

# Localizing and tracking of fluorescent molecules with minimal photon fluxes

Dissertation

for the award of the degree

“Doctor rerum naturalium”

of the Georg-August-Universität Göttingen

within the

International Max Planck Research School  
Physics of Biological and Complex Systems

of the

Göttingen Graduate School for Neurosciences,  
Biophysics, and Molecular Biosciences

submitted by

Dipl.-Phys. Yvan Eilers  
from Vorwerk (Germany)

Göttingen, December 2016

## Members of the Thesis Committee

**Prof. Dr. Stefan W. Hell (Referee)**

Department of NanoBiophotonics,  
Max Planck Institute for Biophysical Chemistry, Göttingen

**Prof. Dr. Sarah Köster (2<sup>nd</sup> Referee)**

Research Group for Nanoscale Imaging of Cellular Dynamics,  
Institute for X-ray Physics, Georg-August-Universität Göttingen

**Prof. Dr. Claus Ropers**

Research Group for Nano-Optics and Ultrafast Dynamics,  
IV. Physical Institute, Georg-August-Universität Göttingen

## Further members of the Examination Board

**Prof. Dr. Christoph F. Schmidt**

Department of Molecular and Cellular Biophysics,  
III. Physical Institute, Georg-August-Universität Göttingen

**PD Dr. Alexander Egner**

Department of Optical Nanoscopy,  
Laser-Laboratorium Göttingen e.V.

**Dr. Thomas P. Burg**

Research Group of Biological Micro- and Nanotechnology,  
Max Planck Institute for Biophysical Chemistry, Göttingen

# Localizing and tracking of fluorescent molecules with minimal photon fluxes

Yvan Eilers

## **Abstract**

In this thesis MINFLUX is presented, a novel optical scheme to determine the position of individual photon emitters in space. By probing the emitter with adapted illumination profiles featuring an intensity zero, the number of emitted photons needed for precise localization can be minimized. Proof-of-concept measurements on static emitters reduced the number of photon detections by 22-fold at equal localization precision compared to widespread camera-based methods. Localization precisions of 2.5 nanometer were realized at 400 microsecond time resolution using only 100 photons. With MINFLUX, the temporal resolution in single molecule tracking experiments of mEos2 fused to 30S ribosomal subunits could be increased by 100-fold. Using the available photons more effectively, the number of localizations was enhanced by more than an order of magnitude permitting a 3-fold improvement in the diffusion coefficient estimation precision. Theoretical evaluations showed that it can be expected that future MINFLUX implementations will improve the spatio-temporal resolution beyond the presented experimental results and thus further facilitate the study of fundamental processes in living organisms at their characteristic time and length scales.





*'Progress in science depends on new techniques,  
new discoveries and new ideas, probably in that  
order.'*

Sydney Brenner



# Contents

<b>1</b>	<b>Introduction</b>	<b>1</b>
1.1	A new photon-efficient localization concept . . . . .	4
<b>2</b>	<b>On theoretical bounds and estimator performances</b>	<b>9</b>
2.1	Localization precision and its theoretical limit . . . . .	9
2.1.1	Fisher information and Cramér-Rao bound . . . . .	10
2.1.2	Geometries of interest . . . . .	15
2.2	Position estimators . . . . .	26
2.2.1	Maximum likelihood estimator . . . . .	27
2.2.2	Other estimators . . . . .	33
2.3	Idealized camera performance . . . . .	41
2.3.1	Fisher information and Cramér-Rao bound . . . . .	42
2.3.2	Maximum likelihood estimator . . . . .	46
2.4	Summary and discussion . . . . .	47
<b>3</b>	<b>Single emitter localization using MINFLUX</b>	<b>51</b>
3.1	Optical setup . . . . .	52
3.2	The multinomial success probability . . . . .	57
3.2.1	Sample preparation . . . . .	57
3.2.2	A functional form for $\bar{p}$ . . . . .	58
3.3	Experimental validation of MINFLUX . . . . .	62
3.3.1	Immobilized single ATTO 647N molecules . . . . .	62
3.3.2	Localization performance in the field of view . . . . .	63
3.4	Localizing with high spatio-temporal resolution . . . . .	69
3.4.1	Sample preparation and measurement protocol . . . . .	69
3.4.2	Experimental results . . . . .	72
3.5	Summary and discussion . . . . .	76

---

<b>4</b>	<b>Single emitter tracking using MINFLUX</b>	<b>79</b>
4.1	Assessment of the tracking performance using simulations . . . . .	80
4.1.1	Challenges imposed by the method . . . . .	80
4.1.2	Parameter optimization . . . . .	83
4.2	Diffusion estimation . . . . .	88
4.2.1	D estimation: algorithm overview . . . . .	89
4.2.2	Applicability and performance of the OLSFE . . . . .	91
4.3	Testing the tracking routine . . . . .	95
4.3.1	Sample preparation and parameter settings . . . . .	95
4.3.2	Data processing and measurement results . . . . .	97
4.4	Tracking 30S ribosomal proteins in <i>E. coli</i> . . . . .	99
4.4.1	Sample preparation . . . . .	99
4.4.2	Data acquisition . . . . .	100
4.4.3	Data processing and experimental results . . . . .	101
4.4.4	Summary and discussion . . . . .	109
<b>5</b>	<b>Conclusion and outlook</b>	<b>111</b>
<b>A</b>	<b>Tracking error for constant localization noise contributions</b>	<b>117</b>
<b>B</b>	<b>Supplementary figures and tables</b>	<b>121</b>
<b>C</b>	<b>DNA sequences</b>	<b>125</b>
	<b>References</b>	<b>129</b>
	<b>List of Abbreviations</b>	<b>135</b>

# Chapter 1

## Introduction

At the end of the last century optical detection of single molecules became reality (Moerner and Kador, 1989) and superresolution fluorescence microscopy emerged as a valuable tool of tremendous impact (Hell and Wichmann, 1994). While previously only ensemble-averaged measurements of molecular properties were possible, the observability of single molecules provided researchers with an entirely new access to the inner workings of living systems. Amongst others, single molecule tracking (SMT) emerged as a powerful tool to investigate the dynamics of single molecules in space and time noninvasively. It permits to reveal transient behaviors in biological processes that are typically averaged out in ensemble measurements, and thus provide a more accurate and quantitative description of the complex and highly dynamic processes in living organisms. Furthermore, as opposed to long standing beliefs (Abbe, 1873), objects that have separations smaller than half the wavelength of light could be discerned using far field optical nanoscopy (Klar et al., 2000). This rendered it possible to obtain information on the inner architecture of biological structures at their native scales under physiological conditions (Huang et al., 2010; D'Este et al., 2016).

Single molecule tracking as well as superresolution microscopy implementations are based on the localization of fluorescent emitters. These emitters are closely attached to the structures or molecules of interest and are excitable and detectable with high contrast. Labeling can be realized with high specificity, ensuring connection of, for example, fluorescent dyes or proteins only to the molecules or the cellular structures under study (Giepmans et al., 2006).

The position estimation of the fluorescent labels generally relies on the collection of fluorescent photons that hold a dependence on the emitter position. Prominent examples are camera-based methods, where fluorescent light from a

single point-like emitter is imaged onto a camera. The collected photons generate a fluorescence diffraction pattern, termed point spread function (PSF). The standard deviation  $\sigma_{PSF}$  of this PSF is typically on the order of 100 nm and is fed to an optimization algorithm to establish the emitter position, e.g. by centroid estimation. The emitter position can be estimated with substantially better precision than  $\sigma_{PSF}$ , typically to  $\sigma_{PSF}/\sqrt{N}$ , where  $N$  is the number of detected photons (Bobroff, 1986; Mortensen et al., 2010; Deschout et al., 2014).

The inverse  $\sqrt{N}$  dependence suggests theoretically unlimited camera localization precision if enough photons are collected, but in reality, the photon-budget is limited by the emitter itself. Fluorescent dyes and fluorescent proteins, for example, suffer from finite photon emission rates and photo-bleaching (Ha and Tinnefeld, 2012; Cranfill et al., 2016). Likewise, the limited photon-budget restricts the obtainable number of localizations, and the limited photon emission rates restrain the attainable localization precision per time frame. Thus, a trade-off between time resolution and localization precision - the so called spatio-temporal resolution - is imposed by the emitter itself.

Therefore, continuous efforts have been made to improve the photostability and the photon emission rates of fluorophores (Marx, 2015). These include the optimization of the fluorophores themselves (Altman et al., 2012; Zheng et al., 2014; Zhang et al., 2016), the manipulation of the emitter environment (Rasnik et al., 2006; Vogelsang et al., 2008), fluorophore-metal interactions (Pellegrotti et al., 2014), cryogenic conditions (Weisenburger et al., 2014) or the use of transient fluorescent labels (Sharonov and Hochstrasser, 2006; Kiuchi et al., 2015; Dai et al., 2016). In live-cell implementations, however, these approaches are of limited applicability only.

Applications of camera localization to SMT arose at the end of the last century when light detectors got sensitive enough (Schmidt et al., 1996). Continuous advances in EMCCD and CMOS sensor technology made this localization scheme one of the most widely used methods in SMT (Yildiz et al., 2003; Elf et al., 2007; Kusumi et al., 2014). Development over the years rendered it possible not only to localize in two dimensions (2D) but also to encode the axial position in the measured fluorescence pattern. Implementations comprise the use of astigmatism (Huang et al., 2008) and optimized detection PSF engineering, for scan free localizations in 3D on large axial field of views (Shechtman et al., 2014, 2016). Furthermore, SMT schemes have been developed that comprise tracking in a confocal volume with multiple point detectors (Sahl et al., 2010) as well as tracking

---

by Gaussian beam scanning (Levi et al., 2003; Kis-Petikova and Gratton, 2004; Sun and Andersson, 2007; Wang and Moerner, 2010; Gallatin and Berglund, 2012; Annibale et al., 2015; Perillo et al., 2015). Yet none of these methods substantially increased the localization precision achievable with a given number of photons  $N$ , the so called photon-efficiency of the localization process.

Camera localization and its photon-efficiency is not only important for the field of SMT but also for multiple superresolution fluorescence nanoscopy implementations. The fundamental principle that is innate to superresolution methods is the adept manipulation of the fluorescent emitters themselves. They are prepared such that the fluorescence signal of the molecules can be detected sequentially in time, rendering the emitters discernible independently of the diffraction limit. Only one feature is allowed to emit in a diffraction limited volume while the rest is switched to a non-emitting OFF state (Hell and Wichmann, 1994; Hell, 2007). In the coordinate-stochastic superresolution modalities like PALM/STORM (Betzig et al., 2006; Hess et al., 2006; Rust et al., 2006), the emitters are switched ON stochastically in space and time and are excited with a uniform widefield excitation. The emitter position is obtained by camera localization such that the localization precision obtainable at a given photon-budget is again determined by approximately  $\sigma_{PSF}/\sqrt{N}$ .

This contrasts with the coordinate-targeted superresolution methods, which most prominently include STED (Hell and Wichmann, 1994; Klar et al., 2000; Hell, 2007). These modalities assure emitter OFF switching by using a tailored laser illumination of suitable spatial shape, wavelength and intensity. Illumination profiles featuring an intensity zero, such as a doughnut shaped beam, are commonly used. Ideally, this so-called depletion beam switches OFF all emitters except the one at the intensity zero. If a fluorophore emits photons in that situation, its location is inherently known. It can only reside at the position of the depletion laser intensity zero.

This work combines elements of coordinate-stochastic superresolution modalities with intrinsic advantages of coordinate-targeted concepts in order to increase the localization precision at a given photon-budget and thus to increase the spatio-temporal resolution of the localization process. Compared to camera-based methods, nanoscale precision is achieved with a significantly reduced amount of emitter photons. The new localization scheme is introduced in a qualitative manner in the next section, before it will be evaluated more rigorously in subsequent chapters.

## 1.1 A new photon-efficient localization concept

In this section, the novel localization modality developed, studied and applied throughout this thesis is introduced in a qualitative manner. The principle is illustrated with a one-dimensional example.

As previously mentioned, typical coordinate-targeted superresolution implementations ideally switch OFF all emitters except the one at the deactivation beam zero. The emission of only one photon would already confirm the presence of the emitter and enable a precise localization. This is a good example of how known excitation profiles, and thus the injected photons, can reduce the number of emitter photons needed for precise localization. Instead of using a known excitation pattern featuring an intensity zero for deactivation, here the pattern is evaluated as an excitation beam. Superimposing the excitation zero on a previously activated emitter would allow a localization with no photons at all. In reality, a precise superposition is not feasible without prior knowledge of the emitter position. Yet the emitter photons obtained in the case of a non-perfect superposition do carry information on the molecule position through the known excitation beam.

Thus, the known illumination profile in conjunction with the emitted photons can be used for localization. It turns out that probing the emitter with multiple displaced excitation beams featuring an intensity zero can reduce the number of detected photons required for precise localization significantly. This is illustrated in one dimension using two displaced standing waves with beam profile  $I(x)$  featuring an intensity zero at the origin such that  $I(0) = 0$ . The measured signal obtained by exciting an emitter at  $x_m$  with that profile will approximately be given by

$$\lambda(x_m) = c_e q_e \sigma_a I(x_m) \equiv CI(x_m) \quad (1.1)$$

where  $c_e$  is the collection efficiency of the measurement device,  $q_e$  is the quantum yield and  $\sigma_a$  is the absorption cross-section of the emitter at the wavelength of excitation. Let us assume that the two profiles are displaced by a distance  $L$  and can be written as  $I_0(x) = I(x + L/2)$  and  $I_1(x) = I(x - L/2)$ . Let the excitation with these beams result in the measurements  $\lambda_0$  and  $\lambda_1$ . The known excitation profile  $I(x)$  can now be used to retrieve the emitter position  $x_m$ , for example by fitting the function  $\lambda(x)$  to the collected signal  $[\lambda_0, \lambda_1]$ . This is possible given that the problem only has two unknown variables:  $C$  and  $x_m$ . The estimated molecule location  $\hat{x}_m$  is then at the position where  $\lambda(\hat{x}_m) = 0$ . This is visualized in the lower panel of fig. 1.1 (A).



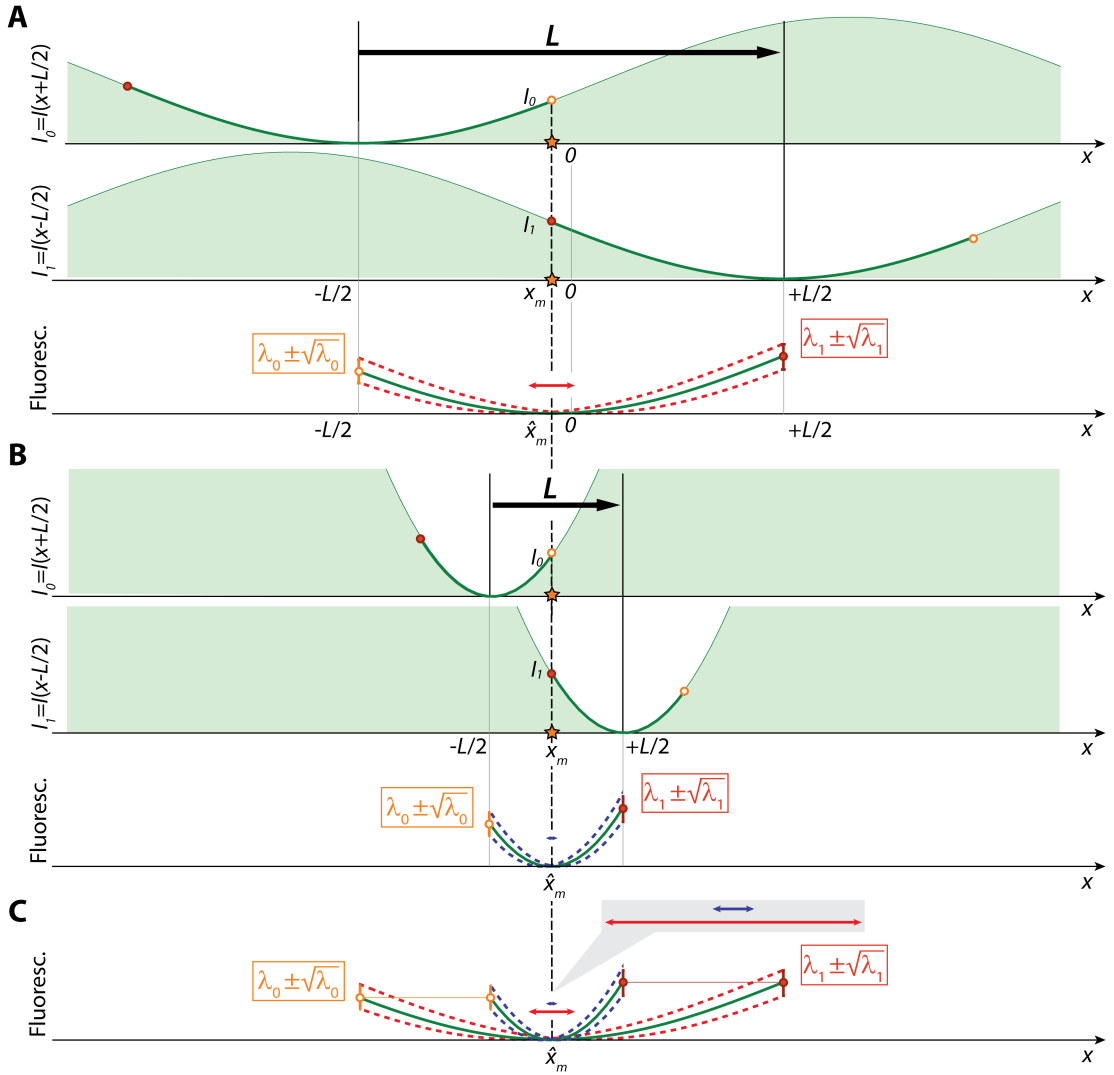


Figure 1.1: Localization principle illustrated in a single dimension ( $x$ ) using a standing light wave  $I(x)$ . **(A)** The emitter at position  $x_m$  is probed twice by the profile  $I(x)$ . For the first measurement the excitation zero is at  $x_0 = -L/2$ , and at  $x_1 = L/2$  for the second. The distance between the zeros is  $L$ . Collection of the fluorescence signals  $\lambda(x_0) = \lambda_0$  and  $\lambda(x_1) = \lambda_1$  allows an estimation of the emitter position by solving  $\lambda(x) = 0$ . In the lower panel this is achieved by fitting the profile  $\lambda(x) = CI(x)$  to the measured signal. Emitter fluorescence fluctuations on the order of  $\pm\sqrt{\lambda}$  will result in an uncertainty of the estimated emitter position (red arrow). **(B)** The inter-zero distance  $L$  is reduced. Higher beam powers or longer integration times enable excitation of the emitter with equal excitation intensities as in (A). The increased steepness in the excitation profile results in a significantly reduced localization uncertainty compared to (A). **(C)** Comparison of the excitation scheme in (A) to the one in (B). The reduction of the emitter position uncertainty at equal photon emissions  $\lambda$  is evident.

In an experimental realization the measured signals will not be the same in every measurement but fluctuate around their mean values  $\lambda_0$  and  $\lambda_1$  with Poissonian statistics. The number of photons  $n_0$  measured from the first exposure will have a mean of  $\langle n_0 \rangle = \lambda_0$  with a standard deviation of  $\sigma_{n_0} = \sqrt{\lambda_0}$ . Correspondingly, the second exposure results in  $\langle n_1 \rangle = \lambda_1$  with  $\sigma_{n_1} = \sqrt{\lambda_1}$ . The uncertainty in the photon collection  $\bar{n} = [n_0, n_1]^T$  will induce an uncertainty in the emitter position estimation. A crude approximation of this uncertainty can be obtained by fitting the values  $[\lambda_0 + \sqrt{\lambda_0}, \lambda_1 - \sqrt{\lambda_1}]$  as well as  $[\lambda_0 - \sqrt{\lambda_0}, \lambda_1 + \sqrt{\lambda_1}]$ . The lower panel in fig. 1.1 (A) shows the two fits as dashed red lines. The resulting localization precision approximation is visualized as a red arrow. It indicates the distance in between the zeros of the two fits.

The example of using a fit as estimator suggests that the position uncertainty induced from the signal fluctuations depends on the excitation profile's steepness and the intensity at the probing points. The magnitude of the fluctuations in the measured signal (e.g.  $\pm\sqrt{\lambda}$ ) depend on the excitation intensity. A high steepness can result in a smaller zero translation when fitting the mentioned signal pairs  $[\lambda_0 \pm \sqrt{\lambda_0}, \lambda_1 \mp \sqrt{\lambda_1}]$ .

It seems thus beneficial to increase the steepness of the excitation profiles without increasing the beam intensity at the emitter position. The presence of an excitation zero allows exactly that, e.g. by moving the two probing zeros closer to the emitter by reducing  $L$  and increasing the beam power. Alternatively, the power can be left unchanged and the signal integration time prolonged. This situation is visualized in fig. 1.1 (B). The lower panel shows the position estimation through a fit as well as the approximation of the position estimation uncertainty. At equal values of  $\lambda_0$  and  $\lambda_1$  a significant reduction of the position uncertainty is obtained. The comparison of the results of the large to the reduced probing range  $L$  is shown in panel (C). Therefore, this localization concept promises the possibility to reduce the number of fluorescence photons needed for high localization precision.

The discussion thus far has provided a simplified motivation for the concept of localizing an emitter using a vanishing excitation light intensity minimum. A strict theoretical evaluation of the many benefits obtainable by encoding spatial information into the excitation illumination as well as arising challenges and their solution will follow in the subsequent chapters.

In chapter 2 a general formulation of the localization problem for an arbitrary number of dimensions, beam-shapes and number of exposures is derived. The formalism permits to assess the theoretical limit of the achievable localization precision for a chosen excitation scheme. Different illumination profiles and various number of exposures are subsequently evaluated in one and two dimensions. The results are then compared to the popular camera localization performance.

In chapter 3 experimental proof-of-concept measurements on a static fluorescent emitter are obtained for different temporal resolutions and compared to the theoretical performance results. The localization scheme is then applied to a moving probe featuring sub-millisecond dynamics on small (nm) length scales.

In chapter 4 the applicability to single molecule tracking on a large ( $\mu\text{m}$ ) field of views is evaluated and the arising challenges are discussed. Finally, mEos2 fused to the 30S ribosomal small subunit protein is tracked in living *Escherichia coli*. The resulting tracking error, the time resolution as well as the precision with which the diffusivity can be estimated is compared to state-of-the-art camera tracking results.

Note that major parts of this work have been recently published in a repository of electronic preprints (Balzarotti et al., 2016). Figures as well as written text are partially adapted from this publication.



# Chapter 2

## On theoretical bounds and estimator performances

### 2.1 Localization precision and its theoretical limit

As indicated in the previous section the proposed measurement scheme allows the flexibility to increase the photon-efficiency of the estimation of an emitter position. An increased photon-efficiency is to be understood as a reduction of the necessary total photons  $N$  to achieve a given localization precision. To quantify the photon-efficiency, the Fisher information and the Cramér-Rao bound (CRB) of the position estimation are calculated. The CRB is an established concept from estimation theory that determines the best possible precision with which a parameter of interest can be estimated (Rao, 1973; Kay, 1993). If the parameter of interest is the molecule position, its CRB yields the best possible localization precision attainable with any unbiased estimator and is therefore a highly informative metric. It can be calculated from the inverse of the Fisher information. The Fisher information provides a measure of the information content that a measurement holds on the parameter of interest. The higher this information content is, the better is the precision with which the parameter can be estimated. In this work the measurement will be given by the collected photon vector  $\bar{n}$  and the parameter of interest is the emitter position  $\bar{r}_m$ . To calculate the Fisher information, the statistics of the measurement process need to be established. In particular the likelihood of having a specific value of the parameter of interest when observing a measurement has to be known. If the likelihood of a given parameter of interest is insensitive to a change in the measurement, the information content will be low. On the other hand, if the likelihood of the parameter does change significantly

upon a change in the measurement, the information content will be high. In the subsequent section the likelihood function as well as the Fisher information and the CRB for the proposed measurement scheme will be derived.

In contrast to the discussion in the introduction, the CRB is calculated for an arbitrary amount of excitation profiles  $I_i$  in a space of arbitrary dimensionality  $d$ . Realistic implementations encompass  $d \in [1, 2, 3]$ , and this work puts a special focus on the two-dimensional (2D) space.

### 2.1.1 Fisher information and Cramér-Rao bound

Let the emitter at position  $\bar{r}_m \in \mathbb{R}^d$  be exposed to a number of  $K$  different excitation intensities  $\{I_0(\bar{r}), \dots, I_{K-1}(\bar{r})\}$ . This results in a measurement of  $\bar{n} = [n_0, \dots, n_{K-1}]^T$  detected photons. Thereby, the respective photons  $n_i$  follow Poissonian statistics with mean  $\lambda_i$ , which depends on the intensity  $I_i(\bar{r}_m)$  with which the emitter is excited. If the excitation intensity is such that saturation is avoided, the mean  $\lambda_i$  can be approximated similarly to eq. (1.1):

$$\lambda_i = c_e q_e \sigma_a I_i(\bar{r}_m) \quad (2.1)$$

Note that in this description, background contributions like detector dark counts or sample background are neglected. However, they will be incorporated later in this chapter (see eq. (2.10)). Given that the photons follow Poissonian statistics, the probability of measuring the photon collection  $\bar{n} = [n_0, \dots, n_{K-1}]^T$  from  $K$  independent measurements is given by:

$$P(\bar{n}) = \prod_{i=0}^{K-1} \frac{\lambda_i^{n_i}}{n_i!} e^{-\lambda_i} \quad (2.2)$$

To be able to quantify the CRB for a fixed number of collected photons  $N$ , it makes sense to condition the measured photons  $n_i$  to  $N$ :

$$\sum_{i=0}^{K-1} n_i = N \quad (2.3)$$

Doing so yields multinomial statistics as can easily be shown:

$$\begin{aligned}
 P\left(\bar{n} \mid \sum_{i=0}^{K-1} n_i = N\right) &= \frac{P\left(\bar{n}, \sum_{i=0}^{K-1} n_i = N\right)}{P\left(\sum_{i=0}^{K-1} n_i = N\right)} \\
 &= \frac{\prod_{i=0}^{K-1} \frac{\lambda_i^{n_i}}{n_i!} e^{-\lambda_i}}{\frac{(\sum_{i=0}^{K-1} \lambda_i)^N}{N!} e^{-\sum_{i=0}^{K-1} \lambda_i}}
 \end{aligned} \tag{2.4}$$

Canceling terms and using  $(\sum_{i=0}^{K-1} \lambda_i)^N = \prod_{j=0}^{K-1} (\sum_{i=0}^{K-1} \lambda_i)^{n_j}$  results in the well known multinomial distribution:

$$P(\bar{n} | N) = \frac{N!}{\prod_{i=0}^{K-1} n_i!} \prod_{i=0}^{K-1} \left( \frac{\lambda_i}{\sum_{j=0}^{K-1} \lambda_j} \right)^{n_i} \equiv \frac{N!}{\prod_{i=0}^{K-1} n_i!} \prod_{i=0}^{K-1} p_i^{n_i} \tag{2.5}$$

The parameters  $p_i$  of that distribution are given by the ratio of the respective Poissonian mean  $\lambda_i$  to the sum of all means. They represent the probability of measuring a count from the corresponding exposure and are henceforth named multinomial success probabilities. Note that these probabilities are independent of emitter properties as well as system parameters  $(q_e, \sigma_a, c_e)$  which is evident upon insertion of eq.(2.1):

$$p_i^{(0)}(\bar{r}_m) = \frac{\lambda_i(\bar{r}_m)}{\sum_{j=0}^{K-1} \lambda_j(\bar{r}_m)}, \quad i \in [0, \dots, K-1] \tag{2.6}$$

$$\Rightarrow p_i^{(0)}(\bar{r}_m) = \frac{I_i(\bar{r}_m)}{\sum_{j=0}^{K-1} I_j(\bar{r}_m)} \tag{2.7}$$

This makes the multinomial success probability  $\bar{p}^{(0)} = [p_0^{(0)}, p_1^{(0)}, \dots, p_{K-1}^{(0)}]$  dependent *only* on the excitation intensities. Additionally, the explicit position dependence of  $\bar{p}^{(0)}$  is evident. The superscript (0) is used to indicate that this success probability is obtained in the situation of no background contributions.

However, every realistic implementation of the method will have background contributions. Therefore, the influence of the background on  $\bar{p}$  will be discussed. I assume that all relevant background contributions to an emitter exposed to an intensity  $I_i$  follow Poissonian statistics. In a experimental implementation the background contribution are typically given by Poissonian noise sources from scattered photons or background fluorescence (Ober et al., 2004). Additionally, detector noise source can be relevant. In this work an avalanche photodiode (APD) detector is used. Measurements showed that the APD dark counts indeed follow a Poisson distribution with a mean count rate of  $\Gamma \approx 87$  counts per second. These

count rate is 2–3 orders of magnitude smaller than the typically measured emitter signal and does thus not really matter. Nevertheless, the assumption of Poissonian background statistics does take these low dark count contributions correctly into account. Given that the sum of Poissonian random variables is again described by Poissonian statistics, the different background contributions can be combined to a mean parameter  $\lambda_{b,i}$ . The detected photons will then be described by a Poissonian distribution with parameter  $\lambda_{tot,i} = \lambda_i + \lambda_{b,i}$ , and thus have a contribution from the emitter as well as from the background photons. As the underlying distribution did not change with regard to the case of no background, the probability  $P(\bar{n}|N)$  is still given by the multinomial distribution of eq. (2.5), with a modified success probability  $\bar{p}$ :

$$p_i(\bar{r}_m) = \frac{\lambda_i(\bar{r}_m) + \lambda_{b,i}}{\sum_{j=0}^{K-1} (\lambda_j(\bar{r}_m) + \lambda_{b,j})} = \frac{c_e q_e \sigma_a I_i(\bar{r}_m) + \lambda_{b,i}}{\sum_{j=0}^{K-1} (c_e q_e \sigma_a I_j(\bar{r}_m) + \lambda_{b,j})} \quad (2.8)$$

The cancellation of emitter properties as well as of the collection efficiency as in eq. (2.7) is unfortunately not applicable anymore. It is therefore convenient to define a signal-to-background ratio (SBR). The advantage is that this ratio is easily measured experimentally as opposed to the explicit values of the quantum yield  $q_e$ , the absorption cross section  $\sigma_a$  and the collection efficiency  $c_e$ :

$$\text{SBR}(\bar{r}_m) \equiv \frac{\sum_{j=0}^{K-1} \lambda_j(\bar{r}_m)}{\sum_{j=0}^{K-1} \lambda_{b,j}} = \frac{\sum_{j=0}^{K-1} c_e q_e \sigma_a I_j(\bar{r}_m)}{\sum_{j=0}^{K-1} \lambda_{b,j}} \quad (2.9)$$

Note that this definition of the SBR is dependent on the excitation intensities  $\{I_j(\bar{r})\}$ , and therefore on the position of the emitter. Rewriting eq. (2.8) using this definition yields:

$$\begin{aligned} p_i(\bar{r}_m) &= \frac{\text{SBR}(\bar{r}_m)}{\text{SBR}(\bar{r}_m) + 1} \frac{\lambda_i(\bar{r}_m)}{\sum_{j=0}^{K-1} \lambda_j(\bar{r}_m)} + \frac{1}{\text{SBR}(\bar{r}_m) + 1} \frac{\lambda_{b,i}}{\sum_{j=0}^{K-1} \lambda_{b,j}} \\ &= \frac{\text{SBR}(\bar{r}_m)}{\text{SBR}(\bar{r}_m) + 1} p_i^{(0)}(\bar{r}_m) + \frac{1}{\text{SBR}(\bar{r}_m) + 1} \frac{1}{K} \end{aligned} \quad (2.10)$$

In the last step the definition of  $\bar{p}^{(0)}$  (see eq. (2.7)) is used, and the assumption is made that all background contributions  $\lambda_{b,i}$  depend on the excitation power only, such that they are rendered equal:  $\lambda_{b,i} = \lambda_b$ ,  $\forall i \in [0, \dots, K-1]$ . Thus, the background contributions change the explicit functionality of the success probability  $\bar{p}$ , but not the underlying distribution  $P(\bar{n}|N)$ . The latter is still given by a multinomial distribution.



It should be stressed that conditioning the sum of detected photons to  $N$  as in eq. (2.3) results in only  $K - 1$  independent variables. That in turn leads to an equal amount of  $K - 1$  independent  $p_i$  parameters. Therefore, the independent elements  $p_i$  span a  $K - 1$ -dimensional space, termed *reduced*  $\bar{p}$  space henceforth. Using the boundary condition  $\sum_{i=0}^{K-1} p_i = 1$  which follows from eq. (2.7) as well as from eq. (2.8), the multinomial distribution of eq. (2.5) can be rewritten to:

$$P(\bar{n}|N, \bar{p}) = \frac{N!}{\prod_{i=0}^{K-1} n_i!} \left( \prod_{i=0}^{K-2} p_i^{n_i}(\bar{r}_m) \right) \left( 1 - \sum_{j=0}^{K-2} p_j(\bar{r}_m) \right)^{n_{K-1}} \quad (2.11)$$

The probability function  $P$  describes the probability of measuring the photon collection  $\bar{n}$  given the success probability  $\bar{p}$  and a total of  $N$  photons.

Subsequently, the information that the photons  $\bar{n}$  hold on the  $d$ -dimensional position of the emitter  $\bar{r}_m$  is calculated. It is evident from eq. (2.11) that a photon realization  $\bar{n}$  holds information on the success probability  $\bar{p}$ , which in turn holds information on the emitter position  $\bar{r}_m$ . Therefore, in the first step, the Fisher information  $F_{\bar{p}}$  that the photon collection  $\bar{n}$  carries on  $\bar{p}$  is calculated. Thereafter, a coordinate transformation will result in the Fisher information  $F_{\bar{r}_m}$  that the photon realization holds on the emitter position  $\bar{r}_m$ . The Fisher information is generally calculated as follows (Kay, 1993)

$$\{F_{\bar{\theta}}\}_{ij} = -E \left( \frac{\partial^2}{\partial \theta_i \partial \theta_j} \ln \mathcal{L}(\bar{\theta} | \bar{m}) \Big|_{\bar{\theta}} \right) \quad (2.12)$$

where  $\bar{\theta}$  is the parameter vector to be estimated and  $\mathcal{L}(\bar{\theta} | \bar{m})$  is the likelihood of the parameter  $\bar{\theta}$  given the measurement  $\bar{m}$ .

Thus, the Fisher information  $F_{\bar{p}}$  is given by

$$\{F_{\bar{p}}\}_{ij} = -E \left( \frac{\partial^2}{\partial p_i \partial p_j} \ln \mathcal{L}(\bar{p} | \bar{n}) \Big|_{\bar{p}} \right), \quad \text{with } i, j \in [0, \dots, K - 2] \quad (2.13)$$

where  $\mathcal{L}(\bar{p} | \bar{n}) = P(\bar{n} | \bar{p})$  is the likelihood function. It describes the likelihood of having the success probability  $\bar{p}$  given the photon measurement  $\bar{n}$ . Inserting eq. (2.11) into eq. (2.13), and using that  $E(n_i) = N p_i$  for a multinomial distribution, yields an expression for the Fisher information matrix for  $\bar{p}$

$$\{F_{\bar{p}}\}_{ij} = N \left( \frac{1}{p_{K-1}} + \delta_{ij} \frac{1}{p_i} \right), \quad \text{with } i, j \in [0, \dots, K - 2] \quad (2.14)$$

where  $\delta_{ij}$  is the Kronecker delta function. Note that failing to take into account the interdependence of the parameters  $p_i$  in eq. (2.11) (which means to insert eq. (2.5) instead of eq. (2.11) into eq. (2.13)), would result in an incorrect Fisher information matrix  $F_{\bar{p}}$ .

If a parameter  $\bar{\theta}$  has an explicit dependency on another parameter  $\bar{\phi}$  such that  $\bar{\theta} = \bar{\theta}(\bar{\phi})$ , the Fisher information  $\{F_{\bar{\phi}}\}_{ij}$  can be obtained from the Fisher information matrix  $\{F_{\bar{\theta}}\}_{ij}$  upon reparametrization as shown in (Kay, 1993). Given that  $\bar{p}(\bar{r}_m)$  is explicitly dependent on the emitter position  $\bar{r}_m$ , the Fisher information  $F_{\bar{r}_m}$  is therefore given by:

$$F_{\bar{r}_m} = J^{*T} F_{\bar{p}} J^* = N J^{*T} \begin{pmatrix} \frac{1}{p_{K-1}} + \frac{1}{p_0} & \cdots & \frac{1}{p_{K-1}} \\ \vdots & \ddots & \vdots \\ \frac{1}{p_{K-1}} & \cdots & \frac{1}{p_{K-1}} + \frac{1}{p_{K-2}} \end{pmatrix} J^* \quad (2.15)$$

Here  $J^* \in \mathbb{R}^{(K-1) \times d}$  is the Jacobian matrix of the transformation from the  $d$ -dimensional  $\bar{r}$  space to the  $(K-1)$ -dimensional reduced  $\bar{p}$  space:

$$J^* = \begin{pmatrix} \frac{\partial p_0}{\partial r_{m1}} & \cdots & \frac{\partial p_0}{\partial r_{md}} \\ \vdots & \ddots & \vdots \\ \frac{\partial p_{K-2}}{\partial r_{m1}} & \cdots & \frac{\partial p_{K-2}}{\partial r_{md}} \end{pmatrix} \quad (2.16)$$

Inserting eq. (2.16) into eq. (2.15) and doing some simplifications yield the final form of the Fisher information  $F_{\bar{r}_m}$ :

$$F_{\bar{r}_m} = N \sum_{i=0}^{K-1} \frac{1}{p_i} \begin{pmatrix} \left( \frac{\partial p_i}{\partial r_{m1}} \right)^2 & \cdots & \frac{\partial p_i}{\partial r_{m1}} \frac{\partial p_i}{\partial r_{md}} \\ \vdots & \ddots & \vdots \\ \frac{\partial p_i}{\partial r_{md}} \frac{\partial p_i}{\partial r_{m1}} & \cdots & \left( \frac{\partial p_i}{\partial r_{md}} \right)^2 \end{pmatrix} \quad (2.17)$$

Note that the information content increases with increasing values of the spatial derivatives of the success probability  $\bar{p}$ , as well as with an increasing number of photons  $N$ . From this result, the lower bound on the covariance matrix of the emitter position estimation  $\Sigma(\bar{r}_m)$  can be computed using the Cramér-Rao bound inequality:

$$\Sigma(\bar{r}_m) \geq \Sigma_{CRB}(\bar{r}_m) = F_{\bar{r}_m}^{-1} \quad (2.18)$$

Therefore, a CRB  $\Sigma_{CRB}(\bar{r}_m)$  is obtained for every emitter position  $\bar{r}_m$ . The computation requires only the total number of photons  $N$  as well as the functional

dependence of the success probability  $\bar{p}$  on the emitter position. The latter follows directly from the excitation intensity profiles and the SBR (see eq. (2.10)).

The arithmetic mean  $\tilde{\sigma}_{CRB}$  of the eigenvalues  $\sigma_i^2$  of  $\Sigma_{CRB}$  is used as a performance metric of the position estimation:

$$\tilde{\sigma}_{CRB} = \sqrt{\frac{1}{d} \text{tr}(\Sigma_{CRB})} \quad (2.19)$$

It represents a measure for the standard deviation of the localization precision, and is equivalent to the square root of the commonly used average variance norm  $\Phi_q[F] = [\text{tr}(F^q)/d]^{1/q}$  with  $q = -1$  for the Fisher information matrix (Pukelsheim, 1993, Chapter 6).

Explicit expressions of the success probability without background contributions  $\bar{p}^{(0)}$ , the Fisher information  $F_{\bar{p}}$ , the CRB  $\tilde{\sigma}_{CRB}$  as well as the reduced Jacobian  $J^*$  can be found in table B.1 in the appendix.

### 2.1.2 Geometries of interest

The preceding section resulted in a general expression of the Cramér-Rao bound (CRB)  $\Sigma_{CRB}(\bar{r}_m)$  in a  $d$ -dimensional space with an arbitrary number of beam exposures  $K$ . Subsequently, the properties of  $\Sigma_{CRB}$  are to be evaluated for specific conditions regarding  $d$  and  $K$  as well as different beam shapes and their arrangement. For reasons of experimental simplicity, the evaluated localization schemes are set to have equal intensity profiles except for a displacement in space

$$I_i(\bar{r}) = I(\bar{r} - \bar{r}_{b,i}) \quad (2.20)$$

with  $\bar{r}_{b,i}$  being the respective beam displacement.

The following evaluation comprises the examination of the one- (1D) as well as the two-dimensional (2D) space. In the former two exposures using a standing wave and its parabolic approximation close to the intensity zero, as well as a doughnut and Gaussian shaped excitation beam are evaluated. Furthermore, a two-dimensional doughnut beam with four exposures is analyzed. It represents the excitation geometry which is heavily used throughout this thesis.

### One-dimensional localization with two exposures

Evaluating the CRB in eq. (2.19) for the case of one dimension ( $d = 1$ ) and two beams ( $K = 2$ ) reduces  $\tilde{\sigma}_{CRB}$  to the simple form

$$\tilde{\sigma}_{CRB} = \frac{1}{\sqrt{N}} \frac{\sqrt{p_0(1-p_0)}}{\left| \frac{dp_0}{dr_0} \right|} \quad (2.21)$$

where, in the case of two exposures,  $p_0$  represents the parameter of a binomial distribution (see eq. (2.11)). In the following evaluation, the assumption of no background contributions is made, and therefore  $p_0$  is given by eq. (2.7). The beam displacements are chosen to be  $r_{b,0} = -L/2$  and  $r_{b,1} = L/2$  such that the two exposures are separated by a distance of  $L$ .

**Standing wave** For this excitation beam the intensity profiles can be described as

$$I_{sw} \left( x \pm \frac{L}{2} \right) = A_0 \sin^2 \left( k \left[ x \pm \frac{L}{2} \right] \right) \quad (2.22)$$

where  $A_0$  is the amplitude, and  $k = 2\pi/\lambda$  the wave vector of the standing wave with period  $\lambda/2$ . Note that  $\lambda$  is not necessarily the wavelength of the excitation light  $\lambda_0$ . Generation of a standing wave with an objective of a given numerical aperture (NA), results in a period  $\lambda/2$  of up to  $\lambda/2 = \lambda_0/2\text{NA}$  (e.g. Bergermann et al. (2015)). The resulting binomial success probability is:

$$p_0^{sw}(x) = \frac{\sin^2 \left( k \left[ x + \frac{L}{2} \right] \right)}{\sin^2 \left( k \left[ x + \frac{L}{2} \right] \right) + \sin^2 \left( k \left[ x - \frac{L}{2} \right] \right)} \quad (2.23)$$

Depending on the emitter position, the value of  $p_0$  changes. For  $x = \pm L/2$ , for example, it assumes the values 0 and 1, and thus spans the full  $p$  range  $[0, 1]$  in a region given by  $L$ . This already indicates an increase in the steepness of  $p_0(x)$  upon reduction of the beam separation  $L$ . It is evident from eq. (2.21) that this, in turn, decreases the CRB for a given  $p_0$  value. The spatial dependence of  $\tilde{\sigma}_{CRB}^{sw}$  is easily calculated:

$$\tilde{\sigma}_{CRB}^{sw}(x) = \frac{\left| \cos \left( 2k \left[ x + \frac{L}{2} \right] \right) + \cos \left( 2k \left[ x - \frac{L}{2} \right] \right) - 2 \right|}{4k\sqrt{N} \sin kL} \quad (2.24)$$

Figure 2.1 (A) visualizes the intensities  $I_0(x) = I_{sw}(x + L/2)$  and  $I_1(x) = I_{sw}(x - L/2)$ , panel (D) the binomial success probability  $p_0(x)$  and (G) the CRB  $\tilde{\sigma}_{CRB}^{sw}$  for three different beam separations  $L$  of 25 nm, 50 nm and 150 nm. For a displacement

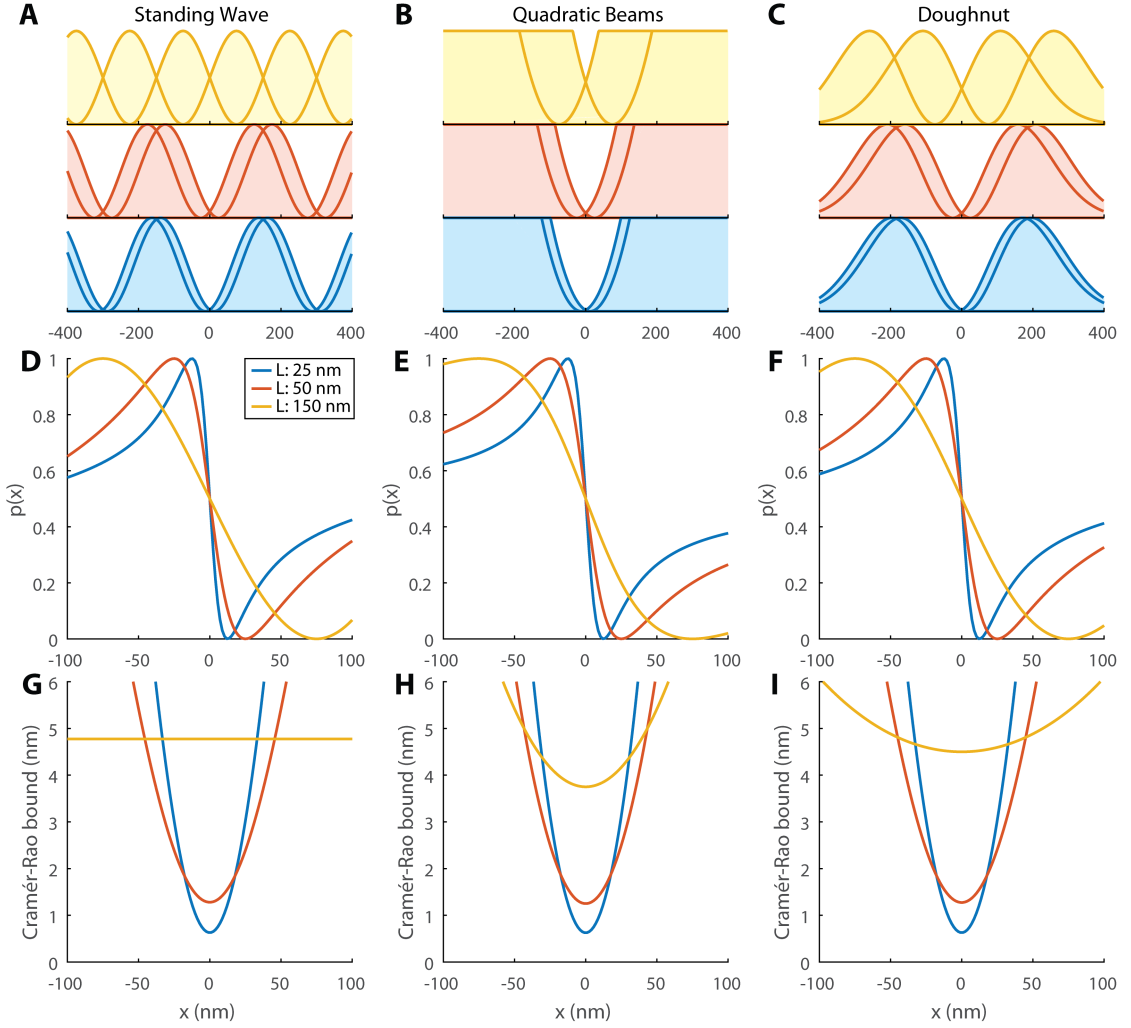


Figure 2.1: One-dimensional success probability  $p$  and CRB  $\tilde{\sigma}_{CRB}$  for different excitation profiles. One-dimensional localization of an emitter with two (**A**, **D**, **G**) standing waves, (**B**, **E**, **H**) quadratic- and (**C**, **F**, **I**) doughnut beams. Each column visualizes the respective beam intensities that are shifted by a distance  $L$  relative to each other, the binomial success probability  $p_0(x)$  as well as the CRB  $\sigma_{CRB}(x)$ . The displacement  $L$  is set to  $L = 25$  nm,  $L = 50$  nm and  $L = 150$  nm. A total of  $N = 100$  photons is assumed. The wave vector  $k$  of the standing wave is  $k = 2\pi/\lambda$  with  $\lambda = 600$  nm and the  $fwhm$  parameter of the doughnut beam is  $fwhm = 300$  nm. The reduction of  $L$  increases the steepness of the  $p$  function and reduces the CRB around the origin, where it is minimal. The value of the lower bound on the localization precision of MINFLUX is truly unlimited in the region surrounding the origin. Figure adapted from Balzarotti et al. (2016).

of  $L = 150 \text{ nm}$  the CRB is flat, indicating a uniform localization precision. A reduction of  $L$  increases the value of the CRB  $\tilde{\sigma}_{CRB}$  especially at the origin, where it assumes its minimal value:

$$\tilde{\sigma}_{CRB}^{sw}(0) = \frac{1}{2k\sqrt{N}} \tan \frac{kL}{2} \quad (2.25)$$

Unlike in camera localization, where the localization precision is homogeneous, here it is now structured with low CRB values in between the zeros surrounding the origin. Henceforth, this interval

$$-\frac{L}{2} \leq x \leq \frac{L}{2} \quad (2.26)$$

is referred to as the field of view.

Close to its respective minima, the standing wave can be described by a quadratic approximation. In fact, both displaced excitation intensities can be approximated by a parabolic beam shape at the emitter position if:

1. the emitter is close to an intensity zero ( $\Delta r \ll \pi k$ ).
2. the beam separation is smaller than half the sine period ( $L \ll \pi/k$ ).

This parabolic approximation is to be evaluated in more detail in the subsequent section.

**Parabolic beam** The definition of a parabolic intensity profile used is

$$I_{quad}(\bar{r}) = A_{quad} r^2 \quad (2.27)$$

where  $A_{quad}$  represents the concavity of the parabolic beam. In one dimension the argument is given by  $\bar{r} = x$ . With that beam shape, the success probability  $p_0(x)$  assumes the following form:

$$p_0(x) = \frac{1}{2} \frac{\left(1 + \frac{x}{L/2}\right)^2}{1 + \left(\frac{x}{L/2}\right)^2} \quad (2.28)$$

$$p_1(x) = 1 - p_0(x)$$

Inserting this success probabilities into eq. (2.21) yields a simple expression for the CRB:

$$\tilde{\sigma}_{CRB}^{quad}(x) = \frac{L}{4\sqrt{N}} \left[ 1 + \left( \frac{x}{L/2} \right)^2 \right] \quad (2.29)$$

A remarkable property of this result is that  $\tilde{\sigma}_{CRB}^{quad}(x)$  is scale invariant, as it depends only on the ratio  $x/L$ . At the origin it assumes its lowest value of:

$$\tilde{\sigma}_{CRB}^{quad}(0) = \frac{L}{4\sqrt{N}} \quad (2.30)$$

Here, the CRB scales linearly with the beam displacement  $L$ . This implies that the value of the lower bound on the localization precision is truly unlimited at the origin.

Note that the linear scaling with  $L$  at  $x = 0$  results for every polynomial of a variable with one even degree of the form:

$$I_k(x) = A_k x^k, \quad \text{with } \frac{k}{2} \in \mathbb{N} \quad (2.31)$$

Following the same derivation as for the parabolic beam we get:

$$\tilde{\sigma}_{CRB}^{(k)}(0) = \frac{L}{2k\sqrt{N}} \quad (2.32)$$

The approximation by functions of the form  $I_k(x)$  is not only valid for standing waves. In fact, it can be applied to a multitude of beam profile with a vanishing intensity minimum. A position coordinate of an emitter residing in the field of view established with a zero valued excitation minima approximable by such a function can thus be made highly precise with a given photon-budget, also for low (minimal) emission fluxes. This inspired the naming of the concept: **MINFLUX**. Furthermore, given that the CRB can locally be made arbitrarily small for a given photon-budget and thus the information per photon arbitrarily high, an alternative interpretation of MINFLUX is: **maximally informative luminescence excitation**. It remains to be shown that an estimator can actually reach the CRB. This will be evaluated later in sec. 2.2.

A visualization of  $I_{quad, p_0}$  and  $\tilde{\sigma}_{CRB}$  is shown in fig. 2.1 (B, E, H) for different beam separations  $L$ . The similarity of the  $p$  functions and the  $\tilde{\sigma}_{CRB}$  profile to the standing wave results is obvious for small  $L$  around the origin. As mentioned earlier, the parabolic approximation also holds for other beam shapes with a vanishing minimum of intensity, such as, for example, a doughnut profile. As this is

the main excitation beam used throughout this work, it is to be evaluated in one and two dimensions.

**Doughnut beam** The general definition of the employed doughnut beam is

$$I_{doughnut}(\bar{r}) = A_0 4e \ln(2) \frac{r^2}{fwhm^2} e^{-\frac{4 \ln(2) r^2}{fwhm^2}} \quad (2.33)$$

where  $A_0$  is the amplitude and  $fwhm$  a size-related parameter. The peak diameter of the intensity profile occurs at:  $1/(\ln 2)^{0.5} fwhm \approx 1.2 \cdot fwhm$ . Using that intensity function with  $\bar{r} = x$ , the binomial success probability as well as the CRB assumes the following intricate form:

$$p_0^{doughnut} = \frac{\frac{1}{2} \left(1 + \frac{x}{L/2}\right)^2 e^{-\frac{4 \ln(2) x L}{fwhm^2}}}{\left[1 + \left(\frac{x}{L/2}\right)^2\right] \cosh \frac{4xL \ln(2)}{fwhm^2} - \frac{2x}{L/2} \sinh \frac{4xL \ln(2)}{fwhm^2}} \quad (2.34)$$

$$\tilde{\sigma}_{CRB}^{doughnut}(x) = \frac{L}{4\sqrt{N}} \left| \frac{\left[1 + \left(\frac{x}{L/2}\right)^2\right] \cosh \frac{4xL \ln(2)}{fwhm^2} - \frac{2x}{L/2} \sinh \frac{4xL \ln(2)}{fwhm^2}}{1 + \frac{L^2}{fwhm^2} \ln(2) \left[\left(\frac{x}{L/2}\right)^2 - 1\right]} \right| \quad (2.35)$$

$$\tilde{\sigma}_{CRB}^{doughnut}(0) = \frac{L}{4\sqrt{N}} \frac{1}{1 - \frac{L^2}{fwhm^2} \ln(2)} \quad (2.36)$$

Figure 2.1 (C, F, I) visualizes the excitation profiles as well as the resulting  $p$  and  $\tilde{\sigma}_{CRB}$  functions. A clear deviation from the result of the parabola is visible for a beam separation of  $L = 150$  nm. But for the smaller evaluated displacements, the functions coincide well, especially around the origin. An approximation by parabolic intensity profiles can be made as long as the emitter remains in the field of view (defined in eq. (2.26)) and the beam separation is smaller than the overall beam size ( $L \ll fwhm/\sqrt{\ln 2}$ ).

### Two-dimensional localization with four doughnut exposures

The previous section showed that MINFLUX in one dimension can be achieved with various excitation beam profiles, including a doughnut beam as defined in eq. (2.33). It shows a similar mathematical behavior around its minimum as a standing wave but provides two-dimensional information. Additionally, it has the benefit of being compatible with a confocal detection to suppress background contributions. Therefore, MINFLUX in two dimensions is evaluated by employing a doughnut shaped beam.



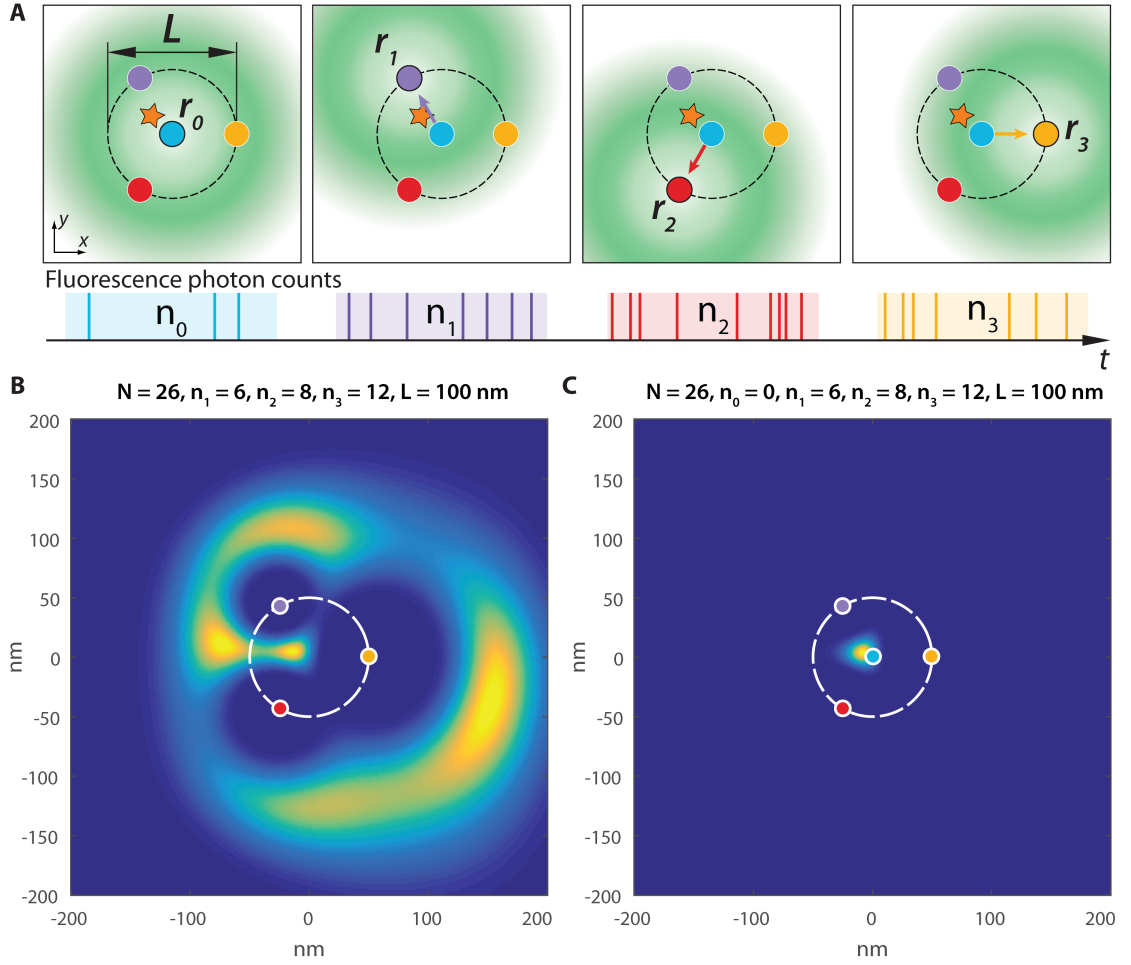


Figure 2.2: **(A)** Excitation beam pattern (EBP) used throughout this dissertation in order to localize an emitter in two dimensions. A central exposure at  $\vec{r}_0 = \vec{0}$  is followed by three exposures equally distributed on a circle of diameter  $L$ . The exposures result in the collection of  $n_i$  photons, respectively. This is illustrated in the lower panel. **(B)** Likelihood function  $\mathcal{L}(\vec{r}_m | \vec{n})$  for a localization with three exposures consisting of doughnut beams ( $fwhm = 200$  nm) with their zeros at the marked colored positions and the photon collection  $\vec{n} = [6, 8, 12]^T$  with a total of  $N = 26$ . The likelihood function is badly behaved for creating a maximum likelihood estimator as it shows multiple equally probable positions. **(C)**  $\mathcal{L}(\vec{r}_m | \vec{n})$  for the case of a fourth central doughnut exposure and the photon collection  $\vec{n} = [0, 6, 8, 12]^T$ . Even though the same number of photons is collected, the radial information encoded in  $n_0 = 0$  concentrates the relevant support of the likelihood function to a much smaller region with a clearly defined maximum; this is favorable in defining a maximum likelihood estimator. Figure adapted from Balzarotti et al. (2016).

In general, a localization in 2D requires at least three peripheral exposures at different positions  $\bar{r}_{b,1}$ ,  $\bar{r}_{b,2}$  and  $\bar{r}_{b,3}$ . Here, the pattern shown in fig. 2.2 (A) is used, which consists of four time shifted exposures, a central one at the origin followed by three exposures equally distributed on a circle of diameter  $L$ .

$$\begin{aligned} I_i(\bar{r}) &= I(\bar{r} - \bar{r}_{b,i}) \\ \bar{r}_{b,0} &= [0, 0]^T \\ \bar{r}_{b,i} &= \frac{L}{2} [\cos(\alpha_i), \sin(\alpha_i)], \quad \text{for } \alpha_i = i \cdot \frac{2\pi}{3} \quad \text{and } i \in [1, 3] \end{aligned} \quad (2.37)$$

The one-dimensional counterpart with two exposures showed a low CRB in between the intensity zeros. The excitation beam pattern (EBP) of eq. (2.37) is therefore expected to perform well within the central field of view given by  $|\bar{r}| \leq L/2$ .

The utilization of a central fourth instead of only three peripheral exposures is beneficial, as it can improve the position estimation. In sec. 2.2 different estimators are discussed. The maximum likelihood estimator (MLE) for example, defines the estimated position as the position that maximizes the likelihood function:  $\hat{r} = \arg \max \mathcal{L}(\bar{r} | \bar{n})$ , with  $\mathcal{L}(\bar{r} | \bar{n}) = P(\bar{n} | \bar{p}(\bar{r}))$  (see eq. (2.11)). Figure 2.2 (B) visualizes the likelihood function for the case of an arbitrary photon collection  $\bar{n} = [n_1, n_2, n_3]$  of only three peripheral doughnut exposures. Though, multiple positions exhibit local maxima for the likelihood function  $\mathcal{L}$ , a unique maximum likelihood estimator  $\hat{r} = \arg \max \mathcal{L}(\bar{r} | \bar{n})$  is defined as long as one of them is absolute. However, fluctuation-driven hopping between two local maxima with similar likelihood values make such an estimator badly behaved. The inclusion of a fourth central doughnut helps the localization by including radial information<sup>1</sup>. The success probability  $p_0(\bar{r})$  suppresses the mentioned indeterminations especially in the central field of view. This is visualized in fig. 2.2 (C), where the likelihood function now displays only one single maximum. Note that the total photon number  $N$  did not change. In fact, the peripheral photon collection is unchanged compared to (B) except for an collection of zero photons from the central exposure. This shows once more how injected information in the form of an intensity zero can improve the localization process without increasing the photon emission flux.

---

<sup>1</sup>The radial dependence of  $p_0(\bar{r})$  is clearly visible in fig. 3.3 (D, H).

The CRB  $\Sigma_{CRB}$  for a two-dimensional localization ( $d = 2$ ) with four exposures ( $K = 4$ ) is obtained from eq. (2.17) and eq. (2.18):

$$\Sigma_{CRB} = \frac{1}{N} \left( \left[ \sum_{i=0}^{K-1} \frac{1}{p_i} \left( \frac{\partial p_i}{\partial x} \right)^2 \right] \left[ \sum_{i=0}^{K-1} \frac{1}{p_i} \left( \frac{\partial p_i}{\partial y} \right)^2 \right] - \left[ \sum_{i=0}^{K-1} \frac{1}{p_i} \frac{\partial p_i}{\partial x} \frac{\partial p_i}{\partial y} \right]^2 \right)^{-1} \quad (2.38)$$

$$\cdot \sum_{i=0}^{K-1} \frac{1}{p_i} \begin{bmatrix} \left( \frac{\partial p_i}{\partial y} \right)^2 & -\frac{\partial p_i}{\partial x} \frac{\partial p_i}{\partial y} \\ -\frac{\partial p_i}{\partial y} \frac{\partial p_i}{\partial x} & \left( \frac{\partial p_i}{\partial x} \right)^2 \end{bmatrix}$$

The arithmetic mean of its eigenvalues  $\tilde{\sigma}_{CRB}$  follows from eq. (2.19):

$$\tilde{\sigma}_{CRB} = \sqrt{\frac{1}{2N} \frac{\sum_{i=0}^{K-1} \frac{1}{p_i} \left[ \left( \frac{\partial p_i}{\partial y} \right)^2 + \left( \frac{\partial p_i}{\partial x} \right)^2 \right]}{\left[ \sum_{i=0}^{K-1} \frac{1}{p_i} \left( \frac{\partial p_i}{\partial x} \right)^2 \right] \left[ \sum_{i=0}^{K-1} \frac{1}{p_i} \left( \frac{\partial p_i}{\partial y} \right)^2 \right] - \left[ \sum_{i=0}^{K-1} \frac{1}{p_i} \frac{\partial p_i}{\partial x} \frac{\partial p_i}{\partial y} \right]^2}} \quad (2.39)$$

Evaluation of these equations for the doughnut EBP introduced in eq. (2.37), yields analytic expressions for the localization performance. These are quite intricate and not reproduced but visualized in this work. Figure 2.3 (A) visualizes  $\tilde{\sigma}_{CRB}(\bar{r})$  for  $L$  values ranging from  $L = 50$  nm to  $L = 150$  nm and a photon collection of  $N = 100$ . Analogously to the one-dimensional case (see fig. 2.1), the CRB is not flat but shows a structured profile which is lowest around the origin and retains low values within a diameter  $L$ . At the origin  $\bar{r} = \bar{0}$ , the analytic expression of  $\tilde{\sigma}_{CRB}$  assumes a simple form:

$$\tilde{\sigma}_{CRB}(\bar{0}) = \frac{L}{2\sqrt{2N}} \left| 1 - \frac{L^2 \ln(2)}{fwhm^2} \right|^{-1} \quad (2.40)$$

Figure 2.3 (C) visualizes  $\tilde{\sigma}_{CRB}(\bar{0})$  as a function of the photon collection  $N$  for different  $L$  values. In the case that the peripheral beam diameter is much smaller than the doughnut size parameter ( $L \ll fwhm$ ), the CRB scales linearly with  $L$ . Thus, as in the one-dimensional case, the increase of localization precision through a geometrical degree of freedom is rendered possible.

Panel (B) shows the covariance matrix  $\Sigma_{CRB}(\bar{r})$ . It is evident that the localization precision is not isotropic and that the anisotropy shows a dependence on the emitter position  $\bar{r}_m$ . This is due to the specific excitation geometry. Note that the inclusion of further equally spaced peripheral excitation beams would render the resulting covariance more isotropic.

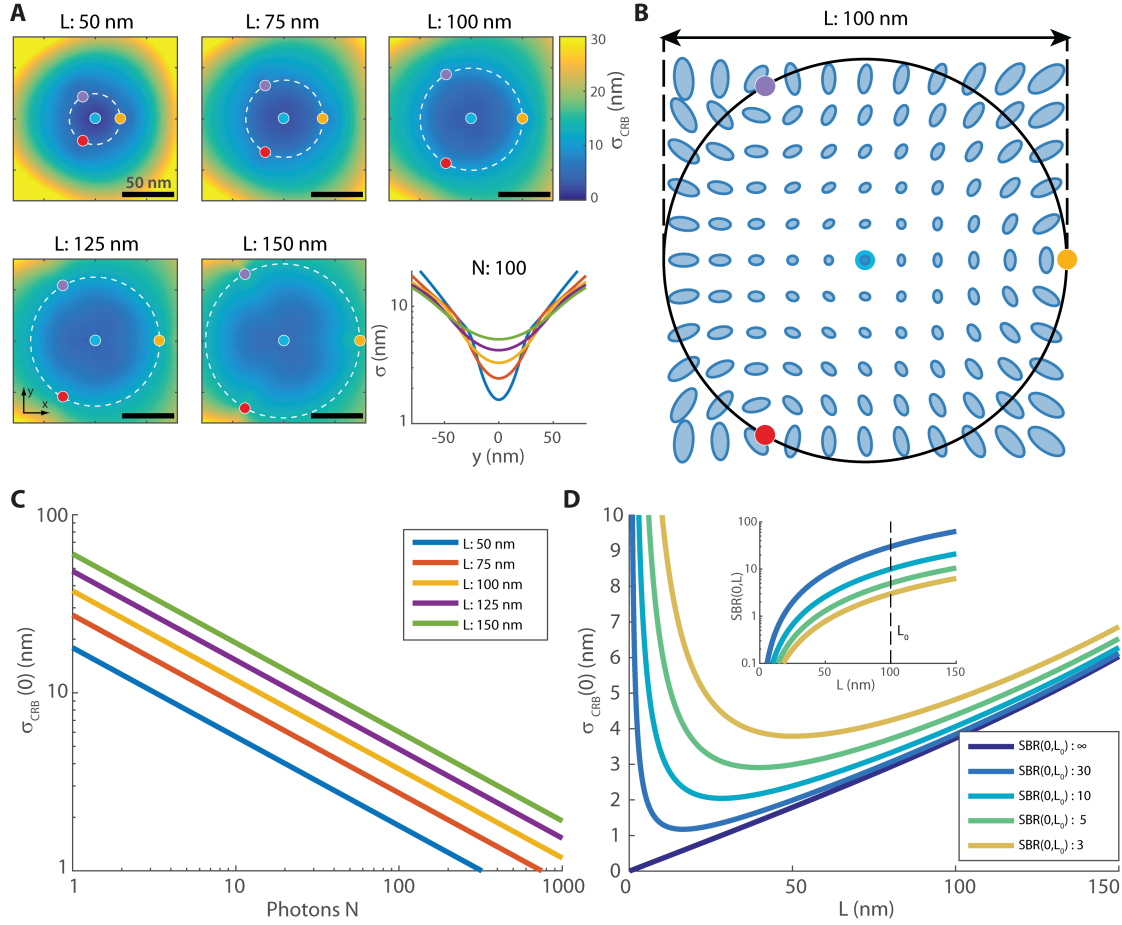


Figure 2.3: **(A)** Position dependent CRB  $\tilde{\sigma}_{CRB}(\vec{r})$  for  $N = 100$  photons. The employed EBP uses doughnut-shaped excitation beams in a geometry depicted in eq. (2.37) and fig. 2.2 (A). The peripheral beams have triangular symmetry and are inscribed in a circle of diameter  $L$ . Colored dots indicate the respective excitation beam zeros. The doughnut is set to have the size parameter  $fwhm = 360$  nm. The CRB is minimal at the EBP origin and grows away from it. Reduction of the parameter  $L$  enables an increase in the localization precision, especially in the vicinity of the origin. The last panel shows a vertical profile through  $\tilde{\sigma}_{CRB}(\vec{r})$ , where the coloring indicates the  $L$  value (see legend in (C)). **(B)** Visualization of the covariance matrix  $\Sigma_{CRB}(\vec{r})$  as a quadratic form for a grid of positions spaced by 9 nm (ellipses of contour level  $e^{-1/2}$ ). The total number of photons is  $N = 1000$ . **(C)** CRB  $\tilde{\sigma}_{CRB}$  at the origin of the beam pattern as a function of the photon collection  $N$  for different beam pattern diameters  $L$  and an infinite SBR. For  $L \ll fwhm$ , the CRB scales linearly with  $L$ . **(D)** Influence of the  $\text{SBR}(\bar{0}, L)$  (see eq. (2.42)) on the CRB at the origin for a total of  $N = 100$  photons and different  $\text{SBR}(\bar{0}, L_0 = 100$  nm) values. Depending on the value of the latter, a reduction of  $L$  improves the localization precision only up to a minimal  $L$ . Smaller separations result in an increase of  $\tilde{\sigma}_{CRB}$ . The effective signal-to-background ratio  $\text{SBR}(\bar{0}, L)$  for different  $L$  values is visualized in the inset. Background contributions establish a limit to the performance of MINFLUX. Figure reproduced from Balzarotti et al. (2016).

**Influence of background contributions** So far the results of the one- as well as two-dimensional examples have been obtained in the limit of an infinitesimal small background contribution. In order to evaluate the expected performance of MINFLUX in a more realistic manner, the influence of background will be discussed. As already derived in section 2.1.1, the  $\bar{p}^{(0)}$  parameter vector of eq. (2.7) has to be adapted to include background contributions. For a signal-to-background ratio (SBR) as defined in eq. (2.9),  $\bar{p}$  assumes the form of eq. (2.10). Inserting this adapted success probability into eq. (2.39) yields a SBR dependent result of the CRB  $\tilde{\sigma}_{CRB}$  at the origin:

$$\tilde{\sigma}_{CRB}(\bar{0}) = \frac{L}{2\sqrt{2N}} \left| 1 - \frac{L^2 \ln(2)}{fwhm^2} \right|^{-1} \sqrt{\left(1 + \frac{1}{\text{SBR}(\bar{0})}\right) \left(1 + \frac{3}{4 \cdot \text{SBR}(\bar{0})}\right)} \quad (2.41)$$

Note that the SBR not only has a position dependence, but it is also a function of  $L$ . This is because in a typical experimental realization the background will not depend on the beam displacement. But the emitter at  $\bar{r} = \bar{0}$ , for example, will see a reduced total intensity upon reduction of  $L$ . Thus, the value of  $\text{SBR}(\bar{0})$  decreases with a reduction of  $L$ . Assuming that  $\text{SBR}(\bar{0}, L_0)$  - the SBR at the origin for a beam displacement of  $L_0$  - is known, the  $L$  dependence of  $\text{SBR}(\bar{0}, L)$  can be written as:

$$\text{SBR}(\bar{0}, L) = \text{SBR}(\bar{0}, L_0) \cdot \frac{L^2}{L_0^2} e^{\frac{\ln(2)}{fwhm^2}(L_0^2 - L^2)} \quad (2.42)$$

Figure 2.3 (D) visualizes the influence the SBR has on the CRB  $\tilde{\sigma}_{CRB}(\bar{0})$  for a value of  $L_0 = 100$  nm and  $\text{SBR}(\bar{0}, L_0)$  values ranging from 3 to  $\infty$ . The presence of background contributions increases the value of the CRB at the origin and, most importantly, it introduces a limit to the usable beam separation  $L$ . The localization precision cannot be improved further by reducing the beam separation over that limit. Thus, the presence of background establishes a lower boundary for MINFLUX.

**Gaussian beam** Another interesting intensity profile to evaluate is the Gaussian beam. Because of the absence of a local minimum, it is not obvious if MINFLUX also applies in this situation.

$$I_{gauss}(\bar{r}) = A_0 e^{\frac{-4 \ln(2) r^2}{fwhm^2}} \quad (2.43)$$

Here, the parameter  $fwhm$  is the full width half maximum of the Gaussian beam. The Gaussian beam is evaluated in one dimension. This profile can be treated equally to the other cases and leads to:

$$p_0^{gauss}(x) = \frac{e^{\frac{4xL \ln(2)}{fwhm^2}}}{2 \cosh \frac{4xL \ln(2)}{fwhm^2}}, \quad p_1^{gauss}(x) = \frac{e^{-\frac{4xL \ln(2)}{fwhm^2}}}{2 \cosh \frac{4xL \ln(2)}{fwhm^2}} \quad (2.44)$$

$$\tilde{\sigma}_{CRB}^{gauss}(x) = \frac{fwhm^2}{4L\sqrt{N} \ln(2)} \cosh \frac{4xL \ln(2)}{fwhm^2} \quad (2.45)$$

$$\tilde{\sigma}_{CRB}^{gauss}(0) = \frac{fwhm^2}{4L\sqrt{N} \ln(2)} \quad (2.46)$$

Figure (2.5) (A, C, E) visualizes these results for beam separations in the range of  $L = (25 - 1200)$  nm. For small separations this excitation geometry leads to success probabilities  $p$  that are not steep and consequently to high CRB values. However, large  $L$  lead to low  $\tilde{\sigma}_{CRB}$  values as can be seen from the  $\propto 1/L$  dependence of  $\tilde{\sigma}_{CRB}^{gauss}(x)$  at the origin (see eq. (2.46)). This can be understood from an analysis of the intensity profiles  $I_i(x)$  for large  $L$ . A Taylor expansion shows that for large  $L$ , the intensity profile  $I(x \pm L/2)$  can be approximated by a polynomial of order two. The utilization of a square completion results in  $I(x \pm L/2) \approx c_1/L^2 + (x \pm c_2/L)^2$ , where  $c_1$  and  $c_2$  are constants. In the limit of large  $L$  this is not distinguishable from the parabolic beam geometry discussed previously. The offset vanishes and the intensity minima converge to each other. Thus, the concept of MINFLUX applies if the emitter is excited by the tails of two Gaussian beams. The theoretical performance is increased the closer one gets to the Gaussian beam minima (which are at infinity). In an experimental realization, this might not be the best beam choice. To obtain reasonably high intensity values at positions far from the Gaussian beam center, high excitation powers are needed.

## 2.2 Position estimators

Section 2.1 investigated Cramér-Rao bounds (CRB) for different MINFLUX excitation geometries. It was shown that the lower bound on the localization precision in a given field of view can be improved upon reduction of a geometrical parameter  $L$ . It needs to be stressed that the CRB provides a value for the best possible performance that any unbiased estimator can achieve. However, it does not give information about the actual performance of a chosen estimator. In this section

the performance of two estimators is to be evaluated. Section 2.2.1 investigates the maximum likelihood estimator (MLE) for different excitation geometries. Section 2.2.2 evaluates a further estimator that is optimized for the low photon regime.

### 2.2.1 Maximum likelihood estimator

The maximum likelihood estimation (MLE) is a widely employed method for parameter estimation. This is related to the many optimal properties it holds, especially consistency (i.e., an asymptotically unbiased estimator) and efficiency (i.e., the MLE converges to the CRB) (Fisher, 1922). Three instances of MLE calculations follow in this section. The one-dimensional localization with two parabolic beams is used as an illustrative example. Additionally, the one-dimensional localization with two Gaussian exposures is evaluated. This localization is used in the intermediate localization step for tracking described in chapter 4. Finally, I will discuss the two-dimensional localization with four doughnut exposures including background as described in sec. 2.1.2, which is the main method presented in this work.

The position  $\bar{r}_m$  of an emitter is estimated from a photon collection  $\bar{n}$  using the maximum likelihood estimator  $\hat{r}_m^{MLE}$  defined as:

$$\hat{r}_m^{MLE} = \arg \max \mathcal{L}(\bar{r} | \bar{n}) \quad (2.47)$$

Thus, the emitter is assumed to be at the position which maximizes the likelihood function  $\mathcal{L}(\bar{r} | \bar{n}) = P(\bar{n} | N, \bar{p}(\bar{r}))$  given by the conditional probability distribution of the photon collection defined in eq. (2.11).

#### MLE for 1D position with two parabolas

Doughnut shaped excitation beams, standing waves as well as multiple other excitation profiles with an intensity zero can be approximated by a parabolic beam around its origin. It is therefore of interest to evaluate the MLE for the position in the case of two parabolic profiles. The excitation beam pattern (EBP) follows the definition of eq. (2.20) with beam displacements  $x_{b,0} = -L/2$  and  $x_{b,1} = L/2$ . In this excitation geometry, the success probabilities  $p_0(x)$  and  $p_1(x)$  are given by eq. (2.28) and lead to the following likelihood function:

$$\mathcal{L}(x | \bar{n}) = \frac{N!}{n_0!n_1!} \prod_{i=0}^1 p_i^{n_i} \quad (2.48)$$

$$\Rightarrow \mathcal{L}(x | \bar{n}) = \frac{N!}{n_0!n_1!} \frac{\left(1 + \frac{2x}{L}\right)^{2n_0} \left(1 - \frac{2x}{L}\right)^{2n_1}}{\left(2 + \frac{8x^2}{L^2}\right)^N} \quad (2.49)$$

As is classically done, the MLE estimate  $\hat{x}_m^{MLE}$  is obtained by maximizing the log-likelihood function. In this case it allows to drop the multiplicative factors that only depend on  $\bar{n}$ .

$$\begin{aligned} \frac{d \ln \mathcal{L}(x | \bar{n})}{dx} &\stackrel{!}{=} 0 \\ \Rightarrow p_0(\hat{x}^{MLE}) &= \frac{n_0}{n_0 + n_1} \\ \Rightarrow \hat{x}_1^{MLE} &= \frac{L}{1 + \sqrt{n_1/n_0}} - \frac{L}{2}, \quad \hat{x}_2^{MLE} = \frac{L}{1 - \sqrt{n_1/n_0}} - \frac{L}{2} \end{aligned} \quad (2.50)$$

The MLE has two solutions which give rise to indeterminations in the position. The result for the field of view defined by  $-L/2 < x < L/2$  is given by  $\hat{x}_1^{MLE}$  and is therefore the one of interest. Note that the inclusion of additional exposures in the EBP can make the MLE unique.

Note also that in the parabolic approximation the success probability  $\bar{p}$  and therefore the MINFLUX localization itself, does not depend on the wavelength creating the light pattern and, since the fluorescence is only collected, MINFLUX does not depend on any wavelength.

It is enlightening to analyze the obtained result further. As discussed earlier, the photon collection  $\bar{n}$  follows a multinomial distribution with parameter  $\bar{p}$ . Thus, a measured collection of photons will hold information on the parameter of its distribution. Actually, the maximum likelihood estimator of the  $\bar{p}$  parameter is simply given by:

$$\hat{p}_i = \frac{n_i}{\sum_j n_j} = \frac{n_i}{N} \quad (2.51)$$

We know that  $\bar{p}$  as defined in eq. (2.7) and (2.10) is a function of the excitation profiles and will thus be a function of the position. Therefore, the estimate of the position can be obtained by making use of the invariance property of the MLE (e.g. Mukhopadhyay (2000)):

$$\bar{p}(\hat{r}) = \hat{p} \quad (2.52)$$

In the one-dimensional example with two parabolas, this reduces to  $p_0(\hat{x}) = \hat{p}_0 = n_0/(n_0 + n_1)$ , as obtained in eq. (2.50). We can say that  $p_0(x)$  maps the statistics of  $n_0$  and  $n_1$  into the position estimation, giving the distribution of the position estimator  $P(\hat{x}_m | N, \bar{p})$ . In other words, if the values  $n_i$  of the acquired photons



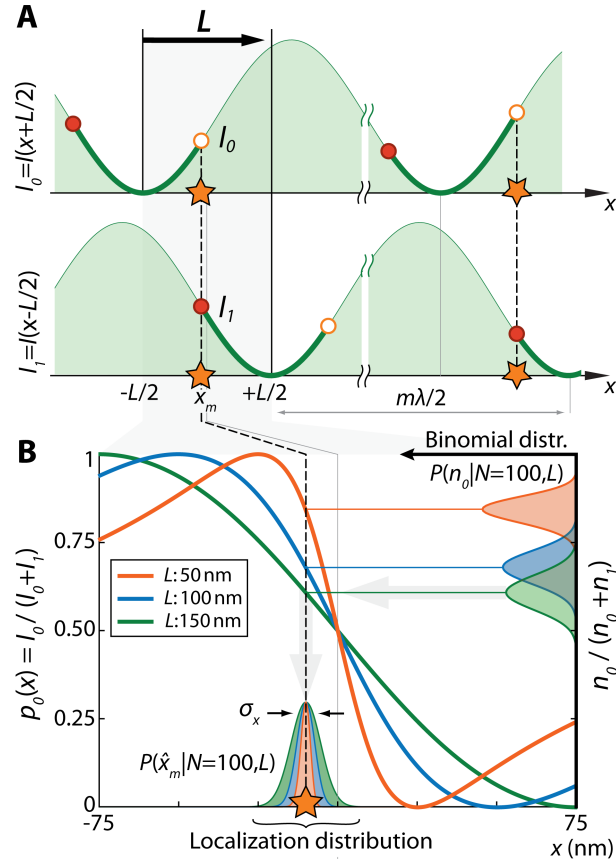


Figure 2.4: **(A)** Excitation of an emitter at  $x_m$  by illumination with two translated standing waves ( $k = 2\pi/\lambda$ ,  $\lambda = 640$  nm), with one intensity zero at  $x_0 = -L/2$  and the second at  $x_1 = -L/2$ . This results in two photon collections  $n_0$  and  $n_1$  that follow a binomial distribution  $P(n_i | N)$ . **(B)** Success probability  $p_0(x)$  for  $L = 50$  nm,  $L = 100$  nm and  $L = 150$  nm. The  $p$  space distributions  $P(n_0 | N)$  with  $N = 100$  are plotted along the vertical axis for the respective  $L$  values. They are mapped through the success probability  $p_0(x)$  to the position space and result in the localization distribution  $P(\hat{x}_m | N)$ , which narrows with decreasing  $L$ . Figure adapted from Balzarotti et al. (2016).

with a total of  $N$  fluctuate, the estimated success probability  $\hat{p}_0$  will also vary and result in a fluctuation of the position estimate  $\hat{x}_m$ . For two exposures the fluctuations of  $n_0$  and  $n_1$  will follow binomial distributions. This is visualized in fig. 2.4, where two standing waves shifted by  $L$  are shown in (A). The success probability  $p_0(x)$  is shown in (B). Additionally, the binomial distribution for an emitter position  $x_m$  is visualized for three different  $L$  values and  $N = 100$  photons. A reduction of  $L$  results in an improvement of localization precision for the given emitter position.

### MLE for 1D position with two Gaussian beams

The maximum likelihood estimate of the position for two Gaussian excitation profiles is used in the tracking application. The success probabilities  $p_0$  and  $p_1$  are given by eq. (2.44). Inserting these into the likelihood function of eq. (2.48) yields the MLE  $\hat{x}_m^{MLE}$  for the position:

$$\begin{aligned} \frac{d\mathcal{L}(x|\bar{n})}{dx} &\stackrel{!}{=} 0 \\ \Rightarrow \hat{x}_m^{MLE} &= \frac{fwhm^2}{8L \ln(2)} \ln\left(\frac{n_0}{n_1}\right) \end{aligned} \quad (2.53)$$

This is a surprisingly simple result that is well suited to being implemented as a live position estimation in an experimental system. It is evident from eq. (2.53) that a position estimation makes sense only if at least one photon is collected from the respective exposures. Problems resulting from zero photon collections are intercepted by defining  $\hat{x}_m^{MLE}(n_i = 0 | N) \equiv 0$ .

The performance of a position estimator is given by its ability to precisely reproduce the true emitter position. In the following, the bias  $bias_{MLE}(x_m)$  as well as the localization precision  $\tilde{\sigma}_{MLE}(x_m)$  are to be evaluated for the MLE position estimate of eq. (2.53). They are calculated as:

$$\begin{aligned} bias_{MLE}(x_m) &= \langle \hat{x}_m^{MLE} \rangle - x_m \\ \tilde{\sigma}_{MLE}(x_m) &= \sum_{n_0=0}^N \left( \hat{x}_m^{MLE} - \langle \hat{x}_m^{MLE} \rangle \right)^2 P(n_0 | N) \\ \text{with } \langle \hat{x}_m^{MLE} \rangle &= \sum_{n_0=1}^{N-1} \hat{x}_m^{MLE} P(n_0 | N) \end{aligned} \quad (2.54)$$

Figure 2.5 (D, E) visualizes both quantities for a beam separation of  $L = 300$  nm and different amounts of total photons  $N$ . The unbiased region is a function of the total number of photons. A minimal  $N$  is needed in order to have an unbiased position estimate in a given field of view. Furthermore, the localization precision  $\tilde{\sigma}_{MLE}(x_m)$  asymptotically approaches the CRB with increasing  $N$  in the proximity of the origin. Consequently, the localization precision reproduces the properties found for the CRB of eq. (2.46), especially the  $\propto L^{-1}$  dependence and the divergence of  $\tilde{\sigma}_{CRB}(x_m)$  with increasing distance to the origin. However,  $\tilde{\sigma}_{MLE}(x_m)$  falls below the CRB at positions where the bias is not negligible. This is acceptable, as the CRB is a lower bound for unbiased estimators only.

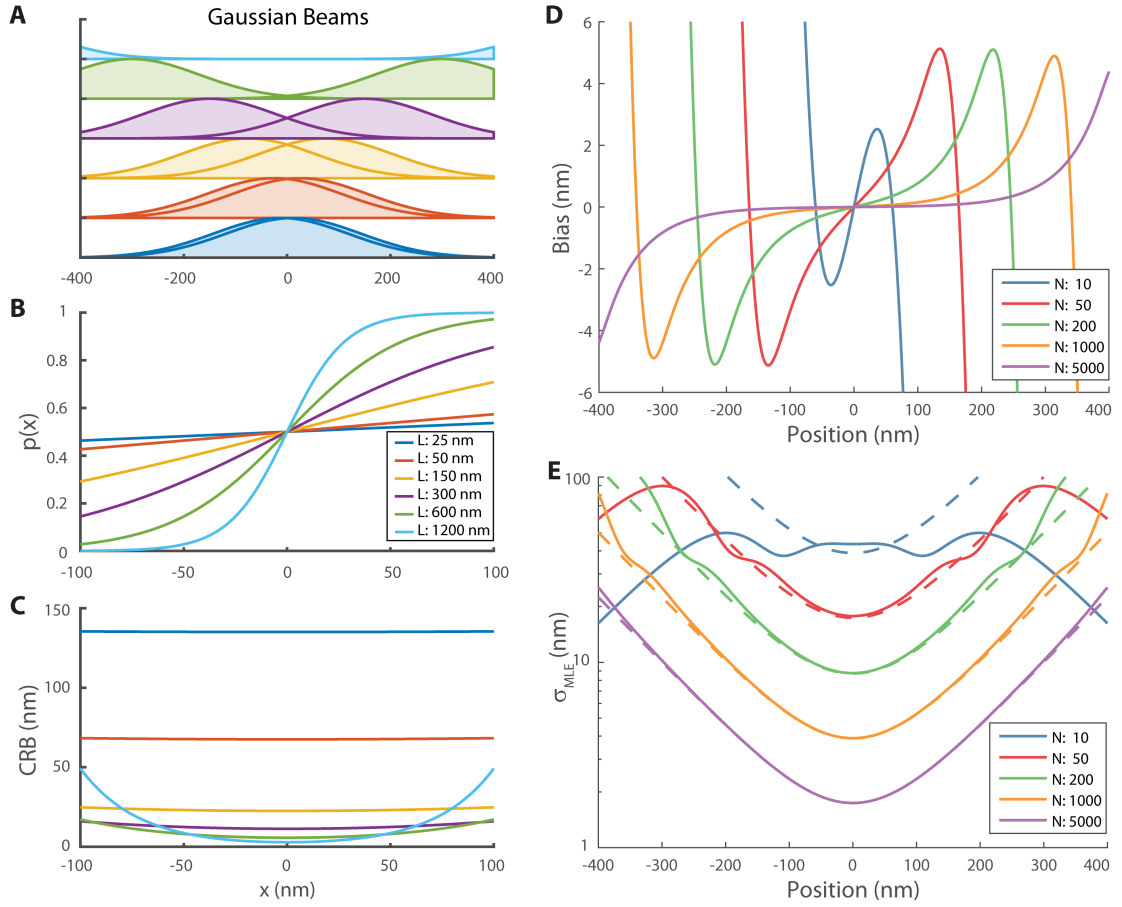


Figure 2.5: One-dimensional localization performance with two Gaussian beams. (A-C) Visualization of the intensity profile  $I_i(x)$ , the binomial success probability  $p_0(x)$  as well as the CRB  $\tilde{\sigma}_{CRB}(x)$  (eq. (2.43)-(2.46)) for different beam displacements  $L$  of 25 nm to 1200 nm. The full width half maximum is set to  $whm = 300$  nm. Steep  $p$  functions and low CRB values are achieved for large  $L$  values. (D) Visualization of the bias as a function of the position for different total number of photons  $N$  of the maximum likelihood position estimate given by eq. (2.53). The excitation geometry is the same as in (A) with  $whm = 320$  nm and a beam displacement of  $L = 300$  nm. The region with low bias grows with increasing number of photons, whereas the origin stays unbiased. (E) Localization precision  $\tilde{\sigma}_{MLE}$  (solid lines) compared to the Cramér-Rao bound (dashed lines) for different total number of photons  $N$ . The precision approached the CRB in the limit of high photon numbers. For low  $N$ ,  $\tilde{\sigma}_{MLE}$  deviates from its CRB, though. It falls below the CRB at outer positions as the estimator is biased in these situations. Figure adapted from Balzarotti et al. (2016).

## 2D position MLE with four doughnut beams

The EBP of four doughnut beams is given by eq. (2.37) and visualized in fig. 2.2 (A). Insertion into the likelihood function  $\mathcal{L}(\bar{r} | \bar{n}) = P(\bar{n} | \bar{p}(\bar{r}))$  (see eq. (2.11)) yields the following simplified log-likelihood  $\ell(\bar{r} | \bar{n})$

$$\ln \mathcal{L}(\bar{r} | \bar{n}) \propto \ell(\bar{r} | \bar{n}) = \sum_{i=0}^2 n_i \ln(p_i(\bar{r})) + n_3 \ln\left(1 - \sum_{i=0}^2 p_i(\bar{r})\right) \quad (2.55)$$

where the success probability  $\bar{p}$  is defined in eq. (2.10) and visualized in fig. 3.3 (D-G). As denoted in eq. (2.47), the maximum likelihood estimator  $\hat{r}_m^{MLE}$  can be obtained by maximization of the simplified likelihood function, which implies the derivation of  $\ell(\bar{r} | \bar{n})$ . Given the intricate expressions involved and therefore the complexity of finding an analytic solution for  $\hat{r}_m^{MLE}$ , the problem is solved numerically.

This is accomplished by use of a grid search. For a given photon collection  $\bar{n}$ , the simplified likelihood  $\ell(\bar{r} | \bar{n})$  is evaluated successively on position grids with decreasing spacing. Typically, the initial grid has a spacing of 5 nm and is followed by three further grids with 0.5 nm, 0.1 nm and 0.01 nm spacing.

The resulting estimator performance is visualized in fig. 2.8 (A), where the localization error is compared to its CRB  $\tilde{\sigma}_{CRB}(\bar{r})$  given by eq. (2.19). The localization error is defined as

$$\sigma_{MLE}^{(1D)} = \sqrt{\tilde{\sigma}_{MLE}^2 + bias_{MLE}^2} \quad (2.56)$$

where the localization precision  $\tilde{\sigma}_{MLE}(\bar{r})$  is the arithmetic mean of the eigenvalues of the covariance matrix  $\Sigma_{MLE}$ :

$$\tilde{\sigma}_{MLE} = \sqrt{\frac{1}{2} \text{tr} \Sigma_{MLE}} \quad (2.57)$$

The error and the bias were evaluated numerically for different emitter positions as a function of the total number of photons  $N$  for different beam separations  $L$  and a SBR of 10. The performance shows a dependence on the photon number as well as on the position and the parameter  $L$ . For high  $N$  values, the MLE asymptotically approaches its CRB in all instances. For  $x = 50$  nm and  $y = 0$  nm, for example, the MLE converges starting from about 500 photons. The convergence arises earlier closer to the EBP origin, already at about 100 photons for all shown beam

separations. Especially for a low photon number the bias assumes high values and the MLE breaks: it deviates strongly from its CRB.

### 2.2.2 Other estimators

In addition to the MLE, another position estimator is used. This is because the tracking application of chapter 4 requires an estimator suitable for the low photon regime. In that application a single emitter is followed by subsequently repositioning the four-doughnut excitation beam pattern (EBP) center on the emitter. The position estimator has to be simple enough to be implemented as a live position estimator in the experimental system. The MLE is not suitable given that it breaks for the EBP employed in the tracking application and low photon numbers  $N$ , as shown in sec. 2.2.1. Additionally, a position estimation employing the MLE would be too slow for live implementation, if no bulky lookup table is used. Concise live position estimation is required as the beam pattern repositioning needs to be fast enough such that the molecule does not diffuse out of the high sensitivity field of view surrounding the beam pattern origin.

In this section the least-mean-square (LMS) estimator is developed, which linearizes the position estimation around the EBP origin and leads to a simple functionalized estimator. Subsequently, a modified LMS estimator (mLMS) is presented, which has a better performance but keeps the computational simplicity of the LMS. Finally, a numerically unbiased version of the mLMS estimator is introduced. This numLMS estimator is used in post processing for low photon localization.

#### Linearized least mean squared (LMS) estimator

The evaluation of the Cramér-Rao bound for the EBP given by four displaced doughnut excitations showed that the best localization precision can be attained around the origin of the pattern (see sec. 2.1.2). This is the region in which a molecule is kept in a tracking application. Thus, it makes sense to construct an estimator that is especially suited in that field of view.

As has been discussed in sec. 2.2.1 the photon collection  $\bar{n}$  follows a multinomial distribution and holds information on the parameter vector  $\bar{p}$  of its statistics. The MLE for a multinomial distribution is given by eq. (2.51). As  $\bar{p}$  has a position dependence, the MLE for the position can be obtained using the invariance prop-

erty of the maximum likelihood estimation as is evident from eq. (2.52). Here, a first order approximation of  $\bar{p}(\bar{r})$  at the beam pattern origin  $\bar{r} = \bar{0}$  is used

$$p_i(\bar{r})|_{r=0} \cong p_i(\bar{0}) + \sum_{j=1}^d r_j \frac{\partial p_i}{\partial r_j} \quad (2.58)$$

where  $\bar{r} \in \mathbb{R}^d$ . In this work, position estimations are mainly performed in two dimension ( $d = 2$ ). Inserting eq. (2.58) into eq. (2.52) yields:

$$J\hat{r} = \hat{p} - \bar{p}(\bar{0}) \quad (2.59)$$

where  $J = \bar{\nabla}\bar{p}$  is the Jacobian matrix of the transformation from the  $\bar{r}$  space to the  $\bar{p}$  space. Note that  $J \in \mathbb{R}^{K \times d}$  has a dimensionality of  $K \times d$  as opposed to the Jacobian of the transformation of the  $\bar{r}$  space to the *reduced*  $\bar{p}$  space as introduced in eq. (2.16):  $J^* \in \mathbb{R}^{(K-1) \times d}$ . The over-determined linear system of equations in eq. (2.59) can be approximated by employing the method of ordinary least squares (Hayashi, 2000). Consequently, the objective function  $S$  that needs to be minimized in order to obtain the position estimate  $\hat{r}$  is given by:

$$S(\hat{r}) = \sum_{i=0}^{K-1} \left| \hat{p}_i - p_i(0) - \sum_{j=1}^d J_{ij} \hat{r}_j \right|^2 = \|\hat{p} - \bar{p}(\bar{0}) - J\hat{r}\|^2 \quad (2.60)$$

The standard minimum square solution leads to the LMS estimator  $\hat{r}_{LMS}$ :

$$\hat{r}_{LMS}(\hat{p}) = (J^T J)^{-1} J^T (\hat{p} - \bar{p}(\bar{0})) \quad (2.61)$$

For the two-dimensional localization ( $d = 2$ ) with four doughnut shaped excitation profiles ( $K = 4$ ) introduced in eq. (2.37), we obtain the surprisingly simple result:

$$\hat{r}_{LMS}(\hat{p}) = \frac{L}{2} \cdot \left| 1 - \frac{L^2 \ln(2)}{fwhm^2} \right|^{-1} \begin{bmatrix} -\hat{p}_3 + \frac{1}{2}(\hat{p}_1 + \hat{p}_2) \\ \frac{\sqrt{3}}{2}(\hat{p}_2 - \hat{p}_1) \end{bmatrix} \quad (2.62)$$

Comparing this solution with the beam positions  $\bar{r}_{b,i}$  defined in eq. (2.37), we can simplify eq. (2.62) to:

$$\hat{r}_{LMS}(\hat{p}) = -\frac{1}{1 - \frac{L^2 \ln(2)}{fwhm^2}} \sum_{i=1}^3 \hat{p}_i \cdot \bar{r}_{b,i} \quad (2.63)$$

This arises because in the vicinity of the origin the gradient of the  $p_i(\bar{r})$  functions point in the direction of the corresponding beam positions  $\bar{r}_{b,i}$ . Thus, the LMS es-

estimator is given by a scaled linear combination of the  $p_i$  parameter MLE estimates  $\hat{p}_i$ , multiplied by the respective directions of the peripheral excitation beams.

### Modified least mean squared (mLMS) estimator

The LMS solution in eq. (2.63) assumes a simple form that could readily be implemented in the experimental system for live position estimation. Unfortunately, it does not make use of the photons  $n_0$  obtained from the first, central doughnut exposure. This is because the function  $p_0(\vec{r})$  has no linear contribution in its polynomial expansion at the origin  $\vec{r} = \vec{0}$ . These photons do not hold directional information but they do hold radial information, as visualized in fig. 3.3 (D). An increase of the  $p_0$  value indicates an increase of the radial coordinate, especially in the vicinity of the EBP origin. To include this property in the position estimator, eq. (2.63) is expanded in orders of  $\hat{p}_0$  with scaling parameters  $\beta_j$ :

$$\hat{r}_{mLMS}^{(k)}(\hat{\vec{p}}, \vec{\beta}) = -\frac{1}{1 - \frac{L^2 \ln(2)}{fwhm^2}} \left( \sum_{j=0}^k \beta_j \hat{p}_0^j \right) \sum_{i=1}^3 \hat{p}_i \cdot \vec{r}_{b,i} \quad (2.64)$$

This choice increases the scaling factor of the linear combination depending on the  $\hat{p}_0$  value. Thus, the radial coordinate increases with  $\hat{p}_0$ . Note that an expansion in arbitrary orders  $\hat{p}_0^k \hat{p}_1^l \hat{p}_2^m \hat{p}_3^n$  with the respective directional vectors could be used. This was not studied further in this work though.

In the case of the live position estimation in tracking, the estimator  $\hat{r}_{mLMS}^{(k=1)}(\hat{\vec{p}})$  was employed. The respective scaling parameters  $\vec{\beta}$  were chosen through tracking simulations as illustrated in sec. 4.1.2.

For  $\beta_0 = 1.27$  and  $\beta_1 = 3.8$  the resulting estimator performance is visualized in fig. 2.6. The beam geometry was set to the four-doughnut excitation beam pattern introduced in sec. 2.1.2 and eq. (2.37). It is evident from panel (B) that the mLMS estimator shows low bias values for a region with a diameter of approximately  $L/2$  surrounding the EBP center. For  $r \gtrsim L/4$  though, the bias starts to increase rapidly. The localization error is slightly higher than its CRB in the vicinity of the EBP center (see caption). For  $r \gtrsim L/4$  the mLMS error falls below its CRB. This is acceptable as the CRB is a bound for unbiased estimators only.

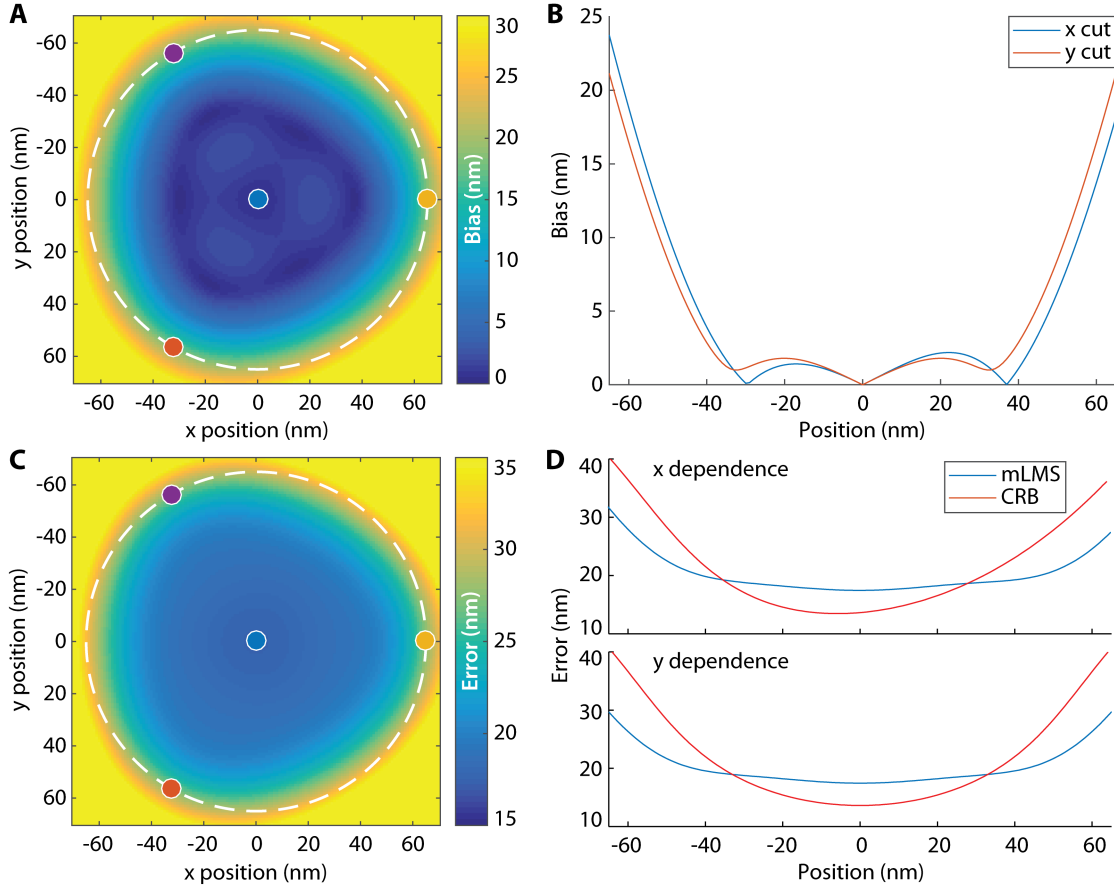


Figure 2.6: Performance of the mLMS estimator  $\hat{r}_{mLMS}^{(k=1)}$  for the four doughnut EBP of sec. 2.1.2 for a total of  $N = 10$  photons. The beam separation is set to  $L = 130$  nm and the  $fwhm$  to 450 nm. The  $\bar{\beta}$  parameters of the mLMS estimator are set to  $\beta_0 = 1.27$  and  $\beta_1 = 3.8$ . (A) Bias as a function of the position. The locations of the excitation doughnut zeros are visualized as colored dots and lie on a dashed circle with radius  $L/2$ . Up to a radial value of about  $r \lesssim L/4$  the estimator has low bias values. For larger distances from the EBP center the bias grows rapidly. (B) Bias as a function of the  $x$  position ( $y = 0$  nm) and as a function of the  $y$  position ( $x = 0$  nm). The low bias for  $r \lesssim L/4$  as well as the mentioned bias growth starting from  $r \gtrsim L/4$  is clearly visible. (C) Position dependence of the localization error. (D) Localization error along the  $x$  ( $y = 0$ ) and the  $y$  ( $x = 0$ ) direction. The localization error at the origin is about 17.5 nm which is slightly higher than its CRB with 13.6 nm. Due to the increasing bias, the mLMS error starts growing rapidly from about  $r \gtrsim L/4$  on. Nevertheless, it assumes smaller values than its CRB. The reason is that the estimator shows a small variance for  $r \gtrsim L/4$ , such that the error is primarily dominated by bias contributions. A biased estimator can show lower localization precision values than its CRB, as the latter is a bound for unbiased estimators only.



### Numerically unbiased mLMS (numLMS) estimator

The mLMSE estimator obtained in eq. (2.64) exhibits a simple functional form, and is fast to calculate. However, it has the drawback of being biased especially for localizations that are not in the proximity of the EBP center (see fig. 2.6). Additionally, experimental beam shapes might deviate slightly from their ideal counterparts of eq. (2.33) for which the mLMSE was calculated. The measured trajectories in the tracking application rely on the mLMSE. Consequently, they have to be corrected in post processing. Unfortunately, the MLE introduced in section 3.1.2 does not converge to the CRB in the photon range employed in tracking, where in average  $\langle N \rangle \approx 9$  photons were used per localization. Even for the  $\langle N \rangle \approx 150$  photons per localization employed in the application in chapter 3.4, the MLE does not achieve its CRB in the entire field of view (esp. for low  $L$ ).

In comparison to the MLE, the mLMSE has the advantage that performance metrics like the covariance and the bias can easily be calculated analytically. The knowledge of the bias enables the possibility of unbiasing the estimator. In the first step, the definition and derivation of the analytical bias of the mLMSE is presented. Subsequently, the routine that finds the optimal numerically unbiased mLMSE (numLMSE) is described.

Following the definition of eq. (2.54) the bias of the mLMSE is given by:

$$\text{bias}_{mLMS}^{(k)}(\bar{r}, \bar{\beta}) = \langle \hat{r}_{mLMS}^{(k)}(\hat{p}, \bar{\beta}) \rangle - \bar{r} \quad (2.65)$$

Note that the position estimate  $\hat{r}_{mLMS}^{(k)}$  is a function of the parameters  $\bar{\beta}$  and of the MLE  $\hat{p}$  parameter estimates  $\hat{p}$ . The latter is a function of the photon collection  $\bar{n}$  (see eq. (2.51)), where the expectation value  $\langle n_i \rangle$ , in turn, is a function of the position  $\bar{r}$ . To clarify this dependence, the expectation value of the position estimate  $\hat{r}_{mLMS}^{(k)}$  is renamed:

$$\bar{R}_{mLMS}^{(k)}(\bar{r}, \bar{\beta}) \equiv \langle \hat{r}_{mLMS}^{(k)}(\hat{p}, \bar{\beta}) \rangle \quad (2.66)$$

$$\bar{R}_{mLMS}^{(k)}(\bar{r}, \bar{\beta}) = -\frac{1}{1 - \frac{L^2 \ln(2)}{fwhm^2}} \sum_{j=0}^k \sum_{i=1}^3 \beta_j \langle \hat{p}_0^j \hat{p}_i \rangle \cdot \bar{r}_{b,i} \quad (2.67)$$

Equation (2.51) yields the identity  $\langle \hat{p}_0^j \hat{p}_i \rangle = \langle n_0^j n_i \rangle / N^{j+1}$ . The generalized factorial moments of the multinomial distribution  $\langle n_0^j n_i \rangle$  can be obtained from Mosimann (1962) - a selection of them is shown in table B.2. They lead to a closed ex-

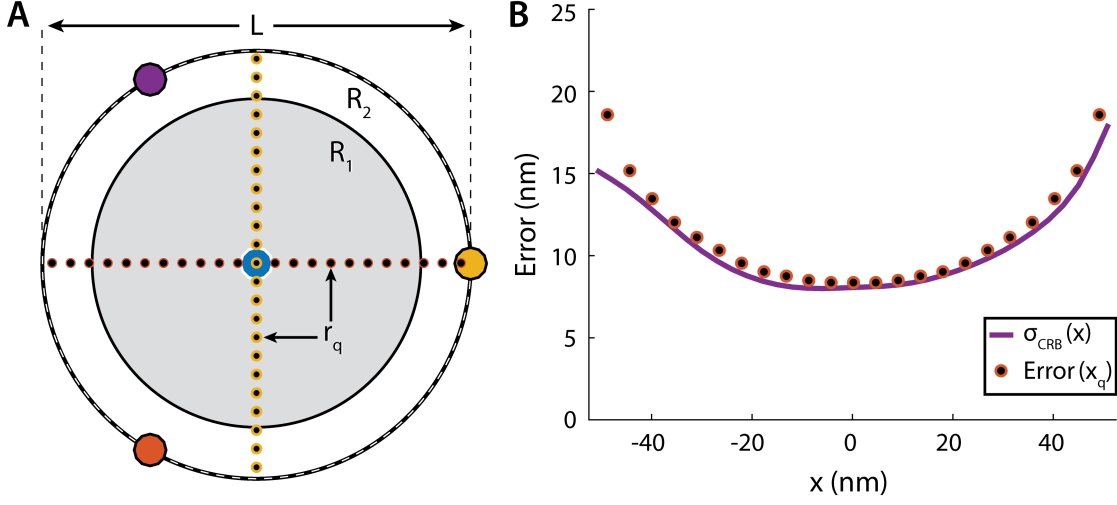


Figure 2.7: Visualization of the parameter used in the unbiasing routine. (A) Doughnut zeros of the excitation beam pattern are shown in thick colored dots.  $\mathcal{R}_2$  is the radius around the origin on which the estimator is unbiased and in which the query points  $\bar{r}_q$  lie. Here  $\mathcal{R}_2 = L/2$ . The radius  $\mathcal{R}_1$  is swept. It defines the region on which the mLMSE parameters  $\bar{\beta}$  is optimized on, and in which the interpolant function  $\mathcal{F}_{\mathcal{R}_1}$  is generated. (B) For each  $\mathcal{R}_1$  value, the mean localization error  $\sqrt{\text{MSE}(\bar{r}_q)}$  (see eq. (2.70)) is calculated for the query points and the deviation  $\mathbb{L}$  to the CRB  $\tilde{\sigma}_{CRB}$  obtained. Minimal deviation is achieved at  $\mathcal{R}_1 = \mathcal{R}_{opt}$ .

pression for  $\bar{R}_{mLMS}^{(k)}(\bar{r}, \bar{\beta})$ . Evaluated for  $k = 2$ , the mean localization  $\bar{R}_{mLMS}^{(2)}(\bar{r}, \bar{\beta})$  for an emitter at position  $\bar{r}$  with a total of  $N$  acquired photons is given by:

$$\begin{aligned} \bar{R}_{mLMS}^{(2)}(\bar{r}, \bar{\beta}) = & -\frac{1}{1 - \frac{L^2 \ln(2)}{fwhm^2}} \cdot \sum_{i=1}^3 \left( \beta_0 p_i(\bar{r}) + \right. \\ & \left. + \frac{N-1}{N} \left[ \beta_1 + \frac{\beta_2}{N} \right] p_0(\bar{r}) p_i(\bar{r}) + \frac{\beta_2 (N-1)(N-2)}{N^2} p_0^2(\bar{r}) p_i(\bar{r}) \right) \bar{r}_{b,i} \quad (2.68) \end{aligned}$$

It is of particular importance to note that for a given total photon number  $N$  and the success probability  $\bar{p}(\bar{r})$  of the four-doughnut excitation geometry, the function  $\bar{R}_{mLMS}^{(k)}(\bar{r}, \bar{\beta})$  is injective up to a maximal radius  $|\bar{r}|$  only. This maximal radius is a function of the scaling factors  $\bar{\beta}$  and, in particular, on the order  $k$ . However, to unbias  $\hat{r}_{mLMSE}^{(k)}$ , a unique mapping  $\bar{r} \rightarrow \bar{R}_{mLMS}^{(k)}(\bar{r}, \bar{\beta})$  needs to exist. Therefore, the area around the origin in which  $\bar{R}_{mLMS}^{(k)}(\bar{r}, \bar{\beta})$  can be unbiased is a function of  $\bar{\beta}$  and  $k$ . In this work,  $k = 2$  is chosen as a compromise, which enables unbiasing of the mLMSE in a radius of about  $L/2$  surrounding the origin.

In order to unbias  $\hat{r}_{mLMS}^{(k=2)}$  the following optimization routine is employed. It minimizes a loss function  $\mathbb{L}$  as subsequently defined.

1. Choose a value  $\mathcal{R}_2 \in \mathbb{R}$ , a set of positions  $\bar{r} \in \mathbb{R}^2$  and a set of query points  $\bar{r}_q \in \mathbb{R}^2$  with  $|\bar{r}_q| \leq \mathcal{R}_2$ . Here  $\mathcal{R}_2$  is the radial value of the area surrounding the origin in which the estimator is to be unbiased. The query points are the positions in which the routine is evaluated on.
2. Minimize the loss function  $\mathbb{L}(\mathcal{R}_1)$ , with  $\mathcal{R}_1 \in \mathbb{R}$  and  $\mathcal{R}_1 \leq \mathcal{R}_2$ . The loss function  $\mathbb{L}(\mathcal{R})$  is calculated as follows:

- (a) Obtain an optimal mLMSE in  $\mathcal{R}_1$ . Optimize  $\bar{\beta}$  such that the average bias  $\langle \text{bias}_{mLMS}^{(k=2)}(\bar{r}, \bar{\beta}) \rangle$  is minimized. The average is taken over all positions  $\bar{r}$ , with  $|\bar{r}| \leq \mathcal{R}_1$ . Let the optimal  $\bar{\beta}$ -vector be  $\bar{\beta}_{opt}$ .
- (b) Unbias the optimal mLMSE by generating an interpolant function  $\mathcal{F}_{\mathcal{R}_1}$  such that:

$$\begin{aligned} \mathcal{F}_{\mathcal{R}_1} : \mathbb{R}^2 &\rightarrow \mathbb{R}^2 \\ \mathcal{F}_{\mathcal{R}_1}(\bar{R}_{mLMS}^{(2)}(\bar{r}, \bar{\beta}_{opt})) &= \bar{r}, \quad \forall \bar{r} \text{ with } |\bar{r}| \leq \mathcal{R}_1 \end{aligned} \quad (2.69)$$

- (c) Test the generated unbiased estimator on the query points  $\bar{r}_q$ .
  - i. For each query point  $\bar{r}_q$ , generate a set of M  $\bar{p}$ -parameter estimates  $\hat{\mathcal{P}}_{\bar{r}_q} = \{\hat{p}_0, \dots, \hat{p}_M\}$ , and calculate the mLMSE  $\hat{r}_{mLMS}^{(k=2)}(\hat{p}, \bar{\beta}_{opt})$  for all  $\hat{p}$ -vectors of the set.
  - ii. Calculate the mean square error (MSE)

$$\text{MSE}_{\hat{\mathcal{P}}_{\bar{r}_q}}(\bar{r}_q) = \frac{1}{M} \sum_{i=1}^M \left( \mathcal{F}_{\mathcal{R}_1}[\hat{r}_{mLMS}^{(k=2)}(\hat{p}_i, \bar{\beta}_{opt})] - \bar{r}_q \right)^2 \quad (2.70)$$

with  $\hat{p}_i \in \hat{\mathcal{P}}_{\bar{r}_q}$ .

- iii. Calculate the loss function  $\mathbb{L}(\mathcal{R}_1)$

$$\mathbb{L}(\mathcal{R}_1) = \left\langle \left| \sqrt{\text{MSE}_{\hat{\mathcal{P}}_{\bar{r}_q}}(\bar{r}_q)} - \tilde{\sigma}_{CRB}(\bar{r}_q) \right| \right\rangle \quad (2.71)$$

where the average is taken over the set of query points  $\bar{r}_q$ . The Cramér-Rao bound  $\tilde{\sigma}_{CRB}$  is given by eq. (2.39).

3. Let the region  $\mathcal{R}_1$  minimizing the loss function  $\mathbb{L}$  be  $\mathcal{R}_{opt}$ . The numerically unbiased estimator is then given by:

$$\hat{r}_{numLMS}^{(k=2)}(\hat{p}) = \mathcal{F}_{\mathcal{R}_{opt}}[\hat{r}_{mLMS}^{(k=2)}(\hat{p}, \bar{\beta}_{opt})] \quad (2.72)$$

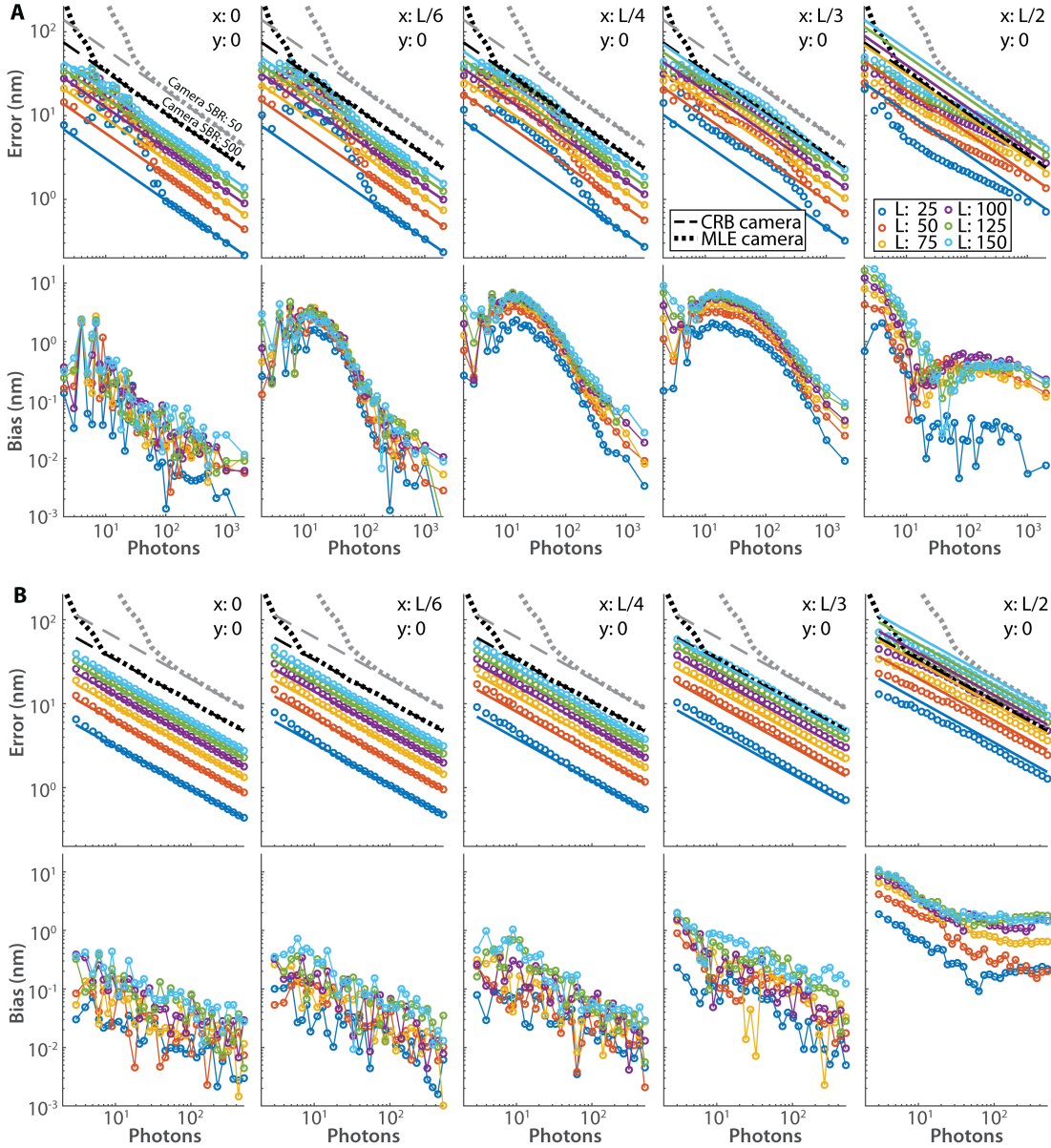


Figure 2.8: Estimator performance of the MLE and the numLMSE as a function of the number of photons  $N$  evaluated at different positions  $\vec{r} = [x, y]^T$  and for different  $L$  values. The EBP is given by eq. (2.37) (visualization in fig. 2.2 (A)), with  $\text{SBR} = 10$ . Every data point is obtained from  $10^4$  photon realizations  $\vec{n}$ , generated using multinomial statistics with parameter vector  $\vec{p}(\vec{r})$  as defined in eq. (2.10). The camera CRB and MLE were calculated as described in sec. 2.3, with two  $\text{SBR}_c$  values (50 (gray) and 500 (black)). Note that the camera performance describes *idealized* cameras. Read noise is not incorporated. **(A)** MLE error  $\sigma_{MLE}^{1D}$  and bias. The estimator converges only for  $N \gtrsim 50 - 500$  photons to the CRB (solid line), depending on the position and on  $L$  (units: nm). For smaller photon numbers, the MLE deviates considerably from its CRB. **(B)** NumLMSE performance: compared to the MLE, the divergence from the CRB is strongly reduced. The numLMSE performs better, especially for low photon numbers. Note that it was designed to work in a region  $|\vec{r}| \lesssim L/2$ . Figure adapted from Balzarotti et al. (2016).

A visualization of the parameter defined in the optimization routine can be found in fig. 2.7. In this work, the region  $\mathcal{R}_2$  in which the estimator is unbiased on is chosen to be  $\mathcal{R}_2 = L/2$ . The set of positions  $\bar{r}$  was a rectangular grid with spacing of 1 nm. The query points  $\bar{r}_q$  were equally spaced positions on the  $x$  and the  $y$  axis with  $x, y \leq L/2$ , respectively. To calculate  $\bar{\beta}_{opt}$  the optimization function “fmincon” of Matlab was used, where  $\beta_1$  was set to  $\beta_1 = 0$  per default. As interpolant  $\mathcal{F}$ , the “scatteredInterpolant” function from Matlab was employed. The set size  $M$  was chosen to be  $M = 10^4$ . The loss function  $\mathbb{L}$  was optimized using a grid search. Note that the mean localization  $\bar{R}_{mLMS}^{(k=2)}(\bar{r}, \bar{\beta})$  depends on the total number of photons  $N$  and on the parameter vector  $\bar{p}$  (see eq. (2.68)), and that  $\bar{p}$  in turn depends on the SBR (see eq. (2.10)). Therefore,  $\mathcal{R}_{opt}$  and  $\bar{\beta}_{opt}$  have a dependence on  $N$  and SBR. To reduce the computation time of the numLMS calculation,  $\mathcal{R}_{opt}(N, \text{SBR})$  and  $\bar{\beta}_{opt}(N, \text{SBR})$  were calculated only for some  $N$  and SBR values. Estimates of the optimal parameter for other combinations were inferred by 2D interpolation.

The performance of the resulting numLMS estimator is visualized in fig. 2.8. The localization error and the bias were evaluated numerically as a function of total photons  $N$  for different beam separations  $L$  and for different emitter positions. The localization error approaches its CRB asymptotically with  $N$  for all evaluated  $L$  values in the region  $|\bar{r}| \lesssim L/2$ . This is the region the numLMSE was designed to work in. Furthermore, the deviation for low  $N$  values is only small and strongly reduced compared to the MLE. Thus the construction of an estimator with close to optimal performance for low photon numbers, in the region surrounding the EBP origin, was successful. The dependence of the localization error as a function of the SBR is not explicitly shown; it was found to perform well for the evaluated range of  $\text{SBR} = 2 - 60$  though.

## 2.3 Idealized camera performance

Chapter 1 illustrated that camera localization is the most widely employed method in single molecule localization and tracking applications. Therefore, in this work the localization performance of MINFLUX is generally compared to camera localization performances. The applicability to single particle tracking, and especially the advent of superresolution microscopy, significantly increased the interest in the assessment of the localization performance for state-of-the-art camera detectors. The CRB for a Poissonian signal and different PSF shapes (e.g. Gaussian- and

Airy-profiles), including the camera pixel size as well as Poissonian and Gaussian noise contributions, was formulated (Ober et al., 2004), and awareness of this measure as the lower bound of localization precision increased (Deschout et al., 2014; Chao et al., 2016). Furthermore, the localization precision achievable by employing different estimators (e.g. fitting of a 2D Gaussian to the PSF) were evaluated (Thompson et al., 2002; Mortensen et al., 2010; Small and Stahlheber, 2014).

In this section, the CRB and the MLE performance are evaluated for a Gaussian PSF and an ideal camera. Effects of pixelation and additive Poissonian noise (originating, for example, from sample background contributions) are taken into account. Current camera technologies have additional noise sources (e.g. read noise and EM excess noise) that worsen the camera performance. These are neglected, given that they make the model more complicated and become less relevant as camera technologies improve. The following results can therefore be seen as a lower bound on the camera performance. Furthermore, the conditioning to  $N$  detected total photons is considered in order to be consistent with the CRB results derived so far. To this end, the theory already developed in sec. 2.1 is used.

### 2.3.1 Fisher information and Cramér-Rao bound

The emitter photons reaching the camera detector follow Poissonian statistics. Let the parameter of that distribution be  $\lambda_{tot}^{(m)}$ , where the superscript ( $m$ ) indicates emitter photons. A camera pixel  $i$  will see only a fraction of the incoming photons with mean  $\lambda_i^{(m)}$ , such that we get in an ideal case of no losses  $\lambda_{tot}^{(m)} = \sum_i \lambda_i^{(m)}$ .

The value of  $\lambda_i^{(m)}$  will depend on the shape and position of the fluorescence diffraction pattern  $I_{PSF}$ . Approximating this PSF by a normalized 2D symmetric Gaussian function with standard deviation  $\sigma_{PSF}$  yields

$$I_{PSF}(x, y) = \frac{1}{2\pi\sigma_{PSF}^2} e^{-\frac{1}{2}\left(\frac{x-x_m}{\sigma_{PSF}}\right)^2} e^{-\frac{1}{2}\left(\frac{y-y_m}{\sigma_{PSF}}\right)^2} \quad (2.73)$$

where  $\vec{r}_m = [x_m, y_m]^T$  is the position of the emitter. For a square shaped pixel with side length  $a$  and center at  $\vec{r}_i = [x_i, y_i]^T$  we get:

$$\lambda_i^{(m)} = \lambda_{tot}^{(m)} \int_{x_i-a/2}^{x_i+a/2} \int_{y_i-a/2}^{y_i+a/2} I_{PSF}(x, y) dx dy \quad (2.74)$$

The probability  $P(\vec{n})$  to measure  $n_i$  photons on pixel  $i$  is given by eq. (2.2). Constraining the total number of photons to  $N$  yields multinomial statistics, with probability function  $P(\vec{n} | N, \vec{p}^{(0)}(\vec{r}_m))$  given by eq. (2.11). This function de-

describes the probability of measuring  $n_i$  photons in pixel  $i$ , given a total of  $N$  photons and an emitter at  $\bar{r} = \bar{r}_m$ . The parameter vector  $\bar{p}^{(0)}$  (see eq. (2.6)) is given by

$$\begin{aligned} p_i^{(0)}(\bar{r}_m) &= \frac{\int_{x_i-a/2}^{x_i+a/2} \int_{y_i-a/2}^{y_i+a/2} I_{PSF}(x, y) dx dy}{\int_{x_{min}-a/2}^{x_{max}+a/2} \int_{y_{min}-a/2}^{y_{max}+a/2} I_{PSF}(x, y) dx dy} \\ &\approx \int_{x_i-a/2}^{x_i+a/2} \int_{y_i-a/2}^{y_i+a/2} I_{PSF}(x, y) dx dy \end{aligned} \quad (2.75)$$

where  $[x_{min}, y_{min}]$  and  $[x_{max}, y_{max}]$  are the coordinates of the outer border of the  $K$  pixel sized region. The approximation is valid as long as the relevant support of the  $PSF$  of eq (2.73) overlaps with the  $K$  pixel sized region of the camera.

If Poissonian background contributions are to be included, the  $\bar{p}$  parameter vector of eq. (2.75) has to be adapted. To that end it makes sense to define a signal-to-background ratio for the camera ( $SBR_c$ ):

$$SBR_c = \frac{\lambda_{tot}^{(m)}}{\lambda^{(b)}/K} \quad (2.76)$$

Here  $\lambda_{tot}^{(m)}$  is the mean total emitter signal reaching the camera and  $\lambda^{(b)}$  is the mean background signal in a small region of  $K$  pixel around the emitter position. It can be thought of as mean-signal-to-mean-background ratio per pixel.

The signal detected by a pixel is now given by a contribution from the emitter with Poissonian mean  $\lambda_i^{(m)}$  and a Poissonian background contribution  $\lambda^{(b)}/K$ . As the sum of random variables that follow Poissonian statistics is again Poissonian, we get:

$$\lambda_i = \lambda_i^{(m)} + \lambda^{(b)}/K \quad (2.77)$$

Using the  $SBR_c$  definition of eq. (2.76) and eq. (2.6) with  $\lambda_i$  given by eq. (2.77), we get the following  $\bar{p}$  parameter vector

$$p_i(\bar{r}_m) = \frac{1}{K + SBR_c} + \frac{SBR_c}{K + SBR_c} \cdot p_i^{(0)}(\bar{r}_m) \quad (2.78)$$

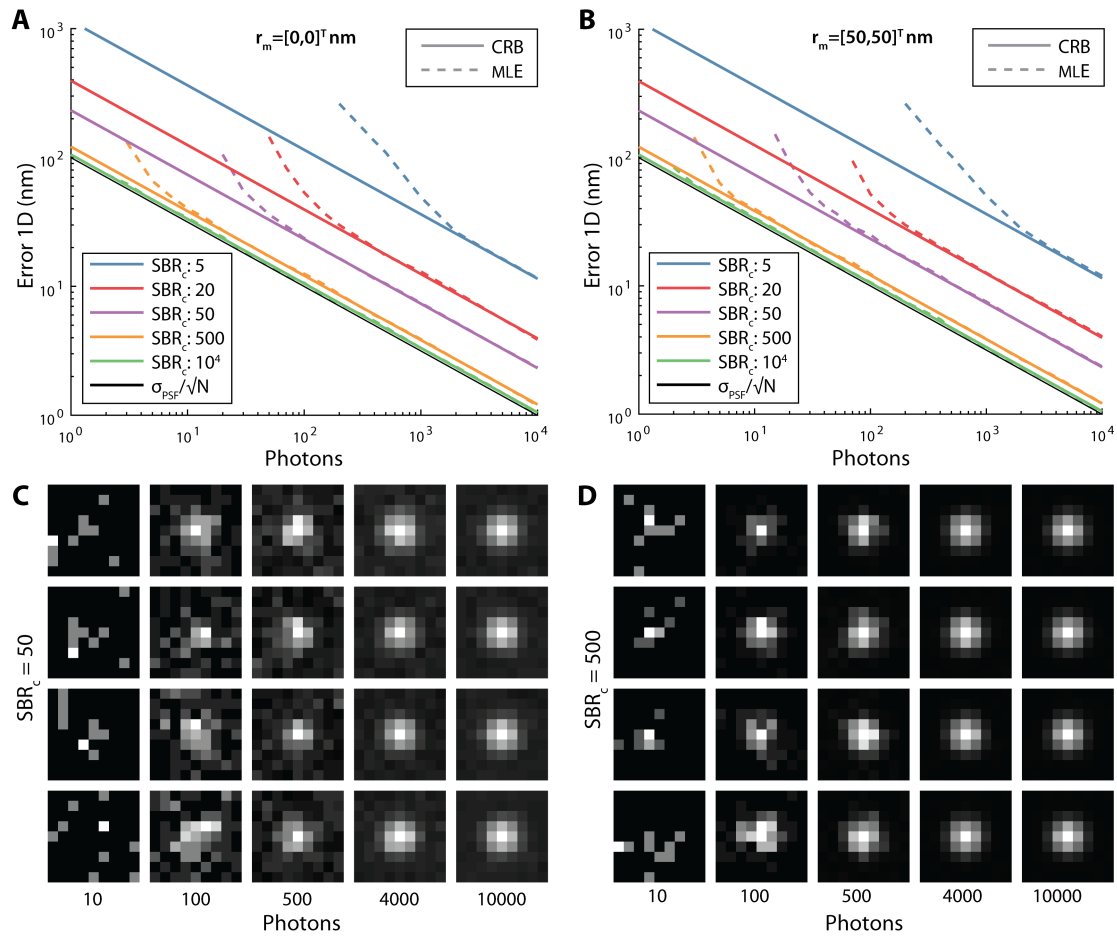


Figure 2.9: (A-B) Ideal camera performance for single emitter localization. The CRB  $\tilde{\sigma}_{CRB}$  (solid lines) as well as the MLE (dashed lines) performance are shown for  $\sigma_{PSF} = 100$  nm and  $K = 9 \times 9$  pixel with size  $a = 100$  nm for two emitter positions  $\bar{r}_m = [0, 0]$  and  $\bar{r}_m = [50, 50]$  nm. Additionally,  $\sigma_{PSF}/\sqrt{N}$ , the CRB for an infinite SBR that neglects the performance-deteriorating pixel size is visualized. (C-D) Examples of simulated normalized camera images visualizing the influence of  $SBR_c$  values for a different total number of acquired photons  $N$ . The pixel size as well as  $\sigma_{PSF}$  are the same as in (A). The emitter location is always in the center of the image. Figure adapted from Balzarotti et al. (2016).



where  $p_i^{(0)} = \lambda_i^{(m)} / \sum_j \lambda_j^{(m)}$  is given by eq. (2.75). Inserting the latter and solving the integral yields:

$$\begin{aligned} \Rightarrow p_i(\bar{r}_m) = & \frac{1}{K + \text{SBR}_c} + \frac{\text{SBR}_c}{K + \text{SBR}_c} \\ & \cdot \frac{1}{4} \left[ \text{erf} \left( \frac{x_i + a/2 - x_m}{\sqrt{2}\sigma_{PSF}} \right) - \text{erf} \left( \frac{x_i - a/2 - x_m}{\sqrt{2}\sigma_{PSF}} \right) \right] \\ & \cdot \left[ \text{erf} \left( \frac{y_i + a/2 - y_m}{\sqrt{2}\sigma_{PSF}} \right) - \text{erf} \left( \frac{y_i - a/2 - y_m}{\sqrt{2}\sigma_{PSF}} \right) \right] \end{aligned} \quad (2.79)$$

Given that the underlying statistics of  $P(\bar{n} | N, \bar{p})$  follow multinomial statistics, the Fisher information and the CRB  $\tilde{\sigma}_{CRB}$  can be obtained from eq. (2.17) and eq. (2.19), with  $d = 2$  and  $K$  the number of pixels considered. Typically,  $K = 9 \times 9$  pixels with size  $a = 100$  nm is used. Results of numerical calculations of  $\tilde{\sigma}_{CRB}$  for relevant  $\text{SBR}_c$  values are shown in fig. 2.9 (A). The decrease and convergence of  $\tilde{\sigma}_{CRB}$  with increasing  $\text{SBR}_c$  values is clearly visible. Note also that the CRB for the chosen pixel size and for  $\text{SBR}_c = 500$  is close, and for  $\text{SBR}_c = 10^4$  very close to  $\sigma_{PSF}/\sqrt{N}$ , the CRB for an infinite SBR that neglects the performance deteriorating pixel size (Ober et al., 2004).

Furthermore, it is evident from fig. 2.8 (A-B) that the camera performance is considerably worse compared to the MINFLUX performance. Here camera parameters were set to  $\sigma_{PSF} = 87$  nm and  $K = 9 \times 9$  pixel with size  $a = 100$  nm. Theory predicts a MINFLUX localization precision of about 1 nm when using  $N = 500$  photons and  $L = 50$  nm with a signal-to-background ratio of  $\text{SBR} = 3$ . The camera would need a factor of about 22 times more photons to reach the same precision for a signal-to-background ratio of  $\text{SBR}_c = 500$ .

### 2.3.2 Maximum likelihood estimator

As mentioned in sec. 2.2, the CRB provides a value for the best possible performance that any unbiased estimator can achieve, but does not provide information on the actual performance of a chosen estimator. Thus, in addition to the CRB the maximum likelihood position estimator performance is to be evaluated. The MLE is chosen, as it is known to be consistent and efficient in the limit of high photon numbers (see sec. 2.2.1).

The likelihood function  $\mathcal{L}(\bar{r}_m | \bar{n}, N) = P(\bar{n} | N, \bar{p}(\bar{r}_m))$  that needs to be maximized is given by eq. (2.11) with  $\bar{p}$  parameter vector of eq. (2.79). To determine the maximum likelihood position estimator  $\hat{r}_m^{MLE}$ , the likelihood function is evaluated numerically. This is accomplished by use of a grid search, with successively smaller grid spacing (typically 5 nm, 0.5 nm, 0.1 nm and 0.01 nm). To quantify the MLE performance, a collection of 1000 simulated images was generated for different combinations of emitter positions  $\bar{r}_m$ ,  $SBR_c$  and number of photons  $N$  values, respectively. A representative selection for an emitter at  $\bar{r}_m = \bar{0}$  is visualized in fig. 2.9 (C-D). For each generated image the MLE estimate  $\hat{r}_m^{MLE}$  was determined. To this end, the  $\bar{p}$  parameter vector was assumed to be known exactly, i.e. the  $SBR_c$  as well as the PSF are assumed to be precisely identified. Subsequently, the error defined in eq. (2.57) was calculated for each parameter combination. The resulting performance of the MLE is shown in fig. 2.9 (A) for  $\bar{r}_m = \bar{0}$  and in (B) for  $\bar{r}_m = [50, 50]^T$ . Thus, the emitters were placed in the center of a pixel and at the cross section of a neighboring pixel. Deviations to the CRB can especially be seen for a low number of photons. In the high photon regime, the MLE converges to the MLE which is in agreement with the MLE being efficient.

It should be stressed that the successful application of a MLE for a real imaging system requires precise knowledge of the  $\bar{p}$  parameter vector, and therefore of the PSF shape and especially the noise of the system (especially the camera). Wrong assumptions will deteriorate the MLE performance (Huang et al., 2013).

## 2.4 Summary and discussion

In section 2.1 of this chapter a general framework was developed to calculate the MINFLUX Cramér-Rao bound (CRB) on the position estimator. The CRB is a lower bound on the variance of any unbiased estimator, thus defining its optimal performance. In this case the theoretical limit on the localization precision was studied in an arbitrary number of spatial dimensions with an arbitrary number of excitation beams. The multinomial success probability  $\bar{p}$  that defines the probability of measuring a given photon collection  $\bar{n}$ , and the total photon number  $N$  were identified as the key parameters on which the CRB depends. Furthermore, the influence of Poissonian background contributions on  $\bar{p}$  were discussed.

The theoretical framework was employed to study different 1D and 2D excitation geometries. Section 2.1.2 illustrated that the properties of the CRB can be tuned by the choice of adequate excitation beam patterns (EBP). The evaluated patterns were comprised of displaced excitation profiles that featured an intensity zero. The beam separation was characterized by a separation parameter  $L$  and was found to have a strong impact on the CRB. It turned out that for a given photon-budget, the reduction of  $L$  decreased the CRB in the field of view between the intensity zeros. Unlike in camera localization, the localization precision was not isotropic and also showed a dependence on the position. The minimum of the CRB was at the center of the field of view (termed EBP origin). It was shown that the MINFLUX CRB at this origin is truly unlimited for a given photon-budget in the case of no background contributions. This was demonstrated in one and two dimensions. In summary, MINFLUX enabled to increase the photon-efficiency of the localization process by means of geometrical degrees of freedom.

The presence of background contributions increased the value of the CRB and, most importantly, they introduced a limit to the beam separation  $L$  until which the CRB can be beneficially reduced. Thus, the presence of background established a lower boundary to MINFLUX.

The possible excitation patterns are not restricted to the evaluated examples. The utilization of non-equal excitation profiles with a variable amount of exposures promises great flexibility on the properties of the CRB. These could be adapted to specific applications, optimizing aspects like field of view, isotropy, speed and localization precision. In this dissertation I focus on the benefits that multiple doughnut shaped excitation profiles offer towards single molecule localization.

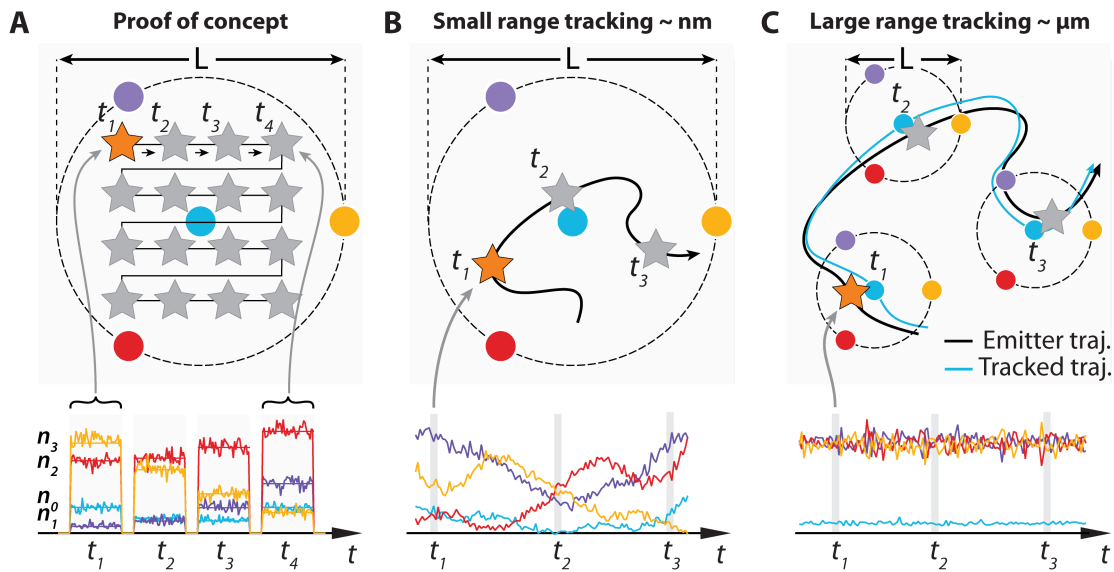


Figure 2.10: **(A)** In order to verify the MINFLUX concept experimentally, an isolated single emitter is localized repeatedly at multiple positions in the field of view. The fluorescence photons  $[n_0, \dots, n_3]$  detected for each doughnut excitation are used to estimate the emitter position. The resulting localization error is compared to the Cramér-Rao bound. **(B)** MINFLUX can be used to localize a single emitter that moves within the region of size  $L$ . The increased photon-efficiency promise higher time resolution at equal localization error. **(C)** If the emitter leaves the initial field of view of diameter  $L$ , the EBP is (iteratively) displaced to the last estimated position of the molecule. By keeping it in the EBP center by means of a feedback loop, photon emission is expected to be minimal for  $n_0$  and balanced between  $n_1$ ,  $n_2$  and  $n_3$ , as shown. Figure adapted from Balzarotti et al. (2016).

The CRB provides the best possible localization performance that any unbiased estimator can achieve. However, it does not provide information on the actual performance of a chosen estimator. Therefore, section 2.2 evaluated the performance of the maximum likelihood estimator (MLE) and of other estimators, e.g. the numLMSE. Explicit expressions for the MLE position estimation were derived for 1D excitation geometries. The 2D MLE of an EBP using four doughnut beams was evaluated numerically. This is the main excitation geometry used in this dissertation. For high  $N$  values the MLE asymptotically approached its CRB in all evaluated instances. For low photon numbers though, the MLE broke. It deviated strongly from its CRB. This was the main reason for the construction of the numLMS estimator. It was optimized numerically and showed close to optimal performance also for low photon numbers ( $\sim 10$ ) in the field of view surrounding the EBP origin. In order to employ these estimators, the spatial dependence of the success probability needs to be known.

Furthermore, the CRB and the MLE of an ideal camera were evaluated in section 2.3 for a Gaussian detection PSF and different signal-to-background ratios  $SBR_c$ . In order to be compatible with the precedent theoretical framework, the localization performance was evaluated by conditioning the total detected photons to  $N$ . The deteriorating effect of  $SBR_c$  on the CRB was illustrated. As expected, the MLE converged to the CRB for large  $N$ . At small photon numbers the MLE localization error departed from its CRB though. Comparing the camera localization error at a given photon-budget  $N$  to the MINFLUX performance showed that the MINFLUX photon-efficiency is considerably increased especially close to the EBP origin.

In the following chapter the theoretical results obtained for the MINFLUX concept are evaluated experimentally. To this end, an isolated single ATTO 647N molecule is localized at different positions throughout the field of view, as shown in fig. 2.10 (A). Some application modalities of MINFLUX comprise the localization of a single emitter dynamically moving inside of the field of view as shown in fig. 2.10 (B) as well as the tracking of a diffusing single emitter by iteratively repositioning the field of view (fig. 2.10 (C)). These modalities are applied and evaluated in chapter 3 and chapter 4.



# Chapter 3

## Single emitter localization using MINFLUX

In this chapter the theoretical results of the MINFLUX concept are verified experimentally in two dimensions. To that end, a single point-like emitter is localized repeatedly when excited with the excitation beam pattern (EBP) consisting of four doughnuts introduced in sec. 2.1.2. MINFLUX localization estimates are obtained from the maximum likelihood estimator (MLE) (see sec. 2.2.1) as well as from the numLMS estimator that was optimized for low photon applications (see sec. 2.2.2). The resulting localization performance is compared to the Cramér-Rao lower bound (CRB) of the employed excitation geometry as well as to the CRB and the MLE performance of an ideal camera (see sec. 2.3). In order to calculate the localization estimates, the multinomial success probability  $\bar{p}$  needs to be characterized experimentally. A detailed protocol on how this was achieved is presented in sec. 3.2.

Subsequently, the MINFLUX concept is applied to resolve the fast dynamics of a custom made DNA origami sample in sec. 3.4. MINFLUX localization estimates are thereby obtained from the numLMS estimator. The achievable localization precision is evaluated down to sub-millisecond timescales and compared to the CRB.

This chapter begins by introducing the experimental setup that was built. It is used for the following measurements as well as for measurements of the single emitter tracking application of chapter 4.

## 3.1 Optical setup

The setup consists of a home built laser scanning microscope with fast beam positioning and modulation capabilities. It is visualized as schematic in fig. 3.1. A detailed description of the setup components as well as of its functionality follows in this section.

### Excitation PSF and amplitude modulation

Excitation of the sample can be performed by either 642 nm excitation with Laser 1 [*VFL-P-1500-642*, MPB Communications Inc., Pointe-Claire, Quebec, Canada or *Koheras SuperK Extreme*, NKT Photonics, Birkerød, Denmark] or by 561 nm excitation with Laser 2 [*Cobolt Jive<sup>TM</sup>*, Cobolt AB, Solna, Sweden]. The power of the 642 nm laser is controlled by an acousto optical tunable filter (AOTF) [*AOTFnC VIS*, AA Sa, Orsay, France]. The beam is focused using an oil immersion microscope objective [*HCX PL APO 100x/1.40-0.70 Oil CS*, Leica Microsystems GmbH, Wetzlar, Germany] to a Gaussian or doughnut shaped excitation PSF with circular polarization. The doughnut is generated by a vortex phase plate (VPP) [*VPP-1a*, RPC Photonics, Rochester, NY, USA]. Switching between both beam profiles as well as fast amplitude modulation is realized by electro-optical modulators (EOM) [*LM 0202 P 5W & LIV 20*, Qioptiq Photonics GmbH & Co. KG, Göttingen, Germany].

### Beam steering components

Fast lateral scanning of the excitation profiles is performed by two orthogonal non-descanned electro-optical deflectors (EOD<sub>x</sub> and EOD<sub>y</sub>) [*M-311-A*, Conoptics Inc., Danbury, CT, USA]. Each deflector is driven by two high voltage amplifiers in a differential arrangement [*PZD700A*, Trek Inc., Lockport, NY, USA & *WMA-300*, Falco Systems BV, Amsterdam, The Netherlands]. The first amplifier provides a bandwidth of 5 MHz and a scanning range of  $\pm 150$  nm. It is mainly employed for fast beam multiplexing in order to generate the time shifted EBP (see fig. 3.2). The second amplifier provides a bandwidth of 125 kHz and a field of view of  $\pm 1$   $\mu$ m. It is mainly used for PSF measurements as well as to follow high frequency movement of an emitter in the tracking application. The low frequency movement is tracked by a descanned tip/tilt mirror [*PSH-10/2 & EVD300*, both piezosystem jena GmbH, Jena, Germany] with 1 kHz bandwidth and a  $20 \times 30$   $\mu$ m scan range. All scanners are controlled by a field programmable gate array board (FPGA) [*NI PCIe-7852R*,



National Instruments, Austin, TX, USA]. To separate the two frequency regimes, a filter bank with a standard first order low pass filter with a time constant of 10 ms was used. The sample is mounted on a piezoelectric stage [*P-733.3-DD* & *E725*, both Physik Instrumente (PI) GmbH & Co. KG, Karlsruhe, Germany] which allows accurate positioning in three dimensions.

### Stage lock

The stage position is stabilized by a stage lock that measures the drift in all three dimensions and corrects for it. Axial stage position measurements are done using the total internal reflection (TIR) of the infrared (IR) beam of Laser 6 [*LP980-SF15*, Thorlabs Inc., Newton, NJ, USA]. The IR beam is spectrally filtered by F4 [*LL01-980-12.5*, Semrock Inc., Rochester, NY, USA & *FB980-10*, Thorlabs Inc., Newton, NJ, USA]. Separation of the IR laser from the excitation laser and the fluorescence signal is realized using a dichroic mirror DM2 [*BB1-E02P*, Thorlabs Inc., Newton, NJ, USA]. The IR beam is focused off center in the back focal plane of the objective lens, and the TIR signal is measured with Camera 2 [*DMK 22BUC02*, The Imaging Source Europe GmbH, Bremen, Germany, CMOS camera, acquisition rate set to 90 fps]. The center of mass of the acquired image is a measure for the axial stage position. Thus, fixing the center of mass coordinates in the image enables stabilization of the axial stage position. Lateral stage position measurements are conducted by dark field imaging of immobilized scattering nanorods. The scattered signal as well as the TIR signal are spectrally filtered by F3 [*FEL850*, Thorlabs Inc., Newton, NJ, USA]. Images are recorded with Camera 3 [Same as Camera 2, acquisition rate set to 160 fps], and fitted using a 2D Gaussian function. All images are exponentially averaged. Stabilization is realized by commanding the *xyz* piezo stage using a PI feedback loop implemented in LabView. The loop update rate is set to 10 Hz.

### Fluorescence detection

The emitter fluorescence signal is measured in back-scattering geometry. A dichroic mirror DM1 separates the fluorescence from the excitation light. Furthermore, the collected fluorescence is spectrally filtered by F1 or F2 and imaged by Camera 1 [*Luca S*, Andor Technology Ltd., Belfast, UK, EMCCD camera] or detected by APD 1 or 2 [*SPCM-AQRH-13-FC*, Excelitas Technologies, Waltham, MA, USA]. The APDs are coupled to multimode fibers which act as a detection pinhole for spatial filtering. APD 1 detects a 400 nm field of view in the sample plane and

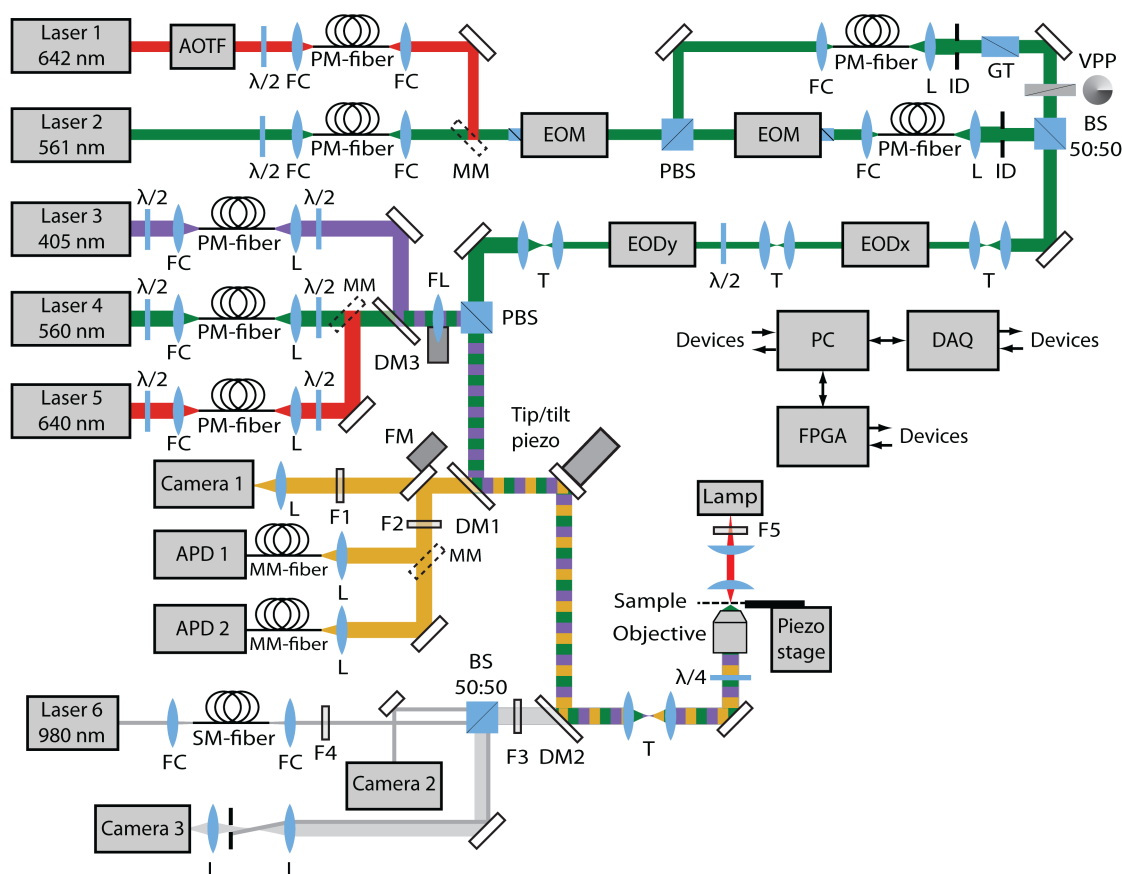


Figure 3.1: Schematic illustration of the experimental setup. The components not described in the text are:  $\lambda/2$ : half wave plate (B. Halle Nachfl. GmbH, Berlin, Germany),  $\lambda/4$ : quarter wave plate (B. Halle Nachfl. GmbH, Berlin, Germany), *FC*: fiber collimator 60FC (Schäfter + Kirchhoff, Hamburg), *MM*: mirror on magnetic mount, *PM-fiber*: polarization maintaining fiber (Thorlabs Inc., Newton, NJ, USA or Schäfter+Kirchhoff, Hamburg, Germany), *SM-fiber*: single mode fiber (Thorlabs Inc., Newton, NJ, USA), *MM-fiber*: multimode fiber (M31L01, Thorlabs Inc., Newton, NJ, USA), *PBS*: polarizing beam splitter cube (B. Halle Nachfl. GmbH, Berlin, Germany), *GT*: Glan-Thompson prism (B. Halle Nachfl. GmbH, Berlin, Germany), *BS*: beam splitter cube 50 : 50 (B. Halle Nachfl. GmbH, Berlin, Germany), *L*: achromatic lens with VIS or NIR AR coating (Thorlabs Inc., Newton, NJ, USA or Qioptiq Photonics GmbH & Co. KG, Göttingen, Germany), *T*: telescope, *FL*: lens on flip mount, *FM*: mirror on motorized flip mount, *ID*: iris diaphragm, *Lamp*: LQ 1100 (Fiberoptic – Helm AG, Bühler, Switzerland), *PC*: personal computer running Windows 7 (Microsoft Corp., Redmond, WA, USA) and LabView 2013 (National Instruments, Austin, TX, USA). Figure adapted from Balzarotti et al. (2016).

is used in the proof-of-concept measurements of this chapter. As it is nearly confocalized, it offers a good background suppression. APD 2 detects a bigger field of view of  $2\ \mu\text{m}$  and is employed in the tracking application. This APD covers the complete scanning range of the non-descanned EODs. Switching between the camera and the APDs is done with a mirror on a motorized flip mount. The filter chosen depends on the excitation wavelength.

#### **Filter for 642 nm excitation**

**DM1** *Z488/633RDC*, Chroma Technology Corp., Bellows Falls, VT, USA

**F1** *FF01-635/LP-25* & *FF01-842/SP-25*, Semrock Inc., Rochester, NY, USA

**F2** *ET700/75m* & *ZET642NF*, Chroma Technology Corp., Bellows Falls, VT, USA & *FF01-775/SP-25*, Semrock Inc., Rochester, NY, USA

#### **Filter for 561 nm excitation**

**DM1** *ZT405/488/561*, Chroma Technology Corp., Bellows Falls, VT, USA

**F1** *BLP02-561R-25*, Semrock Inc., Rochester, NY, USA & *FF01-842/SP-25*, Semrock Inc., Rochester, NY, USA

**F2** *BLP02-561R-25*, Semrock Inc., Rochester, NY, USA & *FF01-775/SP-25*, Semrock Inc., Rochester, NY, USA

#### **Measurement control software**

Measurements are performed with custom programs written in LabView [National Instruments, Austin, TX, USA]. These programs control the devices directly via the data acquisition (DAQ) boards [*NI PCIe-6353* & *NI PCI-6259*, both National Instruments, Austin, TX, USA, & *USB-3103*, Measurement Computing Corporation, Norton, MA, USA] or the FPGA board. The main tasks of the software are:

- controlling the laser beam position and modulation of its amplitude.
- multiplexing the beam positions to generate the EBP. To make sure that the emitter is not excited during the beam repositioning phase, the excitation laser is turned off during that phase. The multiplex cycle is visualized in fig. 3.2.

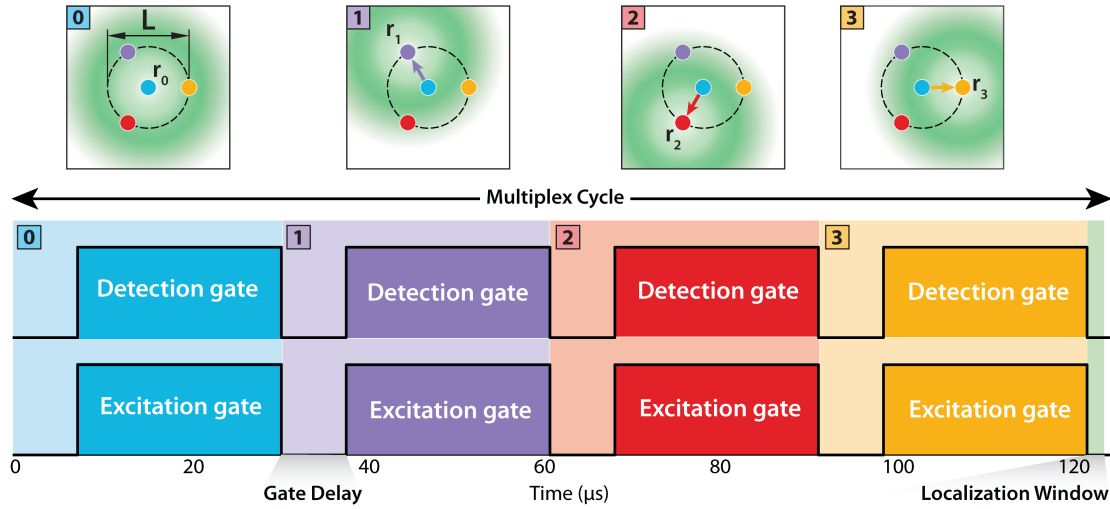


Figure 3.2: Visualization of the multiplex cycle. An FPGA board controls the amplitude modulation and deflection of the laser beam as well as the collection of the fluorescence photon-counts. The excitation is gated by EOMs in order to assure that the fluorophore is not excited during the beam repositioning. The off time is given by the gate delay. Photons are acquired only if the detection gate is enabled. The delay of the latter is equal to the gate delay. After four successive exposures, a live position estimation can be calculated employing the FPGA board. The calculation time slot is given by the localization window (green). Note that the multiplex cycle is visualized using the excitation pattern described in sec. 2.1.2, but is not restricted to it. Figure reproduced from Balzarotti et al. (2016).

- acquire the detected photons from the APDs.
- perform a live position estimation using the mLMSE introduced in sec. 2.2.2 and reposition the EBP in the tracking application.
- control the stage lock as already described.
- save the recorded data.

### Widefield and activation laser

Additional excitation wavelengths are given by Laser 3-5. Laser 3 at 405 nm [405-50-COL-004, Oxxius, Lannion, France] is used for photo-activation in the tracking application. Laser 4 at 561 nm [VFL-P-1000-560, MPB Communications Inc., Pointe-Claire, Quebec, Canada] and Laser 5 at 640 nm [LDH-D-C-640, PicoQuant, Berlin, Germany] are used as widefield illumination. To generate the widefield, a lens on a flip mount (FL) can be introduced into the beam path. Combination of the different beam path is realized with the dichroic mirror DM3 [Z500RDC-XT, Chroma Technology Corp., Bellows Falls, VT, USA]. Furthermore, a lamp enables

generation of transmission images. It is spectrally filtered by F5 [*Z635/10*, Chroma Technology Corp., Bellows Falls, VT, USA] in order not to excite the fluorescent protein used in the tracking application.

## 3.2 The multinomial success probability

The MINFLUX concept requires precise knowledge of the position dependence of the multinomial success probability  $\bar{p}$ . This is evident from both position estimators employed. In order to obtain a position estimate from the photon collection  $\bar{n}$ , the MLE maximizes the likelihood function  $\mathcal{L}(\bar{r} | \bar{n})$  that depends on  $\bar{p}$  (see eq. (2.47), (2.55)). The numLMS estimator is unbiased using the expectation value of the mLMS position estimate that is also a function of  $\bar{p}$  (see eq. (2.69), (2.68) and (2.66)). The success probability  $\bar{p}$  in turn depends on the signal-to-background ratio (SBR) and on the excitation PSF as derived in eq. (2.10) and eq. (2.7). Thus, a precise excitation PSF measurement is required. This is realized by scanning the excitation beam over a 20 nm fluorescent microsphere. The sample preparation followed by the PSF measurement and the derivation of the multinomial success probability is subsequently discussed.

### 3.2.1 Sample preparation

#### Coverslip and objective slide cleaning

For single emitter imaging it is necessary to clean the coverslips and microscope slides in order to reduce fluorescence contributions from unwanted fluorescent particles. Prior to sample preparation, the coverslips were therefore treated with a 2% Hellmanex<sup>®</sup> III (Hellma GmbH & Co. KG, Müllheim, Germany) dilution in Milli-Q water. They are embedded in the solution using a homemade Teflon holder and sonicated twice for 15 min. After the first sonication step, the coverslips are rinsed with Milli-Q and embedded into a fresh Hellmanex<sup>®</sup> III dilution. After the second sonication, Milli-Q rinsing is repeated and the coverslips are dried with compressed N<sub>2</sub>. The microscope slides are cleaned following the same procedure but with only one 15 min sonication step.

#### Nanorod immobilization

In order to use the lateral stage stabilization described in sec. 3.1, Au nanorods with a maximum scattering cross section at 980 nm (*A12-25-980*, Nanopartz Inc.,

Loveland, CO, USA) are immobilized on the coverslip. In the first step the nanorod stock solution is sonicated for 5 min, then vortexed for about 10 s and diluted 1 : 3 in Milli-Q water. Subsequently,  $10\ \mu\text{l}$  of the diluted solution is applied to the coverslip and rinsed with Milli-Q after about 1 min of incubation. The coverslips are dried with compressed  $\text{N}_2$ .

### Obtaining flow channels

Samples in this chapter are prepared using self-assembled flow channels. They enable the fixation of the coverslip on the microscope slide and provide an easily accessible flow channel of selectable width. Flow channels are formed by gluing two double sided tape strips (Double Sided Tape,  $12\ \text{mm} \times 6.5\ \text{mm}$ , 3 m, Scotch<sup>®</sup>, France) parallel to each other on the microscope slide. The spacing between the strips defines the flow channel volume. The coverslip is placed on top of the strips for fixation.

### Immobilized single fluorescent microspheres

Fluorescent microspheres were mainly employed to measure the excitation PSF. To immobilize them, a clean coverslip with Au nanorods is coated with  $50\ \mu\text{l}$  0.01% Poly-L-Lysine (Sigma-Aldrich) solution. After about 5 min the coverslip is rinsed off with Milli-Q water and dried with compressed  $\text{N}_2$ . The 20 nm fluorescent microspheres (*FluoSpheres*<sup>®</sup>,  $0.02\ \mu\text{m}$ , dark red fluorescent, Thermo Fischer Scientific Inc., Waltham, MA, USA) were diluted 1 :  $10^6$  in PBS (Phosphate Buffered Saline, Sigma-Aldrich).  $20\ \mu\text{l}$  of that dilution is applied to the coverslip for about 5 min, rinsed with Milli-Q water and dried with  $\text{N}_2$ . The coverslip is then mounted on the objective slide forming a flow channel. The channel is filled with PBS and sealed with epoxy glue (*Hysol*<sup>®</sup>, Loctite).

## 3.2.2 A functional form for $\bar{p}$

### Data acquisition

To measure the PSF a sample with immobilized single 20 nm fluorescent microspheres and with Au nanorods is used. The excitation wavelength is chosen to be 642 nm. The rods enable stage drift measurement and compensation using the stage lock introduced in sec. 3.1. In the first step an isolated microsphere is centered in the region detected by APD 1 (see setup in fig. (3.1)). The stage

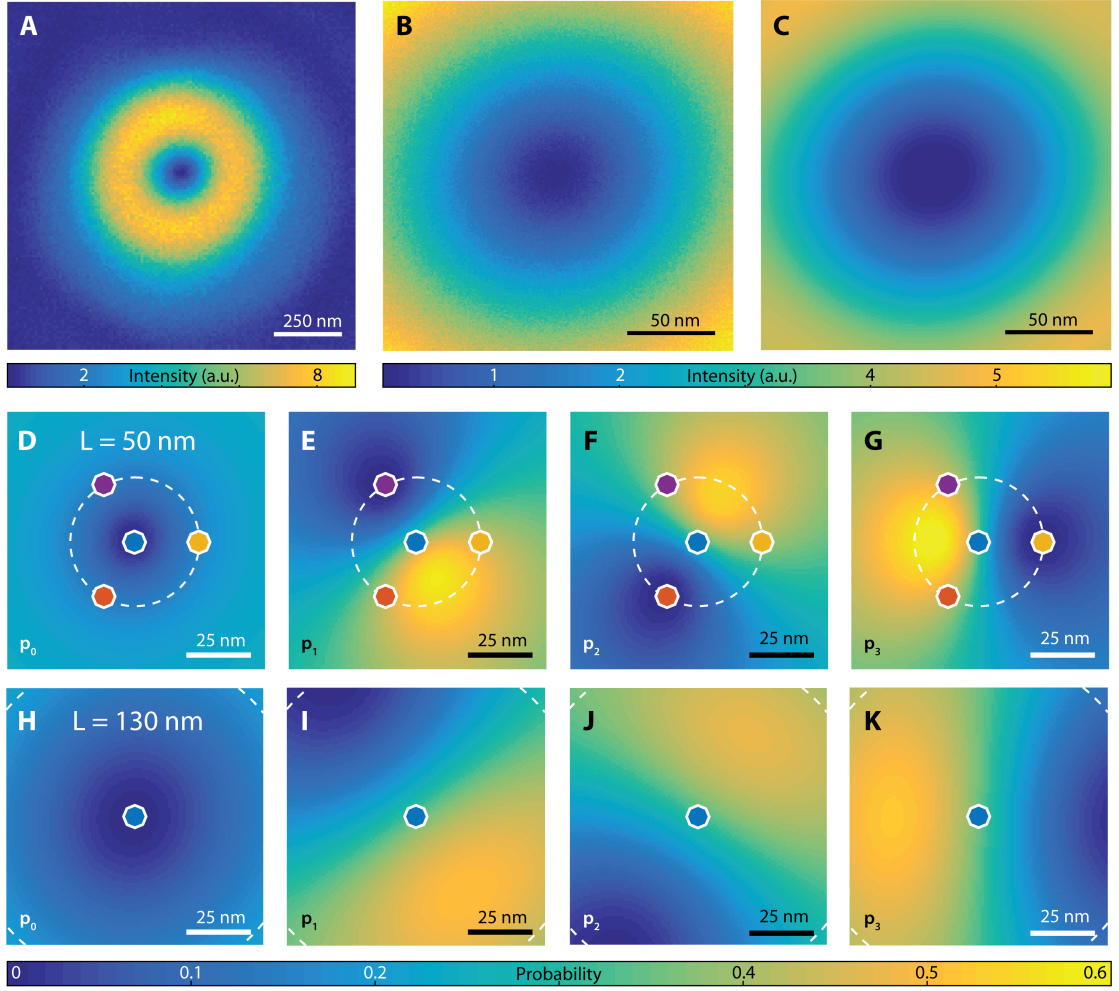


Figure 3.3: (A) Typical experimental doughnut shaped point spread function used for single emitter excitation in two dimensions. (B) Zoom to the central region of the PSF. Emitters in the field of view will only be excited by this inner region. The profile is obtained after averaging over multiple frames that have been drift corrected (see text). (C) Fit of the model excitation profile to (B). (D-G) Respective multinomial success probabilities  $p_i^{(0)}(\bar{r})$  (see eq. (2.7)) obtained from the model excitation profile (C) for a beam separation of  $L = 50$  nm and the EBP of eq. (2.37). (H-K) Multinomial success probabilities  $p_i^{(0)}(\bar{r})$  for a beam separation of  $L = 130$  nm as employed in the tracking application. Figure adapted from Balzarotti et al. (2016).

lock is then set to stabilize the stage position in three dimensions. The doughnut shaped excitation beam is subsequently scanned over the microsphere using the non-descanned electro-optical deflectors (EOD<sub>x</sub> and EOD<sub>y</sub>) and the emitted fluorescent photons are detected. The pixel size is typically set to 1 nm and the pixel dwell time chosen to be 40  $\mu$ s with an excitation power of 1  $\mu$ W in the back focal plane of the objective. A total of about 500 frames are acquired, resulting in a total of about 5000 detected photons per pixel in the doughnut maximum. The acquisition of multiple frames allows for a drift correction in post processing. Furthermore, long lived emitter dark states as well as photo-bleaching can be identified and the corresponding frames discarded.

### Drift correction and PSF fit

A functional expression is to be obtained from the measured PSF. To that end, a fit of an adequate model is conducted to the drift corrected frames. To be able to apply a drift correction in the first place, the center of the PSF needs to be estimated from each frame. The PSF is doughnut shaped, such that it is describable by a 2D parabolic profile in the vicinity of its origin. That functional form is fit to each frame, and the position of the minimum used as an identifier for the PSF origin. The resulting positions are low pass filtered using a moving average filter of typically 10 frames to obtain more precise origin estimates. To align these, each frame is shifted accordingly in units of integer pixel. This makes sense in order to avoid the interpolation of Poissonian counts and is the main reason for the chosen small pixel size of 1 nm.

In the next step, the obtained drift corrected frames are averaged, resulting in one image that can be fitted using an adequate model. Note that in all applications of MINFLUX in this thesis, the emitter is either placed in close proximity to the center of the EBP or held in it by a feedback loop as in the case of the tracking application. Thus, the fit needs to describe the central region of the PSF region only. Typically, that region is chosen to be  $200 \times 200$  nm for beam patterns with  $L \leq 100$  nm and  $300 \times 300$  nm for bigger  $L$ . The doughnut shaped PSF can be approximated by a second order 2D polynomial function in that region. In order to account for deviations from a purely parabolic profile a 2D polynomial of order 4 is used

$$I_{PSF}(\vec{r}) = \sum_{k=0}^4 \sum_{l=0}^k a_{kl} (x - x_0)^k (y - y_0)^{k-l} \quad (3.1)$$



where the fit parameters  $x_0$  and  $y_0$  denote the PSF origin, and  $a_{kl}$  the polynomial coefficients. A typical experimental PSF is visualized in fig. 3.3 (A-B) and the resulting model function fit in (C).

### Multinomial success probability $\bar{p}$

The resulting functional form for the excitation PSF can be used to obtain a functional form for  $\bar{p}^{(0)}$ , the success probability without background contributions. The EBP employed here consists of four shifted doughnut shaped excitation PSF (see eq. (2.37) and fig. 2.2 (A) for a visualization). The respective exposures can be written as

$$I_i(\bar{r}) = I_{PSF}^*(\bar{r} - \bar{r}_{b,i}) \quad (3.2)$$

where  $I_{PSF}^*$  is the offset corrected version of the PSF model function  $I_{PSF}$  obtained from the fit in eq. (3.1), and  $\bar{r}_{b,i}$  is the beam displacement with norm  $|\bar{r}_{b,i}| = L/2$  for the peripheral beams. The parameter vector  $\bar{p}^{(0)}$  can now readily be obtained using eq. (2.7). A visualization of the four components of this vector is shown in fig. 3.3 (D-G) for a value of  $L = 50$  nm and in (H-K) for  $L = 130$  nm.

Note that the MLE and the numLMSE use the success probability  $\bar{p}$  as defined in eq. (2.10) for position estimation. The latter takes the background contributions into account and can be obtained from  $\bar{p}^{(0)}$  and the value of the SBR. The SBR is defined in eq. (2.9) and can be measured empirically. To that end, the average background counts  $\langle \lambda_b \rangle = 1/Q \sum_{j=1}^Q \sum_{i=0}^3 n_{ij}$  are calculated from the count trace of  $Q$  multiplex cycles obtained once the emitter is photo-bleached. This assures a very good background estimation, given that  $Q$  is typically very large (on the order of  $10^4$ ). For each localization with photon collection  $\bar{n}$  and a total of  $\sum_{i=0}^3 n_i = N$  photons, the SBR is given by:

$$\text{SBR} = \frac{N}{\langle \lambda_b \rangle} - 1 \quad (3.3)$$

Note that this is an SBR value estimation given by its ML estimate. In this definition the SBR loses its explicit position dependence (compare to eq. (2.9)). Given that the retrieval of the explicit functional form of the  $\text{SBR}(\bar{r}_m)$  would require the unintended estimation of the molecular brightness, the definition of eq. (3.3) is a good compromise. It does alter the functional form of the success probability  $p_i(\bar{r}_m)$  for  $\bar{r} \neq \bar{r}_m$ . But at the molecule position  $\bar{r}_m$  the  $p_i(\bar{r}_m)$  value uses the MLE of the SBR at that specific position. In the vicinity of  $\bar{r}_m$ , the

SBR definition of eq. (3.3) is an excellent approximation of the real SBR given by eq. (2.9). Note that this approach does not require the knowledge of the true molecule position for the SBR estimation.

### 3.3 Experimental validation of MINFLUX

In this section the theoretical results obtained for the MINFLUX localization precision are investigated experimentally. To that end, a single isolated ATTO 647N molecule in a *Reducing and Oxidizing System* (ROXS) buffer is repeatedly localized at different positions relative to the excitation beam pattern (EBP) origin. This enables obtaining the spatial dependence of the localization bias as well as of the localization precision that can readily be compared to the theoretical predictions.

The sample preparation protocol is presented in sec. 3.3.1. This is followed by a description of the measurement procedure and its analysis in sec. 3.3.2.

#### 3.3.1 Immobilized single ATTO 647N molecules

In order to obtain immobilized isolated single fluorescent emitters, DNA oligonucleotides labeled with ATTO 647N (ATTO Technologie, Inc., Amherst, New York 14068, USA) were used. Two 31 nucleotide long single stranded DNA are annealed, where one of them is labeled with a single ATTO 647N molecule at base position 4 and the second one is labeled with biotin. The biotin will be used for immobilization on the coverslip by binding it to streptavidin. Single stranded DNA oligonucleotides were purchased from IBA GmbH (Göttingen, Germany). The sequences with directionality from the 5'-end to the 3'-end are:

- ATA A(ATTO647N)TT TCA TTG CCA TAT ACT ACA GGA ATA A
- TTA TTC CTG TAT ATG GCA ATG AAA TTA T(Biotin)

The parentheses depict the positions where either the ATTO 647N or the biotin molecule is attached.

A nucleotide measures 0.33 nm (Mandelkern et al., 1981) such that the distance between the emitter and the biotin is about 1.3 nm. Both strands are mixed at equal concentrations and diluted to 100 nM concentration into a solution containing 10 mM TRIS (tris(hydroxymethyl) aminomethane), 10 mM *NaCl* (sodium chloride), and 1 mM EDTA (ethylenediaminetetraacetic acid). This solution is heated to about 95° C and gradually cooled down to room temperature in about 45 min to induce the annealing of the two single stranded DNA.

To prepare the sample, cleaned objective slides and cleaned coverslips with Au nanorods are used to generate a flow channel as explained in sec. 3.2.1. The flow channel is filled with  $5\ \mu\text{l}$  of 2 mg/ml biotinylated BSA (Albumin, biotin labeled bovine, A8549 – 10MG, Sigma-Aldrich) solution dissolved in PBS. The PBS in the flow channel is replaced by  $15\ \mu\text{l}$  of 0.5 mg/ml streptavidin (Streptavidin, recombinant, 11721666001, Sigma-Aldrich) solution dissolved in PBS. After 15 min the channel is rinsed with about  $400\ \mu\text{l}$  of PBS. Subsequently,  $15\ \mu\text{l}$  of 50 pM annealed DNA solution dissolved in PBS is added. After 15 min the channel is rinsed with about  $200\ \mu\text{l}$  of PBS followed by rinsing with  $200\ \mu\text{l}$  of ROXS buffer which stays in the channel. The fluorophore is embedded into a ROXS buffer in order to reduce bleaching and triplet state blinking of ATTO 647N. The latter is prepared according to (Vogelsang et al., 2008). The sample is then sealed with epoxy glue. Note that it must be ensured that no bubbles form in the rinsing processes as these deteriorate the sample.

### 3.3.2 Localization performance in the field of view

#### Data acquisition

In the first measurement the spatial dependence of the localization performance is to be evaluated for a beam separation of  $L = 100\ \text{nm}$ . An isolated single ATTO 647N molecule is placed in the center of the EBP by manual stage repositioning. The stage is then stabilized by activating the stage lock. Subsequently, the EBP itself is scanned in a rectangular grid of  $35 \times 35$  pixel with a pixel spacing of 3 nm. This is repeated multiple times, resulting in an ensemble of  $35 \times 35$  pixel frames. At each pixel a photon collection  $\bar{n}$  is detected from the four multiplexed doughnut excitations. Thus, each pixel in a frame consists of a photon collection vector  $\bar{n} = [n_0, \dots, n_3]$  which add up to a total of  $N$  photons. Scanning of the EBP center as well as the multiplexing of the EBP are controlled by the 125 kHz EOD controller. To ensure a stable beam position the multiplex cycle was set to 5 kHz with a gate delay of  $20\ \mu\text{s}$  (see fig. 3.2). The average power of the modulated excitation laser was set to about  $20\ \mu\text{W}$  in the back focal plane of the objective, resulting in a mean of  $\langle N \rangle \approx 1$  collected photon per multiplexing cycle in the center of the scanned grid with a signal-to-background ratio of  $\text{SBR} \approx 13$ , and  $\langle N \rangle \approx 2$  with  $\text{SBR} \approx 30$  at the outer borders. A total of about 6000 frames of  $35 \times 35$  pixel were acquired.

Furthermore, the localization performance at the origin of the EBP is to be evaluated for different  $L$  values. Again, an isolated single ATTO 647N molecule

$L$ (nm)	$\langle N \rangle$ [ $10^3$ ]	Number of frames	SBR
50	4	12500	4
75	7.5	12500	8.5
100	12	12500	14
125	18	12500	22
150	26	12500	30.5

Table 3.1: Obtained rounded mean photons per multiplex cycle  $\langle N \rangle$  in a pixel, the number of acquired  $9 \times 9$  grid frames as well as the rounded SBR for the evaluation of the localization performance at the origin of the EBP.

is placed in the center of the EBP by manual stage repositioning and the stage lock is activated. In this case the EBP is scanned in a  $9 \times 9$  pixel grid with grid spacing of 2 nm. After completion of one grid scan with a given  $L$  value, the latter is changed and the grid scan repeated. Once all  $L$  values have been used, the routine repeats starting from the first  $L$ . Thus, an ensemble of  $9 \times 9$  pixel frames is acquired for the respective  $L$  values. The average modulated excitation power as well as the multiplex cycle timings did not change to the above settings. The obtained mean photons per multiplex cycle in a pixel  $\langle N \rangle$ , the number of acquired  $9 \times 9$  grid frames as well as the SBR for the different  $L$  values are shown in table 3.1.

### Analysis

As in the previous section, the acquired frames were drift corrected in a first processing step. Each frame consisted of multiple pixel values that had four count channels  $[n_0, \dots, n_3]$ , respectively. The average total number of photons per pixel  $\langle N \rangle$  was low. Thus, a low pass filter was applied to each count channel in order to reduce noise contributions. For the  $31 \times 31$  grid, a sliding average filter with window length of 31 frames was employed. For the  $9 \times 9$  grid, the window length was set to 61 frames. Note that each count value  $n_i$  in a given pixel can be attributed to a known excitation beam displacement  $\bar{r}_i$ . In order to estimate the center of the PSF in each frame, a 2D parabolic profile was fitted to the ensemble of photon collections  $\{n_i\}$  of all pixels with their respective displacement  $\{\bar{r}_i\}$ . The drift showed a magnitude of about  $\pm 2$  nm in both directions over a timescale of minutes. In the next step the individual non low pass filtered frames were shifted laterally such that the estimated centers are aligned at a given position  $\bar{r}_0$ . Just as in the drift correction of sec. 3.2, the shifting was done in integer units of pixels in order to avoid interpolation of Poissonian counts.

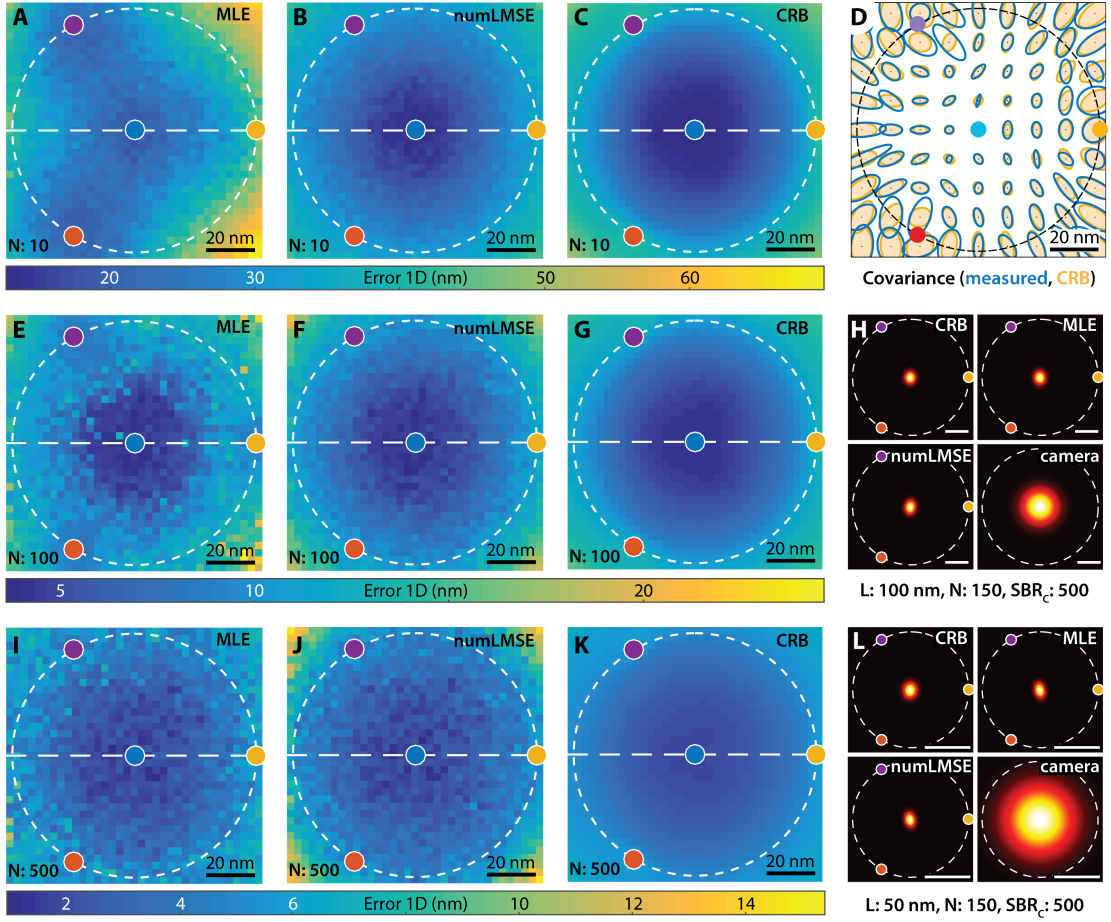


Figure 3.4: Static localization performance map for an isolated single ATTO 647N molecule with a beam separation of  $L = 100$  nm. (A, E, I) Measured MINFLUX localization error obtained from the MLE for three different number of total photons  $N = 10$ ,  $N = 100$  and  $N = 500$ . The localization error reached down to 2 nm for  $N = 500$  collected photons. (B, F, J) The numLMS estimator performance for the same number of photons. The numLMSE is better behaved than the MLE especially for low number of photons. (C, G, K) Visualization of the corresponding theoretical limit of the localization precision given by the CRB  $\tilde{\sigma}_{CRB}$ . (D) Measured and theoretical localization precision covariances represented as ellipses of contour level  $e^{-1/2}$  for the same conditions as in (I, K). (H, L) Comparison of the measured MINFLUX localization performance for two beam separations ( $L = 50$  nm in (H),  $L = 100$  nm in (L)) at the origin of the EBP to the ideal camera CRB with realistic SBR ( $SBR_c = 500$ ). The number of photons is  $N = 150$  in all cases. The covariances are shown as bivariate normal distributions. Scale bars 20 nm. Figure adapted from Balzarotti et al. (2016).

The drift corrected frames were subsequently employed to quantify the localization performance for a specific number of detected photons. To that end, the photon collection  $\bar{n}$  of a given pixel were binned to varying subsets of total photons  $N$ . Each collection was thereby used only once, in order to obtain a set of independent measurements. For a given  $N$  value, the subset of binned photon collections was localized with the MLE as well as the numLMS estimator. Both estimators require the knowledge of the multinomial success probability  $\bar{p}$  for the employed EBP, which is a function of the displaced excitation PSF and the SBR. As described in sec. 3.2, the PSF is modeled by a 2D polynomial function up to order 4 given by eq. (3.1) from which a functional form of the success probability  $\bar{p}$  can be obtained once the SBR is known. The SBR of each localization was calculated using eq. (3.3), where the average background counts  $\langle \lambda_b \rangle$  were obtained from the photon collections once the ATTO 647N emitter was photo-bleached. Thus, a localization estimation  $\hat{r}_m^{MLE}$  and  $\hat{r}_m^{numLMS}$  is obtained for every binned photon collection of a given pixel. The localization performance is characterized using the mean 1D error defined as

$$\sigma_{exp}^{(1D)} = \sqrt{\frac{1}{2M} \sum_{i=1}^M \|\bar{r}_0 - \hat{r}_m^{(i)}\|^2} \quad (3.4)$$

where  $\|\cdot\|$  is the Euclidean norm,  $\bar{r}_0 = [x_0, y_0]^T$  the true emitter position,  $M$  the number of binned photon collections and  $\hat{r}_m^{(i)} = [\hat{x}_m^{(i)}, \hat{y}_m^{(i)}]^T$  the estimated emitter position.

Furthermore, the Cramér-Rao bound  $\tilde{\sigma}_{CRB}$  was determined for the chosen total photon numbers  $N$ . The CRB depends solely on  $N$  as well as on the multinomial success probability  $\bar{p}$ , as derived in eq. (2.39). It was calculated numerically from the obtained functional form of  $\bar{p}$  for the respective pixel coordinates.

The resulting localization error  $\sigma_{exp}^{(1D)}$  for the  $L = 100$  nm measurement with a  $31 \times 31$  pixel grid is visualized in fig. 3.4 for three  $N$  values of  $N = 10$ ,  $N = 100$  and  $N = 500$  photons. Panel (C, D, K) shows the calculated CRB  $\tilde{\sigma}_{CRB}$  for the evaluated grid positions. Panel (A, E, I) show the performance using the MLE. A clear deviation to the CRB is especially visible for low photon numbers. A cross section marked as a straight dotted line in the respective panels is shown in fig. 3.5 (A-C). For  $N = 10$  the MLE deviates at all pixel positions from its CRB. For  $N = 100$  it is better behaved, especially when close to the origin. Nevertheless, starting from  $x = -20$  nm and  $x = 30$  nm, a deviation is visible. For high photon numbers the MLE converges nicely to its CRB for all evaluated positions as

demonstrated in the case of  $N = 500$  photons. Note that the localization error reaches down to 2 nm for  $N = 500$  detected photons using the beam separation of  $L = 100$  nm.

Additionally, the CRB on the localization precision of an ideal camera derived in sec. 2.3 is shown. For realistic signal-to-background ratios (dashed lines), the idealized camera performance is worse than that provided by MINFLUX, especially in the region surrounding the beam pattern origin. The ultimate limit for the ideal camera (infinite  $\text{SBR}_c$ ) is shown by the solid black line. For a total of  $N = 500$  photons, panel (D) in fig. 3.4 visualizes the localization uncertainty covariances for the obtained localization estimates of a grid point subset. The theoretical limit  $\Sigma_{CRB}$  was numerically calculated from eq. (2.39) and is visualized as yellow ellipses. A very good agreement is observable in most of the evaluated grid positions. The numLMS estimator shown in panel (B, F, J) is already well behaved at  $N = 10$  photons. A deviation is to be observed only at about  $x = \pm 40$  nm. Note that the localization performance is lower than the CRB here. This can be explained by the numLMSE being biased at these outer positions for low photon numbers. Therefore, the numLMS estimator already performs close to optimality for low photon numbers in nearly the complete field of view.

Figure 3.5 (D) visualizes the MLE localization error at the origin for  $L$  values ranging from  $L = 50$  nm to  $L = 150$  nm as a function of the total number of photons  $N$ . Convergence to the CRB is visible for photon numbers  $N \gtrsim (50 - 100)$  depending on the  $L$  value. Lower  $L$  values converge at a higher total number of photons. The numLMS estimator performance is shown in fig. 3.5 (E). For most beam separations  $L$ , the measured MINFLUX localization precision reaches the theoretical limit under the measurement conditions. A noticeable deviation is visible only for the localizations with  $L = 50$  nm and photon numbers below  $N \approx 20$ . Note also that the SBR gets considerably smaller for lower  $L$  values. In general, the measurements confirm the theoretical derivations very well. Especially the linear  $L$  dependence of the localization error as well as the inverse square-root dependence on  $N$ . Clearly, decreasing the beam separation  $L$  improves the localization precision more effectively than increasing the number of detected photons  $N$ .

The ideal camera CRB and the MLE performance for  $\text{SBR}_c = 50$  as well as  $\text{SBR}_c = 500$  is visualized in both fig. 3.5 (D) and (E). Furthermore, the CRB for infinite  $\text{SBR}_c$  is shown in a black solid line. Note that simulation and theory show that obtaining a localization precision of 5 nm requires about 600 photons with an ideal camera with realistic SBR ( $\text{SBR}_c = 500$ ), while MINFLUX with  $L = 50$  nm requires only 27 photons. The corresponding values are indicated with red circles

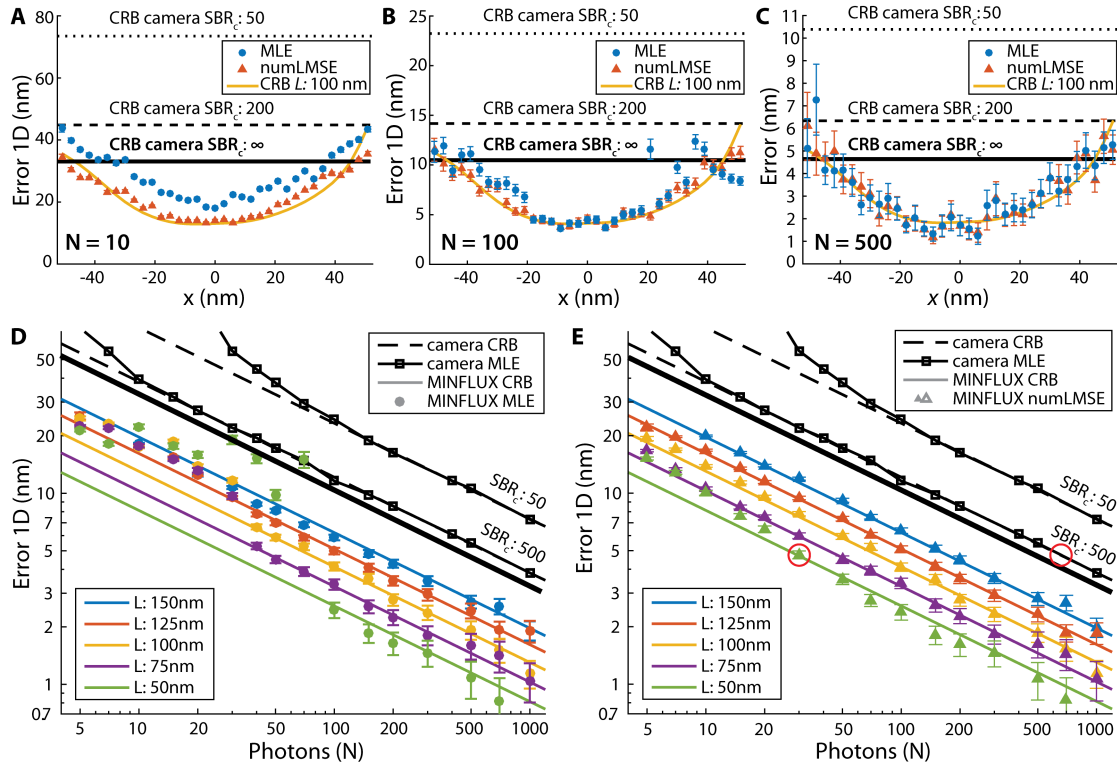


Figure 3.5: (A-C) Measured MINFLUX localization performance along the  $x$ -axis for three different numbers of collected photons  $N$ . The results obtained for the MLE (circles), the numLMSE (triangles) and the corresponding MINFLUX CRB  $\tilde{\sigma}_{CRB}$  (yellow lines) are shown. The CRB of the ideal camera performance for realistic signal-to-background ratios ( $SBR_c$ ) indicate a worse camera performance, especially in the proximity of EBP origin. The ultimate limit for the ideal camera ( $SBR_c = \infty$ ) is shown as this black line. The uncertainty of the error estimation (i.e. the  $\pm\sigma$  error bars) assumed the precision to follow a normal distribution. (D-E) Measured MINFLUX localization error at the origin of the EBP for different beam separations  $L$  as a function of the number of photons  $N$ . For  $N \lesssim 100$  the MLE breaks down, whereas the numLMSE performs well in the whole evaluated regime. The measured MINFLUX localization precision reaches the theoretical limit (CRB) under most of the measurement conditions. The ideal camera CRB is shown for three  $SBR_c$  values, where the thick black line indicates the limit on an infinite  $SBR_c$ . Measurement and theory show that obtaining a localization precision of 5 nm requires about 600 photons with an ideal camera ( $SBR_c = 500$ ), while MINFLUX with  $L = 50$  nm requires only 27 photons. The corresponding values are indicated with red circles. Figure adapted from Balzarotti et al. (2016).



in the panel (E). Thus, the MINFLUX photon-efficiency is increased by a factor of 22-fold in this regime. The comparison of the MINFLUX localization error at the origin for  $N = 150$  photons to the ideal camera with  $\text{SBR}_c = 500$  is further visualized in fig. 3.4 for  $L = 100$  nm in (H) and for  $L = 50$  nm in (L).

## 3.4 Localizing with high spatio-temporal resolution

MINFLUX theory and the obtained experimental results coincide very well, as the last section demonstrated. Especially close to the excitation beam pattern (EBP) center, the photon-efficiency can be improved compared to camera-based localization modalities. This bears the possibility to increase the spatio-temporal resolution of the localization process: given that less photons are needed to obtain a localization precision, a molecule emitting at a fixed count rate can be localized with equal precision at a higher temporal resolution. This will be evaluated in this section. Initially, an immobilized emitter is localized at high temporal resolution and the achievable localization precision is evaluated. Thereafter, MINFLUX will be applied to a DNA origami sample featuring dynamics on a fast time scale.

### 3.4.1 Sample preparation and measurement protocol

#### Sample preparation

Illustrations of the used samples are visualized in fig. 3.6 (A). The panel (A1) shows a fluorescent emitter attached to a 30 nucleotide (nt) single stranded DNA (ssDNA). It is complementarily paired to another ssDNA with a 33 nt base pairing on a rectangular DNA origami. By design the fluorescent emitter ATTO 647N is 4 nt or approximately 1.3 nm away from the DNA origami. The DNA origami is a modification of the Rothemund rectangular (Rothemund, 2006) with 5 biotinylated staple sequences for fixation on the coverslip via streptavidin-biotin linkage, and a double stranded DNA strand sticking out of the DNA origami plane with an ATTO 647N emitter.

Panel (A2) shows a cartoon of an 1D diffuser on a Rothemund rectangular DNA origami. Two DNA strands are attached to the DNA origami base and base paired with one long bridging strand. An ATTO 647N emitter is attached to the top of the bridge with a maximal distance of 10 nm from the DNA origami base. Ideally, the emitter can only move on a half circle above the DNA origami as a confined

1D diffuser. The sequence for the scaffold, the staples and of all further strands needed, are reproduced in the appendix C. The respective origami strands are annealed into a DNA origami in folding buffer consisting of  $1 \times$  TAE (40 mM Tris, 20 mM Acetate and 1 mM EDTA, Sigma-Aldrich) with 12.5 mM  $MgCl_2$  (Magnesium chloride hexahydrate, M2670, Sigma-Aldrich)  $ph = 8.0$ .

**DNA origami assembly** The staples need to be combined in the depicted order. Note that the sequences with number 11, 28, 123, 191 and 208 are biotinylated strands with biotin modification at the 5' end. The final pool contains 20 nM scaffold and 200 nM staples, including the unmodified, modified helping and biotinylated staples. Staple 76 is substituted by a 63 nucleotides ssDNA (76 single molecule helper) to obtain the **ssDNA solution**. Staple 22 and 76 are changed to Nes22 (1DD 22) and Nes76 (1DD 76) helper ssDNA in the origami annealing pool to obtain the **1DD bridge solution**.

**Thermal annealing and purification** The premixed DNA strand pool (either the ssDNA or the 1DD bridge solution) is heated to  $85^\circ C$  for 3 min using a thermocycler (TPersonal, Biometra GmbH, D-37079 Göttingen), cooled to  $42^\circ C$  at  $0.5^\circ C/min$  and then rapidly cooled to  $4^\circ C$ . In a next step the DNA origami are purified. The obtained solution is mixed 1 : 1 with a PEG buffer consisting of 15 % PEG (Poly(ethylene glycol), BioUltra, molecular weight 8000, Sigma-Aldrich), 500 mM  $NaCl$  (Sodium chloride,  $\geq 99\%$ , Sigma-Aldrich) and 12.5 mM  $MgCl_2$  (Magnesium Chloride hexahydrate, M2670, Sigma-Aldrich). The final solution is centrifuged at 20000 rcf for 30 min. The supernatant is discarded and the precipitate are resuspended in folding buffer by vortexing. The purification procedure was performed for 3 times. This procedure results in either ssDNA origami or 1DD origami.

**Immobilizing the origami** Cleaned coverslips coated with nanorods and cleaned objective slides are used to generate flow channels (see sec. 3.2.1). In analogue to sec. 3.3.1 immobilization employs biotin-streptavidin binding. The flow channel is filled with  $20 \mu l$  of 2 mg/ml biotinylated BSA solution dissolved in PBS for 5-10 min. After washing with PBS the channel is incubated with  $40 \mu l$  of 0.5 mg/ml streptavidin solution dissolved in PBS for 5 min. After another washing with folding buffer  $30 \mu l$  of DNA origami ( $\sim 100$  pM of either ssDNA origami or 1DD origami) are added and thus immobilized on the coverslip. Then,  $30 \mu l$

( $\sim 200$  pM) of the single molecule strand (SM strand) or alternatively of the bridge (1DD bridge) is added. After a brief checking of the density of the DNA origami (should be around  $< 0.1/\mu\text{m}^2$ ) ROXS buffer (see sec. 3.3.1) is added before the sample is sealed with epoxy glue (Loctite EA 3430, Henkel) for final imaging.

### Data acquisition

Here, the four-doughnut EBP of sec. 2.1.2 was used for excitation with 642 nm light. In the first step a faint widefield image of the sample was recorded with the CCD camera. Objects of interest were selected manually. Estimations of the corresponding coordinates were obtained by fitting a 2D Gaussian profile to the measured intensity distributions. Subsequently, the EBP was sent to the retrieved coordinate commanding the tip/tilt mirror. To improve the overlap between the object and the EBP center, a proportional integral controller feedback routine was used. For this routine the beam separation was  $L = 100$  nm. The EBP was multiplexed by commanding the 5 MHz EOD controller. Note that the 125 kHz controller was disconnected for these measurements. This enabled a faster beam repositioning and permitted setting the gate delay to  $3 \mu\text{s}$ . The multiplex cycle rate was  $\gamma_c = 10$  kHz and the detection and excitation gate were  $18.8 \mu\text{s}$ . The excitation power was about 10 % of the power used for the subsequent emitter localization (see below). Live position estimation was calculated using the mLMS estimator  $\hat{r}_{mLMS}^{(1)}$  (see eq. (4.1)) with parameters  $k_i = 1.2$  and  $\beta_1 = 3$ . The proportional and integral parameters of the controller were  $p_k = 0$  and  $p_i = 0.0087$ . EBP repositioning was done exclusively by the tip/tilt mirror. After 500 ms, the feedback routine was turned off.

For the now stationary EBP center, the count traces of the four respective exposures were recorded. The system parameters were the same as for the feedback routine except for a beam separation of  $L = 50$  nm and higher excitation powers. The static emitters were excited using 5.6 mW and 2.8 mW, the power for the 1D diffuser was 4.3 mW. Photons were detected with APD 1 granting a 400 nm field of view. In addition to the photon collection in every multiplex cycle, the individual photon arrival times were measured using a TCSPC module (PicoHarp 300, PicoQuant, 12489 Berlin, Germany).

In order to use the MLE or the numLMSE for localization estimations in post processing, the spatial dependence of the success probability  $\bar{p}(\bar{r})$  needs to be known. It was measured using the protocol introduced in sec. 3.2.

### 3.4.2 Experimental results

#### Blinking kinetics

In the first step the characteristic emitter OFF time  $\tau_{bl}$  was estimated. To that end, the temporal auto-correlation function of the photon arrival time  $G(\tau)$  was calculated for 19 traces and fitted to the following model, respectively (Widengren et al., 1995)

$$G(\tau) = G(0) \left[ 1 + \frac{F}{1-F} e^{-\frac{\tau}{\tau_{bl}}} \right] + G(\infty) \quad (3.5)$$

with  $F$  being the fraction of the emitter in the fluorescent OFF state and  $\tau_{bl}$  the emitter OFF time. Evaluation yielded  $\tau_{bl} = (5.7 \pm 1.4) \mu\text{s}$ , which is smaller but still close the detection and excitation gate of  $18.8 \mu\text{s}$ . If the emitter is in the OFF state during one of the multiplex cycle exposures, the resulting count quartet is not indicative of the true emitter position anymore. To reduce these effects, the collected photons of the respective doughnut exposures can be binned. In the subsequent analysis, four multiplex cycles were binned. This resulted in effective photon collection times of about  $75 \mu\text{s}$  per doughnut exposure, which is considerably longer than the emitter OFF time. The resulting time resolution of the binned photon collection, and therefore of the localizations, is  $\delta t = 400 \mu\text{s}$ .

#### Position estimation

Binning yielded about 70 to 140 average total photons per localization. For these values the MLE does not converge to its CRB yet (see fig. 2.8). Therefore, localization estimates were obtained using the numLMS estimator  $\hat{r}_{numLMS}^{(k=2)}(\hat{p})$  of eq. (2.72). The success probability parameter estimates  $\hat{p}$  were obtained from the binned photons  $\bar{n} = [n_0, \dots, n_3]$  using eq. (2.51). The SBR was estimated for every binned photon collection  $\bar{n}$  following eq. (3.3). Prior to further data analysis the obtained localizations were drift corrected. To that end, a 0.5 s moving average of the  $x$  and  $y$  trajectory were subtracted from the numLMS localizations with  $400 \mu\text{s}$  time resolution.

#### Static emitter localization

The results of two measurements with ATTO 647N molecules immobilized at about 1.3 nm distance from the origami base are subsequently discussed. The cartoon of the measured probe is shown in fig. 3.6 (A1). The first emitter yielded 25000 localizations with a mean position at  $x \approx 1.2 \text{ nm}$  and  $y \approx 0.2 \text{ nm}$  relative to EBP origin. This indicates that the employed feedback routine granted indeed a precise

overlap of the emitter with the EBP. The chosen excitation power of 2.8 mW yielded an average of  $\langle N \rangle = 74$  total photons per localization. The distribution of  $N$  is visualized in fig. 3.6 (D). The average signal-to-background ratio was 6.7.

A histogram of the obtained emitter localizations is shown in fig. 3.6 (B). Calculation of the error of the localizations using eq. (3.4) resulted in a localization precision of  $\sigma_{exp}^{(1D)} \approx 3.3$  nm at 400  $\mu$ s time resolution. The error of  $\sigma_{exp}^{(1D)}$  estimation assumed the precision to follow a normal distribution. The second emitter yielded 2396 localizations with a mean position at  $x \approx 1.4$  nm and  $y \approx 0.48$  nm relative to EBP origin. The average total photons per localization were  $\langle N \rangle = 138$  at 5.6 mW excitation power with an average signal-to-background ratio of 6.9. Note that both total photon distributions shown in fig. 3.6 (D) follow Poissonian statistics. The Poissonian distribution corresponding to the mean of the distributions is overlaid (black lines). For this emitter a localization precision of  $\sigma_{exp}^{(1D)} \approx 2.5$  nm was reached at 400  $\mu$ s time resolution. The corresponding localization histogram is visualized in fig. 3.6 (E).

Note that the achieved localization precisions are worse than their CRB predicted. For  $L = 50$  nm and the parameters of the second evaluated emitter, a precision of  $\sigma_{CRB} = 1.76$  nm is expected for the corresponding photon distribution with  $\langle N \rangle = 138$  shown in fig. 3.6 (D). The measured localization precision is reduced by a factor of about 1.4. This may be in part due to real emitter movement. The emitter is attached to a single stranded DNA at about 1.3 nm distance from the origami base. Thus, emitter movements on the order of  $\pm 1.3$  nm are possible. Movement on the order of or below the measuring time resolution can significantly broaden the apparent localization precision. A crude estimation of the broadening was obtained by assuming the emitter to be located at different positions distributed according to a Gaussian distribution with parameter  $fwhm = 2 \cdot 1.3$  nm at different localization instances. The resulting apparent localization precision is obtained by convolving the position distribution with the normally distributed error distribution with  $\sigma_{CRB} = 1.76$  nm. This increases the precision from  $\sigma_{CRB} = 1.76$  nm to  $\sigma_{CRB} = 2.07$  nm, which is closer to the real measurement. Note that this is just an approximation to clarify the effect of emitter dynamics in the localization precision.

In addition to emitter movement, system instabilities can increase the measured precision. These could arise from vibration of the sample or of optical components impelling excitation beam fluctuations. Unwanted tip/tilt mirror movement or voltage fluctuations at the EODs also need consideration. Indeed, a frequency analysis of the retrieved  $x$  and  $y$  positions showed prominent contributions at 10 Hz,

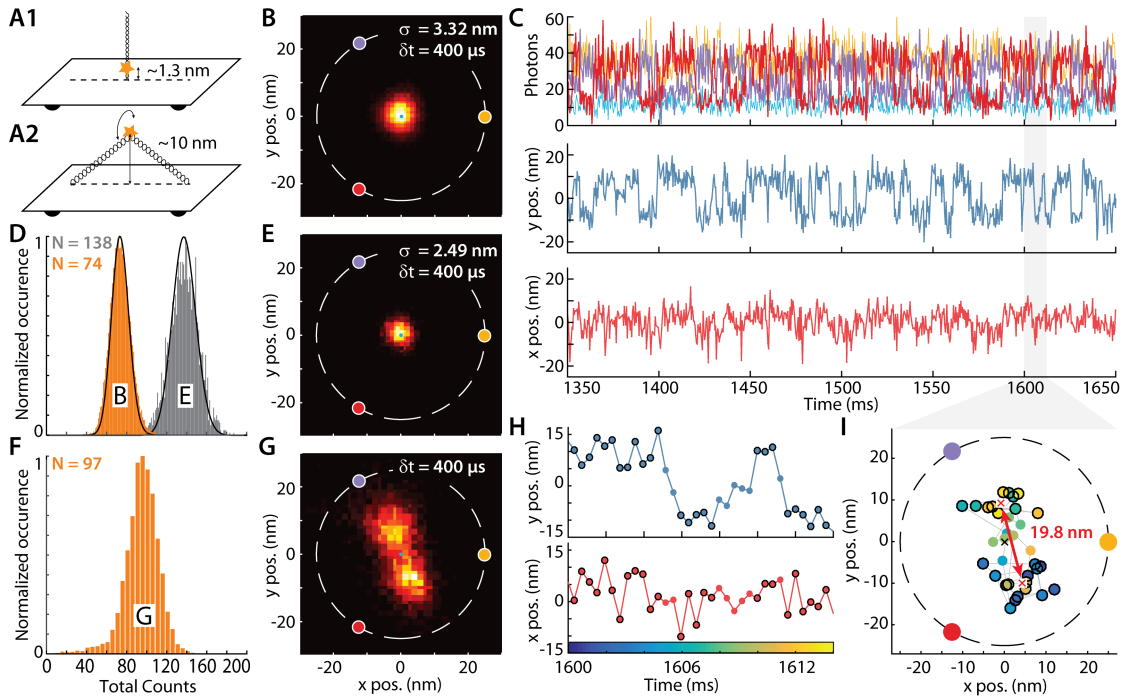


Figure 3.6: **(A)** Cartoon of the measured samples. **(A1)** Shows an ATTO 647N emitter attached to a single stranded DNA at 1.3 nm distance to the origami base. **(A2)** An ATTO 647N emitter is attached to a bridge consisting of two single stranded DNA. The distance of the emitter to the origami base is 10 nm for a vertical bridge position. The sample was designed to allow the emitter a movement in ideally one direction only. **(B)** Histogram of 25000 localizations of sample A1 with  $1 \times 1$  nm binning. For a time resolution of  $\delta t = 400$   $\mu$ s a localization precision of  $\sigma_{exp}^{(1D)} = 3.32$  nm was reached with an average of  $\langle N \rangle = 74$  photons. The locations of the excitation profile zeros are marked as colored dots. **(C)** Details of sample (A2) measurements. *Upper panel*: Photon counts obtained by binning 4 multiplex cycles. The color coding indicates the exposure and coincides with the color of the zero positions in panel (G). *Lower panels*: Retrieved  $x$  and  $y$  positions after numLMS position estimation. Two predominant positions at about  $\pm 10$  nm are especially visible in  $y$  direction. **(D, F)** Histogram of the photons used per localization. The distribution means are indicated in the legend. The corresponding localization histograms are indicated by capital letters. **(E)** Same as (B) but with an average of  $\langle N \rangle = 138$  photons resulting in a localization precision of  $\sigma_{exp}^{(1D)} = 2.49$  nm at  $\delta t = 400$   $\mu$ s. A total of 2396 localizations were used. **(G)** Histogram of 6118 localizations of sample A2 with  $\delta t = 400$   $\mu$ s time resolution. The predominant motion is along one direction as expected from the sample design. **(H)** 14 ms excerpt of the trace shown in (C) containing 35 localizations. The transitions between the predominant  $y$  positions are clearly resolved with the given spatio-temporal resolution. **(I)** Scatter plot of the excerpt shown in (H). The color coding of the dots indicates the time and coincides with the colorbar in (H). The distance of data points surrounded by black circles (also marked in (H)) is calculated to  $(19.7 \pm 0.2)$  nm and agrees with the sample design.

83 Hz and 135 Hz as visualized in fig. B.2, which could very well arise from system instabilities. These frequencies are not filtered out by the 0.5 s moving average drift correction. Therefore, they increase the apparent localization precision. Note that these frequencies would be averaged out in the measurements of the previous sec. 3.3 if they were present, where much larger photon integration times were employed.

Further improvement of the localization precision at high temporal resolution could be achieved by a live beam position measurement. Retrieved beam positions could be used in post processing to correct the numLMS localizations. To render this correction beneficial, the beam position estimation would need to be measured with high spatio-temporal resolution. Given that the excitation laser has vast amounts of photons, high spatio-temporal resolutions should be achievable.

### One-dimensional diffuser

In addition to static emitters, a sample allowing for ideally one-dimensional emitter movement on a half circle was evaluated. Figure 3.6 (C) visualizes a 300 ms excerpt of a resulting measurement. The red and purple count trace, belonging to peripheral doughnut excitations, show a pronounced anti-correlation. They result in a predominant movement along the  $y$ -direction as is evident from the numLMS position estimations in the lower panel as well as in the localization histogram in panel (G). Furthermore, the emitter seems to reside preferentially around two distinct positions at  $\bar{r} = [8.8, 4] \text{ nm}$  and  $\bar{r} = [-10.3, 0.8] \text{ nm}$ . They are marked as red crosses in panel (I) and result in an emitter displacement of around 20 nm as expected from the sample design. The normalized occurrence of the total counts per localization with an average of  $\langle N \rangle = 97$  is visualized in panel (F). Note that, as a result of the emitter movement, the distribution in (F) does not follow Poissonian statistics. For  $\langle N \rangle = 97$  the expected localization precision can be obtained from the reported results of the static emitters with  $\sigma_{exp}^{(1D)} = 3.3 \text{ nm}$  and  $\sigma_{exp}^{(1D)} = 2.5 \text{ nm}$ . Assuming the inverse  $\sqrt{N}$  dependence, a precision of  $\sigma_{exp}^{(1D)} \approx 2.9 \text{ nm}$  is expected in the proximity of the origin. Evaluation of the precision at the origin, perpendicular to the predominant movement direction, results in  $\sigma_{exp}^{(1D)} = (4.7 \pm 0.8) \text{ nm}$ . This indicates that the sample allows for movement perpendicular to its axis. Nevertheless, panel (H) and (I) show that MINFLUX is able to clearly resolve the sample dynamics of 20 nm maximal displacement with 400  $\mu\text{s}$  time resolution.

### 3.5 Summary and discussion

In order to employ the MINFLUX maximum likelihood estimator (MLE) and the numLMS estimator, a precise knowledge of the multinomial success probability  $\bar{p}$  is required. Section 3.2 illustrated how a functional form for  $\bar{p}$  can be obtained from the doughnut shaped experimental excitation PSF measured with the setup introduced in sec. 3.1.

In sec. 3.3 the localization performance of MINFLUX was investigated by repeatedly localizing a single ATTO 647N molecule on a pixel grid in the field of view. By using varying subsets of  $N$  photons the influence of the photon number on the localization error could be evaluated for the MLE as well as for the numLMSE. Throughout the field of view, the measured localization error obtained with MINFLUX agreed very well with its CRB, indicating that photon information has been used optimally. Theory and simulation showed that obtaining a localization precision of 5 nm requires about 600 photon counts with an ideal camera with realistic SBR ( $SBR_c = 500$ ), while MINFLUX measurements with  $L = 50$  nm reached that precision with only 27 photons. Thus, MINFLUX could increase the photon-efficiency by a factor of 22-fold compared to an ideal camera.

Subsequently, the MINFLUX performance at high spatio-temporal resolution was evaluated. Dynamics of a custom designed origami sample with 20 nm maximal emitter displacement could be resolved clearly using MINFLUX at 400  $\mu$ s time resolution. Furthermore, an immobilized single ATTO 647N emitter was localized at an identical time resolution with  $\sigma_{exp}^{(1D)} = 2.49$  nm localization error employing an average of  $\langle N \rangle = 138$  photons. Compared to its theoretical limit the measured localization error was worse by a factor of about 1.4. This was likely caused by emitter movement as well as system instabilities, implying that further improvements are possible.

For  $N = 138$  photons an ideal camera with a realistic signal-to-background ratio of  $SBR_c = 500$  would yield a localization precision of  $\sigma_{cam} = 10.3$  nm. This implies that equal localization precision requires a 17-fold increase in the number of photons per localization. Note that the CRB-based camera results represent idealized performances, that do not take read out noise or achievable realistic camera frame rates into consideration. In opposition to that, MINFLUX data was obtained under experimental conditions.



It was found experimentally that the fluorescence of ATTO 647N saturated at a detection count rate of about 1 MHz. The average MINFLUX count rate was around 350 kHz. In consequence, rates of 5.9 MHz would be required for an ideal camera to achieve equal spatio-temporal resolution, making it impossible to achieve the reported results in a camera-based approach if ATTO 647N is used.



# Chapter 4

## Single emitter tracking using MINFLUX

The results of chapter 3 validated the MINFLUX concept experimentally. Furthermore, it demonstrated that improved spatio-temporal resolutions are attainable in the proximity of the excitation beam pattern (EBP) center compared to camera based methods. In this chapter the MINFLUX concept is applied to track a diffusing single emitter. The emitter is kept in the photon-efficient central region of the field of view by repeatedly repositioning the EBP. Any method that localizes a finite photon-budget probe will suffer a tradeoff between the number of localizations and its spatial resolution. By following the emitter with the photon-efficient EBP center, the spatio-temporal resolution is to be increased not only locally, but for the entire emitter track. The results are again compared to state-of-the-art camera tracking methods.

In the next section the challenges associated with using the MINFLUX concept to track a diffusing single emitter are discussed. Suitable parameter settings for the beam separation  $L$ , the multiplex cycle rate as well as parameter values for the live position mLMS estimator are obtained through simulations. The simulation results are used to evaluate the precision with which emitter diffusivities as well as MINFLUX localization precisions can be retrieved. Furthermore, the parameter values obtained through simulation are evaluated experimentally. Known ground truth emitter movement is tracked with the experimental setup and compared to the retrieved trajectories. Finally, MINFLUX is applied to track ribosomal small subunit proteins S2 fused to the switchable fluorescent protein mEos2 in living *Escherichia coli* cells.

## 4.1 Assessment of the tracking performance using simulations

### 4.1.1 Challenges imposed by the method

Localizations of the single isolated emitter are to be carried out using the four-doughnut EBP introduced in sec. 2.1.2 and visualized in fig. 3.2. To track the emitter, the EBP is repeatedly repositioned to the estimated emitter location. In that situation the four-doughnut measurement needs to be carried out rapidly enough such that the emitter does not diffuse away too far from the photon-efficient EBP center. Amongst other things, that requires a live position estimation that is fast. To that end, the mLMS estimator introduced in sec. 2.2.2 is used. It is implemented as a live position estimator in the FPGA board (see sec. 3.1) and enables localization calculation times on the order of one microsecond:

$$\hat{r}_{mLMS}^{(1)}(\hat{p}) = -k_i(1 + \beta_1 \hat{p}_0) \sum_{i=1}^3 \hat{p}_i \cdot \bar{r}_{b,i} \quad (4.1)$$

It was designed to work in the central region of the EBP (see sec. 2.2.2 and fig. 2.6). The explicit values of the parameters  $k_i$  and  $\beta_1$  are optimized through simulation as discussed in the next section.

It is evident from eq. (4.1) that the directionality of the localization of the mLMS estimator for a given  $k_i$  and  $\beta_1$  value is defined by the values of  $\hat{p}_1$ ,  $\hat{p}_2$  and  $\hat{p}_3$ . A drawback of the chosen four-doughnut EBP is that very similar success probability  $\bar{p}$  values appear for emitter positions inside and outside of a region with radius of about  $r_{max} = 0.6 \cdot fwhm$ . This is the peak radius of the central intensity profile (see sec. 2.1.2). Figure 4.1 (A, B, D) shows a contour plot for success probabilities  $\bar{p}$  values corresponding to an emitter at  $\bar{r}_{m,1} = [-160, 80]^T$  nm. It is evident that, in addition to  $\bar{r}_{m,1}$  a second location in the opposite direction of the EBP origin has very similar success probabilities (both positions are marked with a white error in (A)). In consequence, one of the two locations will result in a position estimation  $\hat{r}_{mLMS}^{(1)}$  with wrong directionality. Panel (E) shows the direction and scaled magnitude of the mLMS estimator with  $k_i = 1.2$  and  $\beta_1 = 3$  in the form of vectors for a grid of locations. The color coded direction of the position estimation is shown in the background. Note that all positions with  $|\bar{r}| \gtrsim r_{max}$  show the wrong directionality.

The molecule is to be kept in the center of the EBP. Therefore, the  $k_i$  and  $\beta_1$  values were chosen to yield the correct direction for the positions with  $|\bar{r}| < r_{max}$ .

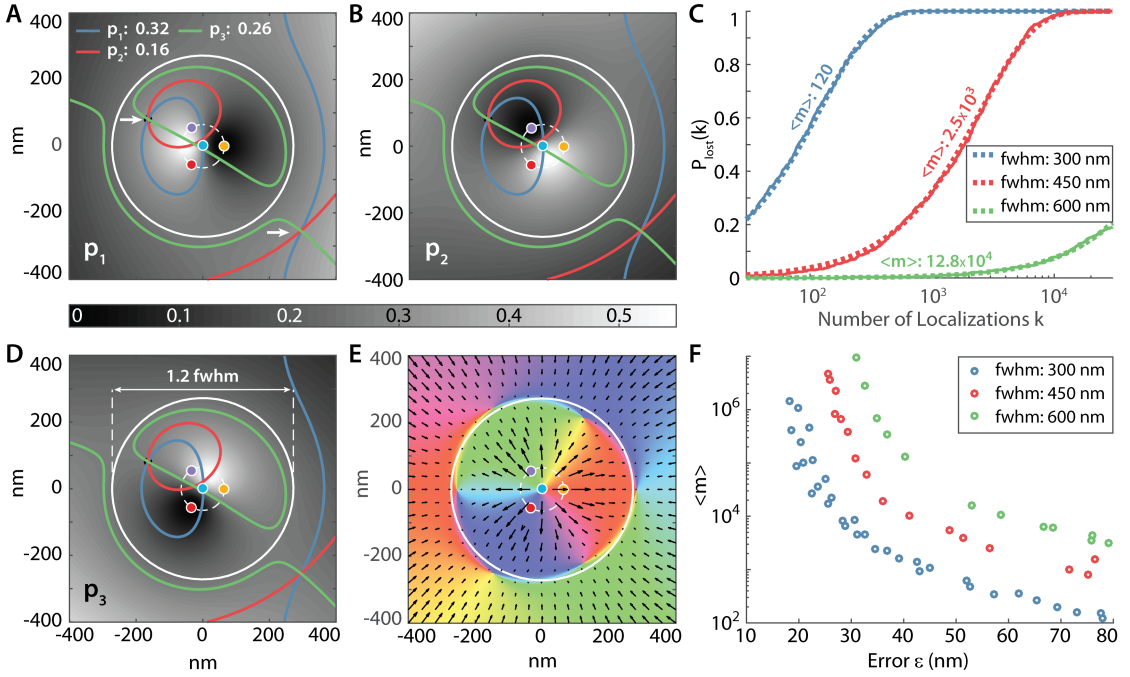


Figure 4.1: (A, B, D) Success probability  $p_1$ ,  $p_2$  and  $p_3$  for four doughnuts with  $fwhm = 450$  nm and a beam separation of  $L = 130$  nm. Overlaid is a contour plot for  $\bar{p}$  values corresponding to an emitter at  $\bar{r}_{m,1} = [-160, 80]^T$  nm. Arrows indicate the positions  $\bar{r}_{m,1}$  and  $\bar{r}_{m,2} = [300, -265]^T$  nm which show similar success probabilities. These two positions lie in opposite directions of the EBP origin,  $\bar{r}_{m,1}$  inside and  $\bar{r}_{m,2}$  outside of a region with a radius of about  $0.6 \cdot fwhm$ . Given that the  $\bar{p}$  values are very similar for both positions, the mLMS estimator defined in eq. (4.1) will show similar magnitude and direction. Thus, the localization of an emitter at one of the two positions points in the wrong direction. (E) Arrows indicate the direction and scaled magnitude of the mLMS estimator with  $k_i = 1.2$  and  $\beta_1 = 0.3$  for a grid of emitter positions. Angles are color coded. Note that all positions outside of the region with a radius of about  $0.6 \cdot fwhm$  show a wrong direction. Thus, the EBP will move away from an emitter if it is outside of that region in a live tracking implementation, and eventually lead to the emitter being lost. (C) Visualization of  $P_{lost}(k)$ , the probability of losing the emitter in localization  $k$  for  $fwhm = (300, 450, 600)$  nm. Parameter are as stated in (F) except for  $\Gamma_c = 10$  kHz and  $D = 1 \mu\text{m}^2/\text{s}$ . (F) Mean number of localizations  $\langle m \rangle$  before losing the emitter. Simulation parameters were set to  $L = 130$  nm,  $\gamma_c = 8$  kHz,  $k_i = 1.2$ ,  $\beta_1 = 3$ ,  $\Gamma_c = 2.5 - 80$  kHz,  $D = 0 - 1 \mu\text{m}^2/\text{s}$  and  $fwhm = (300, 450, 600)$  nm. The emitter was assumed not to blink. For larger  $fwhm$  values, the mean number of localizations before losing the probe is higher for a given tracking error  $\epsilon$ .

In consequence, the probability of losing a diffusing emitter is high once it is outside of  $r_{max}$ , as the localization points away and not toward the emitter. This suggests that the probability of losing an emitter will have a dependence on the  $fwhm$  value (given that  $r_{max} \approx 0.6 \cdot fwhm$ ).

Simulation results confirmed this supposition. The simulation routine described in sec. 4.1.2 was used with parameters as described in fig. 4.1 (D). For each parameter combination, 600 tracks with  $30 \cdot 10^3$  multiplex cycles were simulated and, the number of localizations  $m$  before the emitter is lost, extracted. The ratio of the number of emitters lost over the total number of emitter yields  $P_{lost}(k)$ , the probability to have lost the emitter in localization  $k$ . Figure 4.1 (C) visualizes  $P_{lost}(k)$  for three different  $fwhm$  values. It turned out that the process of losing the emitter can be reasonably well described by a Markov chain of order two, with state  $A = \text{“not lost”}$  and  $B = \text{“lost”}$ . Let the probability of staying in  $A$  be given by  $p_{aa}$  and the transition probability from  $A \rightarrow B$  given by  $1 - p_{aa}$ . The assumption is made that once in  $B$  this state cannot be left again. Therefore, the probability to have lost the molecule in or before the  $k^{th}$  localization is given by  $P_{lost}(k) = 1 - p_{aa}^k$ . This model fits the data reasonably well (see fig. 4.1 (C)). Using it, the mean number of localizations before losing the emitter can be estimated:

$$\langle m \rangle = \sum_{k=1}^{\infty} k \cdot p_{aa}^{k-1} (1 - p_{aa}) = \frac{1}{1 - p_{aa}} \quad (4.2)$$

Figure 4.1 (F) visualizes  $\langle m \rangle$  as a function of the tracking error  $\epsilon$  (defined in eq. (4.3)) for three different  $fwhm$  values. At equal error  $\epsilon$ , the track length is extended by increasing the  $fwhm$ .

In the experimental implementation in chapter 4.4, the  $fwhm$  was set to  $fwhm = 450 \text{ nm}$ . Note that large  $fwhm$  values require higher beam power to yield the same excitation intensity in the EBP center. Thus, an increase of the  $fwhm$  reduces the SBR and increases the light dose the sample receives.

In addition to the mLMS estimator working in a finite region only, the localization error grows with distance to the EBP center (see sec. 2.2.2). In order to reduce the tracking error  $\epsilon$ , and therefore the probability of losing the emitter, adequate tracking parameters need to be chosen. The multiplex cycle rate  $\gamma_c$ , for example, should be chosen high enough to ensure that the emitter does not diffuse out of the photon-efficient proximity of the EBP center during the multiplex cycle. The error  $\epsilon$  is not only dependent on  $\gamma_c$ , but also on the emitter diffusivity  $D$ , the

beam separation  $L$ , the total count rate  $\Gamma_{tot}$ , the mLMS parameters  $k_i$  and  $\beta_1$  as well as on the SBR.

Furthermore, potential emitter blinking, i.e. irregular fluorescence ON and OFF intermittencies, has to be taken into account. In sec. 4.4 single 30S ribosomal protein subunits fused to the photoconvertible fluorescent protein mEos2 were tracked in living *Escherichia coli* (*E. coli*). The fluorescent emitter mEos2 showed blinking on millisecond timescales. Initial blinking parameter estimates showed ON and OFF times around  $t_{on} = 2.5$  ms and  $t_{off} = 1$  ms. Once the emitter is in the OFF state, no position information can be obtained. These blinking events put further constraints on the tracking parameter choices.

Suitable parameter combinations were obtained from a simulation. The evaluated range of diffusivities was thereby adapted to results obtained in previous studies. It was shown that most of the 30S ribosomal protein are in a bound state with a low apparent diffusion coefficient of  $D \approx 0.06 \mu\text{m}^2/\text{s}$  (88 %) and only about 12 % in a free state with an apparent diffusion coefficient of  $D \approx 0.4 \mu\text{m}^2/\text{s}$ . The fastest measured  $D$  values are on the order of  $D \approx 1 \mu\text{m}^2/\text{s}$  (Sanamrad et al., 2014). The tracking parameters were therefore tuned to track this fastest expected  $D$  value with a reasonably low tracking error  $\epsilon$  as discussed in the next section.

### 4.1.2 Parameter optimization

In order to assess the influence of the tracking parameter on the tracking error, the following simulation routine was employed.

#### The simulation routine

**Trajectory generation** Two-dimensional trajectories were generated for free isotropic Brownian motion characterized by a diffusion constant  $D$ . Starting from a position  $\bar{r}_m = \bar{0}$  nm subsequent position increment realizations in  $x$  as well as in  $y$  were drawn from a normal distribution with variance  $\sigma_D^2 = 2Ddt$ . Thus, a diffusive movement was approximated by a random walk. The time sampling  $dt$  was chosen to be 12 times smaller than the time interval for one localization.

**Excitation beam pattern** The excitation geometry was set to the four-doughnut EBP introduced in sec. 2.1.2 with a beam separation parameter  $L$ . The doughnut excitation profile is given by eq. (2.33), with  $fwhm = 450$  nm if not stated otherwise. The total time interval for one multiplex cycle is  $\Delta t_c$ . Typically, the multiplex cycle rate  $\gamma_c = 1/\Delta t_c$  is reported. The trajectory time sampling  $dt$  is

chosen to be  $dt = \Delta t_c/12$  to allow for a 12-fold subsampling of the trajectory. This accounts for motion blurring during the multiplex cycle.

**Photon count realizations** Poissonian emitter photon count realizations were drawn in every sub-sampling interval. They resulted in an emitter photon collection of  $\bar{n}_m = [n_{m,0}, \dots, n_{m,3}]^T$  after one multiplex cycle with a total number of  $N_m = \sum_{i=0}^3 n_{m,i}$  photons. For simulation speed improvement, Poissonian noise contributions were drawn only once per multiplex cycle for each exposure. Note that the parameter  $\lambda_{noise}$  of the Poissonian noise distribution was assumed to be equal for all four beams. The value of  $\lambda_{noise}$  is defined through the signal-to-background ratio (SBR) at the center of the EBP. If a total of  $\langle N_m \rangle$  emitter photons is obtained at this position, the parameter  $\lambda_{noise}$  is given by  $\lambda_{noise} = \langle N_m \rangle / \text{SBR}$ . Thus, a photon collection consisting of emitter as well as noise contributions  $n_i = n_{m,i} + n_{noise,i}$  is obtained for every beam exposure after a multiplex cycle.

The amplitude of the excitation beam is set to obtain a total count rate  $\Gamma_c$  at the center of the EBP. This rate comprises emitter as well as noise contributions. Typical  $\Gamma_c$  values are chosen to be in the range between 10 kHz and 150 kHz. Note that the total count rate  $\Gamma_{tot}$  of a tracked emitter is larger than  $\Gamma_c$ . This is due to a radially growing intensity profile of the EBP in the vicinity of its origin.

**Emitter blinking** In order to incorporate potential emitter fluorescence ON and OFF intermittenencies in the simulation, blinking ON and OFF times were assumed to be exponentially distributed with parameters  $t_{on}$  and  $t_{off}$ . Transition probabilities between the two fluorescent states were evaluated on every trajectory time sampling  $dt$ .

**Position estimation** Emitter localizations during the track employed the live position estimator  $\hat{r}_{mLMS}^{(1)}$  of eq. (4.1) with parameter  $k_i$  and  $\beta_1$ . The success probability estimates  $\hat{p}$  can be obtained from the photon collection  $\bar{n} = [n_0, \dots, n_3]^T$  of a multiplex cycle using eq. (2.51). After each multiplex cycle, the EBP center  $\bar{r}_{EBP}$  is repositioned to the emitter position estimate  $\bar{r}_{EBP} + \hat{r}_{mLMS}^{(1)}(\hat{p})$ .



**Tracking error definition** The tracking error  $\epsilon$  for a track with  $S$  multiplex cycles is defined as the mean distance between the *average emitter position during the multiplexing cycle* and its respective position estimate:

$$\epsilon = \sqrt{\frac{1}{2S} \sum_{i=1}^S \|\langle \bar{r}_i \rangle - \hat{r}_i\|^2} \equiv \sqrt{\frac{1}{2S} \sum_{i=1}^S \|\bar{\zeta}_i\|^2}, \quad \text{with } \bar{r} \in \mathbb{R}^2 \quad (4.3)$$

where  $\|\cdot\|$  depicts the Euclidean norm,  $\bar{\zeta}_i = \langle \bar{r}_i \rangle - \hat{r}_i$  is the error vector,  $\hat{r}_i$  the estimated emitted position after the  $i^{\text{th}}$  multiplex cycle and  $\langle \bar{r}_i \rangle$  the average emitter position during the  $i^{\text{th}}$  multiplex cycle of duration  $\Delta t_c$ :

$$\langle \bar{r} \rangle = \frac{1}{\Delta t_c} \int_0^{\Delta t_c} \bar{r}(t) dt \quad (4.4)$$

In the simulation the integration is replaced by a sum over the trajectory updates in the corresponding multiplex cycle. For the mLMS live position estimator, the estimated emitter position is given by  $\hat{r}_i = \bar{r}_{EBP,i-1} + \hat{r}_{mLMS,i}^{(1)}$ , where  $\bar{r}_{EBP,i-1}$  is the EBP center position during the  $i^{\text{th}}$  multiplex cycle and  $\hat{r}_{mLMS,i}^{(1)}$  the position estimate relative to the EBP center.

### Simulation results

The simulation routine was used to find suitable parameter combinations to track a single emitter with a maximal apparent diffusion coefficient of  $D = 1 \mu\text{m}^2/\text{s}$ . Fluorescence ON and OFF intermittencies with blinking ON and OFF times of  $t_{on} = 2.5 \text{ ms}$  and  $t_{off} = 1 \text{ ms}$  were assumed. Initial measurements characterized the signal-to-background ratio to  $\text{SBR} \approx 3.5$  for the chosen *fwhm* of 450 nm. The parameter space that was evaluated comprised the mLMS estimator parameter  $k_i$  and  $\beta_1$ , the beam separation  $L$ , the multiplex cycle rate  $\gamma_c$  as well as the total count rate  $\Gamma_{tot}$ . Subsequently, the influence of these parameters on the tracking performance are discussed.

Figure 4.2 (A) visualizes the influence of the mLMS parameters  $k_i$  and  $\beta_1$  on the tracking error  $\epsilon$ . Used parameter settings are specified in the figure caption. It is evident that multiple  $k_i$  and  $\beta_1$  combinations result in low error values. This property also repeated for lower  $D$  values and different  $\gamma_c$ ,  $L$  and  $\Gamma_c$  combinations. To reduce the dimensionality of the parameter space, the  $\beta_1$  value was set to  $\beta_1 = 3$  leaving only the scaling factor  $k_i$  as a free parameter of the mLMS estimator.

The influence of this  $k_i$  parameter on the tracking error is shown in fig. 4.2 (B) for different  $D$  values with and without emitter blinking. Note that in both cases

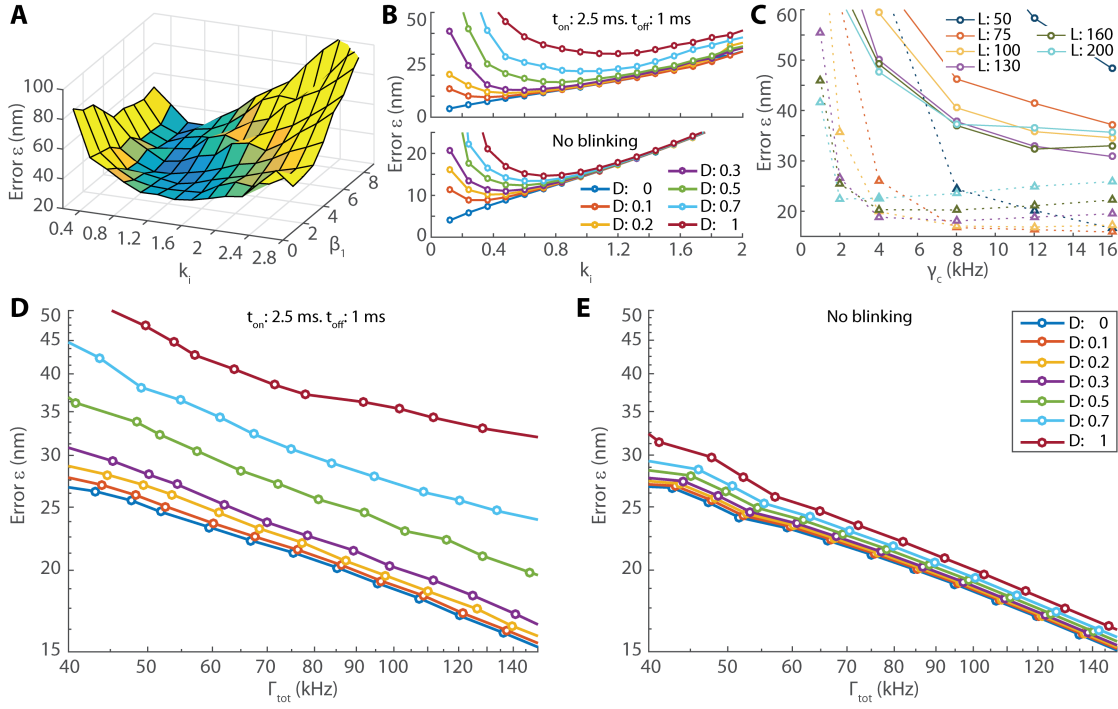


Figure 4.2: **(A)** Influence of the mLMS parameters  $k_i$  and  $\beta_1$  on the tracking error  $\epsilon$  for  $D = 1 \mu\text{m}^2/\text{s}$ ,  $\text{SBR} = 3.7$ ,  $t_{on} = 2.5 \text{ ms}$  and  $t_{off} = 1 \text{ ms}$ . For each  $k_i$  and  $\beta_1$  combination 200 tracks of  $30 \cdot 10^3$  localizations were simulated. The multiplex cycle rate was  $\gamma_c = 8 \text{ kHz}$ , the beam separation  $L = 130 \text{ nm}$  and the count rate  $\Gamma_c = 80 \text{ kHz}$ . **(B)** Influence of the mLMS scaling factor  $k_i$  on the tracking error  $\epsilon$  with  $\beta_1 = 3$  for different diffusivities  $D$ . The upper panel visualizes results with emitter blinking, the lower panel assumes the emitter to be in the ON state at all times. Further parameter settings are equal to (A). **(C)** Tracking error  $\epsilon$  as a function of the multiplex cycle rate  $\gamma_c$  for different beam separations  $L$  and a diffusion coefficient of  $D = 1 \mu\text{m}^2/\text{s}$ . The mLMS parameter  $\beta_1$  is set to  $\beta_1 = 3$ . The  $k_i$  value resulting in a minimal tracking error  $\epsilon$  for each  $\gamma_c$  and  $L$  combination was extracted from the simulation. The total count rate is  $\Gamma_{tot} = 75 \text{ kHz}$ . Round markers (and solid lines) represent emitter tracking results with blinking times of  $t_{on} = 2.5 \text{ ms}$  and  $t_{off} = 1 \text{ ms}$ . Triangular markers (and dotted lines) represent tracking with no blinking present. The color coding indicates the  $L$  values as depicted in the legend. **(D)** Tracking error  $\epsilon$  for  $L = 130 \text{ nm}$ ,  $\gamma_c = 8 \text{ kHz}$ ,  $\beta_1 = 3$  and  $k_i = 1.2$ . These are the parameters used in the experiment in chapter 4.4. Blinking ON and OFF times were  $t_{on} = 2.5 \text{ ms}$  and  $t_{off} = 1 \text{ ms}$ . SBR as in (A). **(E)** Tracking error  $\epsilon$  for the same parameters as in (D), except for no emitter blinking.

higher diffusion coefficient  $D$  values require larger  $k_i$  values for optimal tracking. This is understandable given that the  $k_i$  scaling factor is related to the integral parameter of an integral controller. Small  $k_i$  values in an integral controller cause a position set point to be reached after multiple controller updates only. This can make the tracking routine too slow to follow a fast diffusing emitter. At the same time, a small  $k_i$  reduces the magnitude of noise contributions. In consequence, there is an optimal value balancing out both contributions to minimize the tracking error.

For a simplified system with constant localization noise contribution  $\sigma_0$  on every EBP pattern position update, for example, the expected error is calculated analytically in the appendix A. The interplay between both error contributions is clearly visible from eq. (A.6). In the case of realistic MINFLUX tracking, the localization error is not constant in every update but depends on the position of the molecule and the number of collected photons. This renders the analytic deviation of the tracking error challenging and was not pursued further in this work.

For a diffusion coefficient of  $D = 1 \mu\text{m}^2/\text{s}$ , the  $k_i$  value minimizing the tracking error  $\epsilon$  can readily be extracted from the simulation. This was done for different beam separations  $L$  as well as for different multiplex cycle rates  $\gamma_c$ . The results are visualized in fig. 4.2 (C) in the case of blinking (solid lines) and without it (dotted lines). The results show that lower multiplex cycle rates  $\gamma_c$  require larger beam separations  $L$  to enable tracking with low error values. This can be understood as explained subsequently. For low  $\gamma_c$  values, the emitter has more time to diffuse away from the EBP center in-between localizations. Even though the localization precision at the EBP center is decreased for large  $L$  compared to smaller  $L$ , the field of view in which the live estimator has low bias is increased. The diameter of that region is approximately  $L/2$  (see fig. 2.6). This renders  $L = 200 \text{ nm}$  better suited than  $L = 75 \text{ nm}$  at multiplex cycle rates of  $\gamma_c = 2 \text{ kHz}$  as is evident from the figure.

For increased multiplex cycle rates starting from  $\gamma_c = 8 \text{ kHz}$ , smaller  $L$  values down to  $L = 75 \text{ nm}$  become suitable and result in better tracking performances.  $L = 75 \text{ nm}$ , for instance, enables a tracking error of  $\epsilon < 17 \text{ nm}$  at  $\Gamma_{tot} = 75 \text{ kHz}$ . This count rate corresponds to only 9 photons per localization.

Note that an increased multiplex cycle rate  $\gamma_c$  is not always positive, as can be seen from the error  $\epsilon$  increasing for  $\gamma_c > 2 \text{ kHz}$  in the case of  $L = 200 \text{ nm}$ . The reason is that for the evaluated count rate of  $\Gamma_{tot} = 75 \text{ kHz}$  a higher  $\gamma_c$  involves less photons per localization and therefore higher localization errors. Thus, a tradeoff

between the photons per localization used, the distance the emitter moves away from the EBP center and the spatial localization precision profile exists.

The tracking error increases significantly in the case of emitter blinking, as is evident from fig. 4.2 (C). In the fluorescent OFF state, the emitter is free to diffuse away from the proximity of the EBP center. Consequently, minimal errors  $\epsilon$  arise at higher  $L$  values. At 8 kHz for example,  $L = 75$  nm is not suitable anymore. In this case minimal errors are achieved for beam separations of  $L = (130 - 200)$  nm.

In this work a multiplex cycle rate of  $\gamma_c = 8$  kHz was chosen. This is related to the electro-optical deflectors requiring a gate delay of  $7.4 \mu\text{s}$  to reposition the doughnut beams in between the multiplex cycle (see fig. 3.2). Thus, the laser off time in a multiplex cycle needs to be on the order of  $30 \mu\text{s}$ . For a multiplex cycle rate of  $\gamma_c = 8$  kHz, this implies the laser being off in 25 % of the multiplex cycle. For  $\gamma_c = 16$  kHz the laser off time would be already 50 %. For equal count rate this implies higher laser powers and therefore also higher peak intensities in the living *E. coli* cells.

For the multiplex cycle rate of  $\gamma_c = 8$  kHz, a beam separation of  $L = 130$  nm was chosen as it resulted in similar tracking performances as larger  $L$  values up to 200 nm. The corresponding suitable mLMS parameters can readily be extracted from the simulation and are  $k_i = 1.2$  and  $\beta_1 = 3$ .

## 4.2 Diffusion estimation

Single molecule tracking is often used to extract quantitative parameters on the behavior of single molecules in their natural environments. An important motion regime is the free diffusive motion in an isotropic media that is characterized by a diffusion constant  $D$  (Michalet and Berglund, 2012). This section evaluates with which precision the emitter diffusivity can be retrieved from the simulated MINFLUX tracks.

Different algorithms can be found in the literature to estimate the apparent diffusion coefficient  $D$  as well as the average localization precision  $\sigma$  from single-particle tracks. A brief algorithm overview is presented and the choice of an optimized least-square fit (OLSF) diffusion estimation (Michalet and Berglund, 2012) for this work is motivated. It is found that the OLSF estimator needs some slight adaptation compared to its published version (Michalet and Berglund, 2012) to precisely retrieve the diffusivity of simulated MINFLUX trajectories. Doing so enables  $D$  estimation with a performance close to its information-based theoret-

ical limit. Furthermore, it could be shown that the OLSF estimator enables the correct estimation of the average MINFLUX tracking error  $\epsilon$  from the measured trajectories.

### 4.2.1 D estimation: algorithm overview

A maximum likelihood estimation (MLE) approach for the diffusion, based on the statistics of the observed molecule displacements  $\{\Delta_k = \bar{r}_{k+1} - \bar{r}_k\}$ , was developed (Berglund, 2010). In this approach, the calculation of the exact values of the likelihood function  $\mathcal{L}(D, \sigma \mid \bar{\Delta})$  for a diffusivity  $D$  and an average localization precision  $\sigma$  given the molecule displacement vector  $\bar{\Delta}$  can be very time consuming, especially for trajectories with a large number of localizations  $S$ . This is because, for every  $D$  and  $\sigma$  pair, a  $(S-1) \times (S-1)$  covariance matrix needs to be inverted. To overcome this drawback an approximation based on the discrete Fourier transform was employed, rendering the MLE computationally more efficient. In the case that molecular blinking is present, some time-lapse displacements are missing in the emitter trajectory. In that situation the MLE can still be used (Shuang et al., 2012). Unfortunately, non-equally spaced time-lapse displacements do not allow the use of the mentioned approximation. This renders the MLE time consuming, especially for long trajectories. In this work, blinking as well as long trajectories with an average of  $\langle S \rangle > 700$  are present (see sec. 4.4), such that the MLE was not employed.

Nevertheless, the knowledge of the likelihood function enables the computation of the Cramér-Rao bound (CRB) for the  $D$  and  $\sigma^2$  parameter estimation as derived in Berglund (2010) for non-blinking emitter trajectories. For  $S \gg 1$ , the theoretical limit on the relative standard deviation  $\sigma_D/D$  is given by

$$\frac{\sigma_D}{D} \geq \sqrt{\frac{2}{d(S-1)}} \cdot [1 + 2\sqrt{1 + 2X}]^{\frac{1}{2}} \quad (4.5)$$

where  $d$  is the dimensionality of the trajectory space. Here  $X = \sigma^2/D\Delta t - 2R$  is the *reduced square localization error* (Berglund, 2010; Michalet, 2010), where  $\Delta t$  is the time interval between trajectory points and  $R$  is the motion blur coefficient, a dimensionless variable characterizing the duration and type of the emitter exposure

$$R = \frac{1}{\Delta t} \int_0^{\Delta t} I_p(t) (1 - I_p(t)) dt \quad (4.6)$$

where  $I_p(t)$  is the illumination percentage occurring between the start of the exposure ( $t = 0$ ) until time  $t$ . For a uniform exposure during the whole time interval

$\Delta t$ ,  $R$  is  $R = 1/6$ ; for the multiplex cycle employed in MINFLUX tracking we obtain  $R \approx 1/6.2$  (see fig. 3.2, sec. 4.4.1 and sec. 4.3.1).

The CRB on the relative diffusion coefficient  $D$  estimation precision in eq. (4.5) gives valuable insights on how to conduct experiments to maximize the  $\sigma_D/D$  precision (Vestergaard, 2016). It was found that the maximization of the number of localizations  $S$  is more important than the actual localization precision  $\sigma$  in a given localization in order to obtain precise  $\sigma_D/D$  estimates.

Furthermore, a regression-free covariance-based estimator (CVE) that is computationally very fast was proposed (Vestergaard et al., 2014). It converges to the CRB of eq. (4.5) for small reduced square localization errors  $X \lesssim 1$ , and thus estimates  $D$  and  $\sigma$  values optimally in that regime. For  $X \gtrsim 1$ , however, the CVE departs considerably from the CRB. Given that this work employs time intervals of  $\Delta t = 125 \mu s$ , the reduced square localization error exhibits high values  $X \gg 1$  (for typical  $D$  and  $\sigma^2$  values, see fig. 4.6). Consequently, the CVE is not suitable for the parameter regime covered here.

Alternatively, an algorithm for an optimized least-square fit (OLSF) to the mean square displacement (MSD) was derived (Michalet and Berglund, 2012). In the case of free isotropic Brownian Motion in  $d$  dimensions, the MSD for a lag  $s$  is given by

$$\rho_s = 2d(\sigma^2 - 2RD\Delta t) + 2dDs\Delta t \quad (4.7)$$

The experimental MSD curve is fitted to this model, using time lags from  $s = 0$  to a given value  $s$ . There is an optimal number points  $s = s_{opt}$  to fit, in order to extract the diffusion coefficient estimate  $D$  with maximum precision. This is because the variance of the MSD gets larger with increasing lags  $s$ . Additionally, correlated values cause the MSD curve to deviate from linearity for large  $s$  values. At the same time the variance in the first MSD points is dominated by the localization precision  $\sigma$ . Thus, large  $\sigma$  values require longer lags  $s$  to obtain reliable diffusivity estimates for  $D$ . It was found that the value of  $s_{opt}$  for  $D$  estimation depends solely on the reduced square localization error  $X$  and on the number of localizations  $S$  in the track. If  $s_{opt}(X, S)$  is employed, the OLSF estimator performance approaches optimality for a wide parameter range. This, in addition to its computational simplicity, makes the OLSFE a potentially promising candidate for extracting diffusion coefficients from the measured trajectories.

### 4.2.2 Applicability and performance of the OLSFE

In the evaluated tracking application the emitter was blinking and large  $X$  values were present. Furthermore, the MINFLUX localization precision has a dependence on the relative position of the emitter to the EBP center. This leads to non-uniform localization precisions for different trajectory points (see sec. 2.1.2 and fig. 2.3). Therefore, the prerequisites that allow the utilization of the  $s_{opt}(X, S)$  relationship are not met (Michalet and Berglund, 2012). To evaluate whether the OLSFE is still applicable, simulated trajectories were evaluated. The simulation routine employed is described in sec. 4.1.2.

**Simulation settings** Two-dimensional trajectories with 1200 localizations were generated for free isotropic Brownian motion with diffusion constants in the range of  $D \in (0.01 - 1) \mu\text{m}^2/\text{s}$  and count rates of  $\Gamma_{tot} \in (20 - 200) \text{ kHz}$ . The signal-to-background ratio was set to  $\text{SBR} = 3.7$ . A total of 100 trajectories were generated for each parameter combination. Blinking On and OFF times were assumed to be exponentially distributed with parameters  $t_{on} = 2.2 \text{ ms}$  and  $t_{off} = 0.6 \text{ ms}$ . These parameter values are in agreement with the experiment (see sec. 4.4). The multiplex cycle rate was  $\gamma_c = 8 \text{ kHz}$  with a beam separation of  $L = 130 \text{ nm}$ . Emitter localizations employed the live position estimator  $\hat{r}_{mLMS}^{(1)}$  defined in eq. (4.1) with parameter  $k_i = 1.2$  and  $\beta_1 = 3$ . The chosen simulation parameters covered the range of the employed values in the single emitter tracking measurement.

**Obtaining the MSD** In the case of blinking an MSD curve can still be defined (Michalet and Berglund, 2012)

$$\langle \rho_s \rangle = \frac{1}{\sum_{i=1}^{S-s} q_i q_{i+s}} \sum_{i=1}^{S-s} (\bar{r}_{i+s} - \bar{r}_i)^2 q_i q_{i+s} \quad (4.8)$$

with

$$q_i = \begin{cases} 1 & \text{emitter ON at sample } i \\ 0 & \text{emitter OFF at sample } i \end{cases} \quad (4.9)$$

In order to identify blinking states (ON and OFF) from the simulated tracks, a simple two state hidden Markov model was employed as explained in sec. 4.4.3. The raw trajectory  $\hat{r}$  of the emitter was estimated with the live position estimator  $\hat{r}_{mLMS}^{(1)}$ . This simplified estimator is biased and works well in a region surrounding the beam pattern origin only (sec. 2.2.2). Simulations show that this causes the MSD curves to deviate from the expected linear relationship of eq. (4.7) as evident

from fig. 4.3 (A). To improve the localization estimates, the raw trajectories were corrected in post processing using the numLMS estimator. The MSD obtained from a raw trajectory employing the mLMS estimator, as well as the MSD obtained from the numLMS corrected trace are shown. The linear behavior of eq. (4.7) is retrieved after the correction. At the same time, the offset of the corrected trace is higher, which suggests that the localization error  $\sigma$  is increased after the numLMS correction (see eq. (4.7)). This is counter-intuitive at first glance. The reason is related to the finite working region of the mLMS. Outside of it, position estimations become considerably biased, especially radially, which reduces the spread of localizations and therefore the value of  $\epsilon$ .

**Optimal fit length** The MSD curve obtained from eq. (4.8) for the respective numLMS-corrected trajectories was fitted to eq. (4.7) for different logarithmically spaced lengths parameters  $s \in [2, 1200]$ . Subsequently, the  $s$  values minimizing  $\sigma_D/D$  were identified and found to follow the relationship:

$$s_{opt}(X) = 2 + 4.5 \cdot X^{0.62} \quad (4.10)$$

The identified  $s_{opt}$  values as well as the functional form of eq. (4.10) are visualized in fig. 4.3 (B). Given that the  $X$  value of a trajectory is not known *a priori*, the recursive algorithm proposed in (Michalet, 2010) is used:

**Recursive optimization algorithm** Start by setting the maximal lag of the MSD curve to  $s_0 = S/10$  and extract  $\hat{\sigma}_1$  and  $\hat{D}_1$  using a fit of eq. (4.7) to the MSD curve. These estimates allow the calculation of a reduced square localization error estimate  $\hat{X}_1$ . Using the latter, a new lag  $s_1$  can be obtained from eq. (4.10). Repeating this procedure results in a fast convergence to the optimal lag value  $s_{opt}$ . Non-convergence is an exceptional case and can be spotted by reoccurrences of  $s$ -values (i.e. optimization is trapped within the same two values).

This algorithm was applied to simulated trajectories with  $S = 100$ ,  $S = 1200$  and  $S = 5000$  localizations, respectively. In the case that the obtained lag  $s_i$  in an iteration was larger than  $S$ , the number of points used in the MSD fit was set to  $s_i = S$ . The simulation parameter choices (i.e.  $D, \Gamma, \dots$ ) were equal to the ones stated before in ‘‘Simulation Settings’’ of sec. 4.2.2. After initialization of the recursive algorithm (using  $s_0 = S/10$ ), a total of 10 iterations were conducted. Figure 4.3 (C) visualizes the median and the standard deviation of the



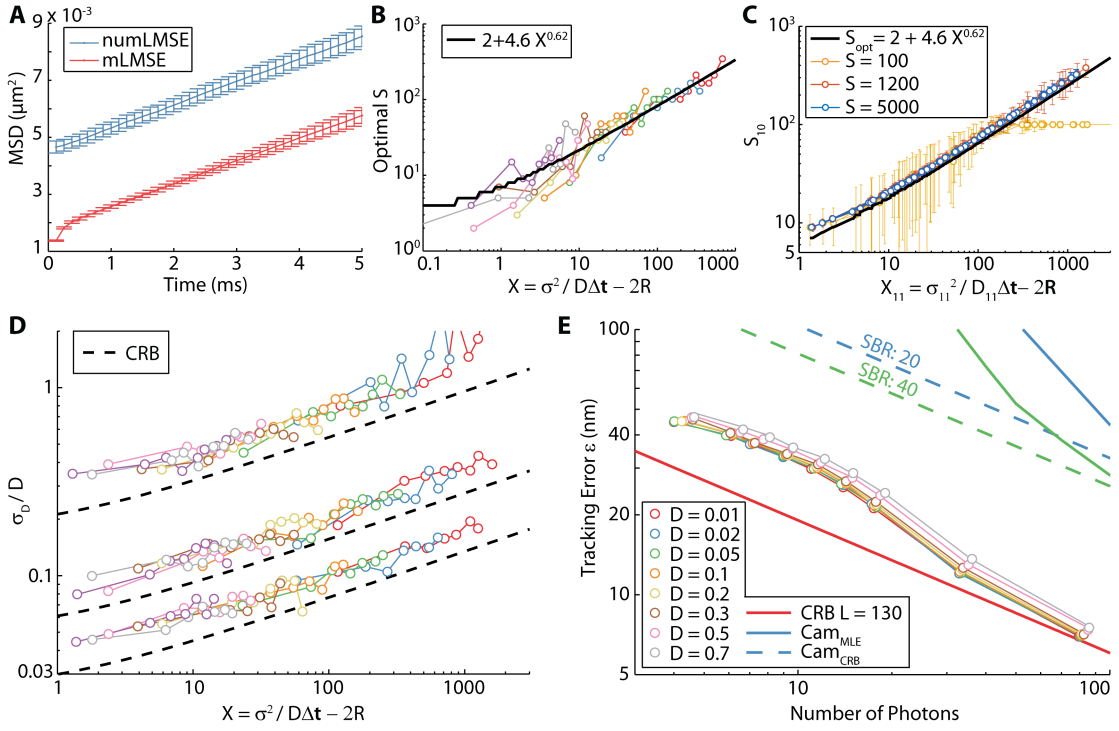


Figure 4.3: Estimation of the apparent diffusion coefficient and tracking error. Data in this figure is based on a tracking simulation using MINFLUX. The single emitter movement follows free isotropic Brownian motion in two dimensions. **(A)** Comparison of the mean of 100 MSD curves for trajectories obtained using the mLMS estimator (red) and the numLMS estimator (blue). The total width of the error bars represents twice the standard deviation. **(B)** Optimization of the number of MSD points  $s$  used in the fit to eq. (4.7). Optimization was conducted by minimizing the deviation of the estimated  $\hat{D}$  value to its ground truth  $D$  value. The optimal  $s$  values can be described by the relationship of eq. (4.10). **(C)** Convergence of  $s$  to  $s_{opt}$  using the recursive optimization algorithm (see 4.2.2) for different number of trace length  $S$ . Each data point represents the median of 100 trajectories. The total width of the error bars is twice the standard deviation. The  $s_{10}$  values were obtained after 10 iterations, and are plotted against the estimated reduced square localization error  $\hat{X}_{11}$ . The latter was obtained from the results of the 10<sup>th</sup> iteration. **(D)** Comparison of the relative standard deviation  $\sigma_D/D$  of the estimated  $D$  values to its CRB in eq. (4.5). Each data point is calculated from 100 trajectories. The results of 3 different trajectory length  $S$  are visualized. 10 iterations of the recursive optimization algorithm were conducted. **(E)** Comparison of the real tracking error  $\epsilon$  (thin colored lines) with the value extracted by the OLSF method (colored circles). The CRB (eq. (2.40)) for  $L = 130$  nm and  $fwhm = 450$  nm at the origin (EBP center) is shown as a thick red line. The CRB of camera localization for two  $SBR_c$  are shown as thick dotted lines. The MLE camera performance (for equal  $SBR_c$ ) is pictured as thick colored lines. Figure adapted from Balzarotti et al. (2016).

values  $s(\hat{X}_{10})$  for the three respective trace lengths. They are plotted against the estimation  $\hat{X}_{11}$  to visualize the convergence (i.e., all the points are close to the optimal curve of eq. (4.10)).

**Diffusion coefficients** The apparent diffusion coefficients were extracted using the final fit of the recursion routine. Subsequently, the variance  $\sigma_D^2$  was calculated from the 100 repetitions of each parameter combination. The resulting values of  $\sigma_D/D$  are visualized in fig. 4.3 (D). Though close to the CRB, the estimator is not optimal and could possibly be improved. It deviates from its theoretical limit given by eq. (4.5) by a factor of about 1.4. It should be noted that the CRB values correspond to tracks without emitter blinking and should only be taken as a guide. The derivation of the likelihood function (and CRB) for the parameters of a trajectory of a blinking emitter surpasses the scope of this work.

**Estimation of the localization precision** Equation (4.7) does not only permit obtaining the diffusion coefficient  $D$  from a track, but also the average localization precision  $\sigma$ . Note that it was shown that the optimal trajectory length  $s_{opt}$  for diffusion coefficient  $D$  estimation differs from the one for localization precision  $\sigma$  estimation (Michalet and Berglund, 2012). Nevertheless, the  $[S, N]$ -parameter region spanned in this work, which is visualized in fig. 4.6, is well suited for precise  $\sigma$  estimation. Figure 4.3 (E) shows that the estimated average localization precision  $\hat{\sigma}$ , obtained from eq. (4.7), coincides very well with the ground truth tracking error  $\epsilon$  (see eq. (4.3) and sec. 4.1.2). Furthermore, the convergence of the MINFLUX tracking error to its theoretical bound at the origin (EBP center) is evident from the plot in the limit of high number of photons per localization. This suggests that the mLMS live position estimator is able to keep the tracked emitter in close proximity to the EBP center in this regime. A further requirement for the convergence is that the numLMS post processing corrections has to perform close to its theoretical bound, a fact we know to be true from the discussion in sec. 2.2.2.

In conclusion, the OLSF estimator is applicable to extract the diffusion coefficient  $D$  as well as the tracking error  $\epsilon$  of the numLMS corrected tracks with (i) blinking, (ii) non-uniform localization precision and (iii) large values of the reduced square localization error  $X$  for the trajectory lengths that are present in this work.

### 4.3 Testing the tracking routine

Before tracking a diffusing molecule within an E.coli cell, MINFLUX tracking with the experimental setup introduced in sec. 3.1 was tested on known trajectories. For this purpose, a ground truth waveform was injected into the system and compared to the retrieved MINFLUX trajectory. The trajectory generation was achieved by displacing the excitation beam pattern (EBP) center relative to the fluorescent emitter in well-defined steps. In order to exploit trajectory speeds beyond the capabilities of the piezo stage, the beam scanning system itself was used to generate the trajectory. The trajectory generation as well as the tracking were performed on the same FPGA board but completely independent from each other. To this end, a generator added a trajectory specific offset to the EBP center before a multiplex cycle. Note that in this implementation no emitter movement was present during the multiplex cycle. Thus, no motion blurring effects took place. After photon readout of the four displaced doughnut shaped beams, the emitter position was estimated using the mLMS estimator introduced in eq. (4.1) yielding a correction of the EBP center position ideally compensating the introduced offset. Both the injected as well as the retrieved trajectory were saved for subsequent analysis.

#### 4.3.1 Sample preparation and parameter settings

To perform this experiment a 20 nm fluorescent microsphere was chosen as emitter. The sample preparation followed the analogue procedure introduced in sec. 3.2.1. The emitter was excited at 642 nm using laser 1 (see fig. 3.1). Photons were collected using APD 2. MINFLUX tracking parameters were set to a multiplex cycle rate of  $\gamma_c = 8$  kHz, with a gate delay of  $7.4 \mu\text{s}$ , an excitation and detection gate of  $23.2 \mu\text{s}$  and a localization window of  $2 \mu\text{s}$  (see fig. 3.2). The beam separation was  $L = 100$  nm. Excitation powers measured before the back focal plane of the objective were about  $15 \mu\text{W}$ . The emitter position was estimated using the mLMS estimator introduced in eq. (4.1) with parameters  $k_i = 1.2$  and  $\beta_1 = 3$ . The induced trajectory consisted of two sinusoidal movements along the  $x$  and  $y$  direction with equal peak-to-peak amplitude of 300 nm but different frequencies. These were set to 150 Hz in  $x$  and 100 Hz in  $y$  direction. This resulted in a well-known Lissajous curve.

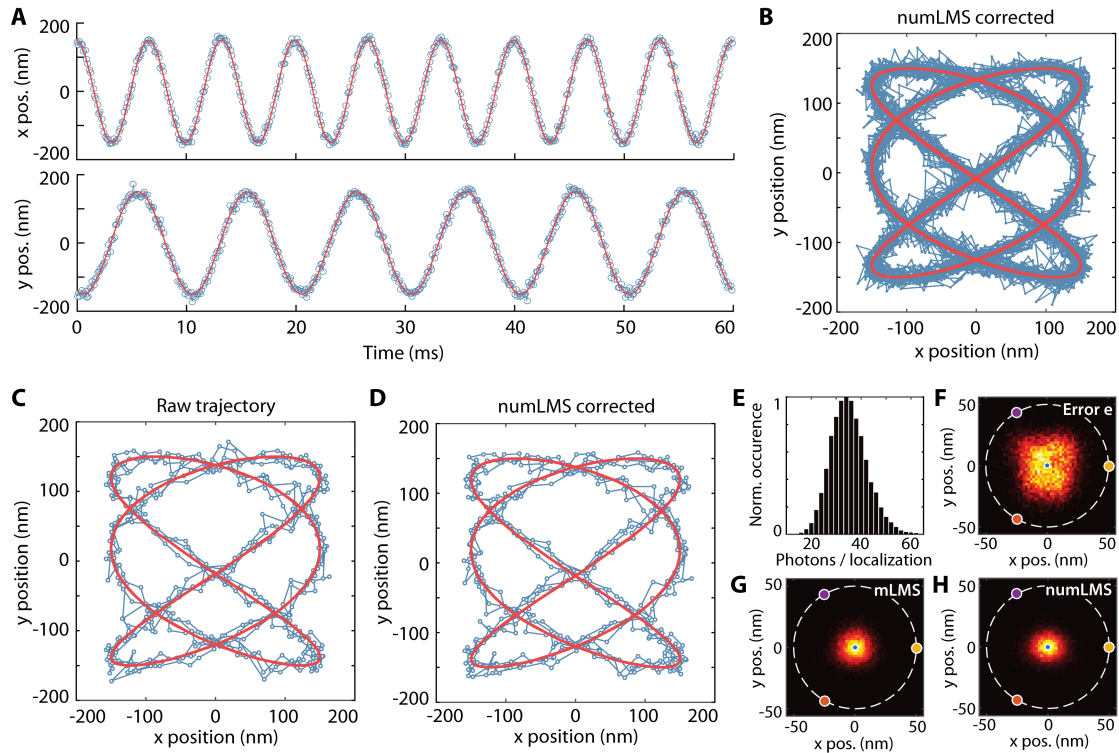


Figure 4.4: **(A)** Tracking of a predefined trajectory using a 20 nm fluorescent microsphere. Two sinusoidal trajectories along the  $x$  and  $y$  direction were injected to the system (solid red lines). The peak-to-peak amplitudes were 300 nm and the frequencies were 150 Hz and 100 Hz in  $x$  and  $y$ , respectively. MINFLUX tracking was performed with parameters as described in the text. The retrieved numLMS corrected trajectory is shown by the blue circles. **(B)**  $xy$ -plot of a 1 s excerpt of the injected and numLMS corrected trajectory with equal color coding as in (A). **(C)**  $xy$ -plot of the raw trajectories extracted from the experiment. Live position estimation was calculated using the mLMS estimator (see text for parameter settings). **(D)**  $xy$ -plot of the trajectories shown in (A). **(E)** Histogram of the detected photons per localization. The mean is 35.6 photons/localization. This corresponds to an average count rate of 285 kHz. **(F)** 2D histogram of the error vector  $\bar{e}$ , which characterizes the distance between the injected trajectory and the emitter before the EBP position is updated. The mean error is 12.7 nm. **(G)** 2D histogram of the error  $\bar{\zeta}$ , characterizing the distance between the injected and the retrieved mLMS trajectory. This corresponds to the distance between the injected trajectory and the emitter after the EBP position is updated. The mean error is 7.7 nm. **(H)** Post processing correction using the numLMS estimator further reduced the mean error to 7.5 nm. The errors are in good agreement with the Cramér-Rao bound in the experimental conditions. The latter was calculated to 7.3 nm.

### 4.3.2 Data processing and measurement results

The chosen MINFLUX parameter settings enabled the tracking of the fluorescent microsphere. Figure 4.4 (C) visualizes an overlay of the injected trajectory  $\bar{r}_i$  (solid red lines) and the retrieved trajectory  $\hat{r}_i = \bar{r}_{EBP,i-1} + \hat{r}_{mLMS,i}^{(1)}$  (round blue markers), where  $\bar{r}_{EBP,i-1}$  is the EBP center in the  $i^{th}$  multiplex cycle yielding the localization estimate  $\hat{r}_{mLMS,i}^{(1)}$  relative to the EBP center. Using the error definition of eq. (4.3), the tracking error  $\epsilon$  between the injected trajectory and the retrieved trajectory was estimated to  $\epsilon = 7.65$  nm. Here, the average emitter position  $\langle \bar{r}_i \rangle$  is given by  $\bar{r}_i$  as the emitter is not moving during the multiplex cycle. The distribution of the error vectors  $\bar{\zeta}_i^{mLMS} = \bar{r}_i - \hat{r}_i = \bar{r}_i - (\bar{r}_{EBP,i-1} + \hat{r}_{mLMS,i}^{(1)})$  is visualized in fig. 4.4 (G) as a 2D histogram. Note that the physical distance  $\bar{e}_i$  between the EBP center and the emitter during the multiplex cycle is not given by the error vector  $\bar{\zeta}_i$ , but by comparing the EBP center position to the emitter position, thus  $\bar{e}_i = \bar{r}_i - \bar{r}_{EBP,i-1}$ . The distribution of  $\bar{e}$  is shown in fig. 4.4 (F) as a 2D histogram. As expected it shows a larger spread than the error vector  $\bar{\zeta}^{mLMS}$ .

The average count rate of the fluorescent microsphere tracking was 285 kHz. This corresponds to a mean of 35.6 photons/localization. The histogram of the photons per localization used is visualized in fig. 4.4 (E). The knowledge of the photon collection  $\bar{n}$  in each multiplex cycle enabled post processing correction of the retrieved trajectory. Given the low total photon numbers per localization, the numLMS estimator introduced in sec. 2.2.2 was employed. In order to use it, the success probability  $\bar{p}$  needed to be known. To obtain  $\bar{p}$  the protocol introduced in sec. 3.2 was employed. The numLMS corrected trajectory is given by  $\hat{r}_i = \bar{r}_i - (\bar{r}_{EBP,i-1} + \hat{r}_{numLMS,i}^{(2)})$ . Using this post processing correction, the tracking error  $\epsilon$  was reduced to  $\epsilon = 7.48$  nm. The corresponding error vector  $\bar{\zeta}^{numLMS}$  distribution is visualized in 4.4 (H). Note the small deviation to the live tracking error  $\epsilon$  when using the mLMS estimator. This demonstrates that, for the error distribution  $\bar{e}$  shown in panel (F), the mLMS estimator is well suited.

The knowledge of the error distribution  $\bar{e}$  in combination with the photon collection  $\bar{n}$  and the success probability  $\bar{p}$  enabled calculation of the optimal performance given by the Cramér-Rao bound (CRB) that can be expected for the chosen EBP. To that end, the CRB  $\tilde{\sigma}_{CRB}$  was calculated numerically using eq. (2.39). The lower bound on the localization precision of the  $i^{th}$  localization in the track is given by calculating  $\tilde{\sigma}_{CRB,i}$  for an emitter position at  $\bar{e}_i$  using the corresponding photon collection  $\bar{n}_i$  with total number of photons  $N_i = \sum_{j=0}^3 n_j$ . Doing so yielded an average localization precision of  $\langle \tilde{\sigma}_{CRB} \rangle = 7.3$  nm. Thus, both the mLMS and

the numLMS performed close to optimality in these experimental conditions with a slightly improved numLMS performance.

Note that an ideal camera with a signal-to-background ratio of  $\text{SBR}_c = 500$  would require a factor of 7.5 times higher photons to achieve equal error values (see sec. 2.3). This corresponds to about 260 photons per localization. Even for the non-realistic ideal case of an infinite  $\text{SBR}_c$  about 190 photons per localization are needed for equal localization precision.

MINFLUX tracking by injecting the trajectory through the stage instead of the beam scanning system was also evaluated. As already mentioned, the stage enabled only slow emitter movement generation. Tracking results of a Lissajous trajectory with 1.5 Hz modulation in  $x$  direction and 1 Hz in  $y$  direction for different count rates and different  $L$  are shown in fig. B.1 in the appendix.

**Summary** The results presented in this section show that MINFLUX tracking using the experimental setup and employing the mLMS estimator works for various count rates and beam separations  $L$ . Trajectories injected through the stage as well as through the electro-optical scanners could be retrieved. Using  $L = 100$  nm, the retrieved mLMS tracking error for the chosen sinusoidal movement with 6.7 ms and 10 ms period and 300 nm peak-to-peak amplitude showed a photon-efficiency that was increased by 7.5 compared to the ideal camera performance. Furthermore, the tracking error of the numLMS corrected trajectory was close to optimality for the obtained mLMS track.

## 4.4 Tracking 30S ribosomal proteins in E. coli

After verification of the functionality of the tracking setup, MINFLUX was applied to track ribosomal small subunit proteins S2 fused to the switchable fluorescent protein mEos2 (McKinney et al., 2009) in living *Escherichia coli* (*E. coli*) cells. A number of challenges arose from this application. After photo-activation of an mEos2 emitter, the excitation beam pattern (EBP) needed to be superimposed on the emitter. To that end, a tracking initiation routine was used as will be discussed subsequently. The tracking parameters of the experimental system had to be chosen such that the emitter was not lost during the tracking, even in the case of mEos2 blinking. Amongst other things, this was achieved by optimizing the parameters through a tracking simulation.

This section starts by explaining the sample preparation. Subsequently, the tracking initiation routine is discussed and the tracking parameter settings are motivated. Next, the data processing as well as the experimental results are presented. Thereby, a focus is set on the evaluation of the tracking performance. This includes assessment of the number of localizations per track, the diffusion coefficient estimation precision as well as the tracking error. Finally, the results are compared to state-of-the-art camera tracking performances.

### 4.4.1 Sample preparation

*E. coli* BW25993 strains with mEos2 fused to the ribosomal small subunit protein S2 were obtained from the research lab of Johan Elf (cf. Sanamrad et al. (2014)) and stored as freezer cultures.

*M9* minimal media was obtained by heating 928 ml of Milli-Q water to (30 – 50)° C to prevent *Ca* precipitation. Subsequently, 0.1 mM *CaCl*<sub>2</sub>, 1x *M9* salts, 0.4% Glucose and 2 mM *MgSO*<sub>4</sub> were added. The solution was filtered (suction filter: 0.2 μm) and stored at room temperature.

Overnight cultures were grown from freezer cultures by incubation shaking at 37° C in *M9* minimal media supplemented with 0.4% glucose and 1640 amino acids (RPMI 1640 Amino Acids Solution (50x), Sigma-Aldrich). Cultures were inoculated from overnight cultures by the analogue process, until an optical density at 600 nm of  $OD_{600} = 1.5$  was reached. The cells were pelleted by centrifuging at 4000 rpm for 4 min, and resuspended in fresh growing media in order to attain  $OD_{600} = 1.5$  again.

Clean coverslips and objective slides were used (see sec. 3.2.1). The cells were placed on 2.5% agarose pads (SeaPlaque GTG Agarose, Lonza) obtained using

fresh growing media. Immobilization was attained by squeezing the agarose pad between a clean microscope slide and a clean coverslip. The latter was attached using a frame seal (Frame-Seal Slide Chambers SLF0601, Bio-Rad Laboratories GmbH).

## 4.4.2 Data acquisition

### Tracking initiation

The employed EBP in combination with the mLMS estimator works only in a finite region surrounding the EBP center, as discussed in sec. 4.1.1 and visualized in fig. 4.1. To superimpose the EBP on the emitter an initial localization routine is needed.

A Gaussian shaped excitation beam at 560 nm with  $fwhm \approx 320$  nm was scanned over the  $1.9 \times 1.9 \mu\text{m}$  field of view of the electro-optical deflectors. Thereby, APD 2 was used for photon detection. The mEos2 emitters were switched to the ON state by a focused Gaussian shaped 405 nm activation beam. It was applied centered on the scanned field of view with a periodicity of 3 Hz and a pulse length of 1 ms. The pixel size of the scan was set to 127 nm with pixel dwell times of  $50 \mu\text{s}$ . The scan was repeated until an activated mEos2 molecule was detected - a photon detection threshold of 15 needed to be surpassed in a pixel. The scanning routine as well as the activation were stopped, and an emitter localization was launched around the center of the corresponding pixel. This localization was implemented by four Gaussian beam exposures. Two were placed at  $x_{b_{0,1}} = \pm L/2$  in order to estimate the  $x$  position of the molecule. The analogue was done with two further Gaussian beams for the  $y$  position estimation. The beam separation  $L$  was set to 300 nm. The multiplex cycle timings used a gate delay of  $10 \mu\text{s}$ , an excitation and detection gate of  $38 \mu\text{s}$  and a localization window of  $2 \mu\text{s}$  (see fig. 3.2). The localization was carried out in  $198 \mu\text{s}$ . Live position estimation employed the MLE (see eq. (2.53) and sec. 2.2.1). Photon numbers of  $N \approx 60$  ensure a localization precision of  $\sigma \leq 30$  nm in a field of view of about 300 nm surrounding the Gaussian EBP center (see fig. 2.5 (D-E)). In the experimental conditions, a mean of  $\langle N \rangle = 53$  photons was measured.

Subsequently, the MINFLUX tracking routine was launched. When terminated, the tracking initiation routine was restarted. Note that an additional 405 nm activation timeout of 10 s was introduced, to reduce the probability of having multiple activated mEos2 emitters present.



### The MINFLUX tracking routine

The four-doughnut EBP with  $fwhm \approx 450$  nm introduced in sec. 2.1.2 was employed using 560 nm excitation (Laser 2, see fig. 3.1). The multiplex cycle rate was 8 kHz, with a gate delay of  $7.4 \mu\text{s}$ , an excitation and detection gate of  $23.3 \mu\text{s}$  and a localization window of  $2 \mu\text{s}$ .  $L$  was set to 130 nm. The excitation power ranged between  $(50 - 100) \mu\text{W}$ . Photons were detected with APD 2. Live position estimation was calculated using the mLMS estimator  $\hat{r}_{mLMS}^{(1)}$  of eq. (4.1) with parameters  $k_i = 1.2$  and  $\beta_1 = 3$ . The parameter choice is based on the simulation results as discussed in sec. 4.1.2. To prevent the EBP from being background driven when the emitter is in a fluorescent OFF state, a 6 photon reaction threshold was implemented on the total counts acquired per multiplex cycle. This threshold ensured a probability below 2% to react to background counts for the measured background levels.

### 4.4.3 Data processing and experimental results

A collection of 1667 single emitter tracks was recorded from 27 different E. coli cells at room temperature using the previously described tracking routine. The acquisition of transmission images in regular time intervals showed that the E. coli embedded on the agarose pads grew and cell division took place in the entire time span of the data acquisition, indicating that the cells were indeed alive.

**Trace segmentation** The measured trajectories consisted of two segments. A first one in which an emitter is tracked and, after emitter bleaching/losing, a segment that is driven by background contributions only. The segments were isolated by manual inspection. To classify as a successful trajectory, the average central doughnut ratio  $\langle n_0 / \sum_i n_i \rangle$  needed to fulfill  $\langle n_0 / \sum_i n_i \rangle < 0.23$ , with  $n_i$  the counts obtained in the  $i^{\text{th}}$  doughnut exposure of a multiplex cycle. When no emitter is present, a value of  $\langle n_0 / \sum_i n_i \rangle = 0.25$  is expected. Trajectories with unusually long OFF times ( $\gtrsim 100$  ms) were separated into two independent trajectories. Likewise, events of unusually high count rates ( $\geq 150$  kHz) with central doughnut ratio values  $\geq 0.25$  were cut out to exclude potential multi-emitter contributions. The applied selection criteria resulted in 1535 tracks used for further analysis. The track length distribution is approximately exponential with mean of 157 ms as visualized in fig. 4.5 (A).

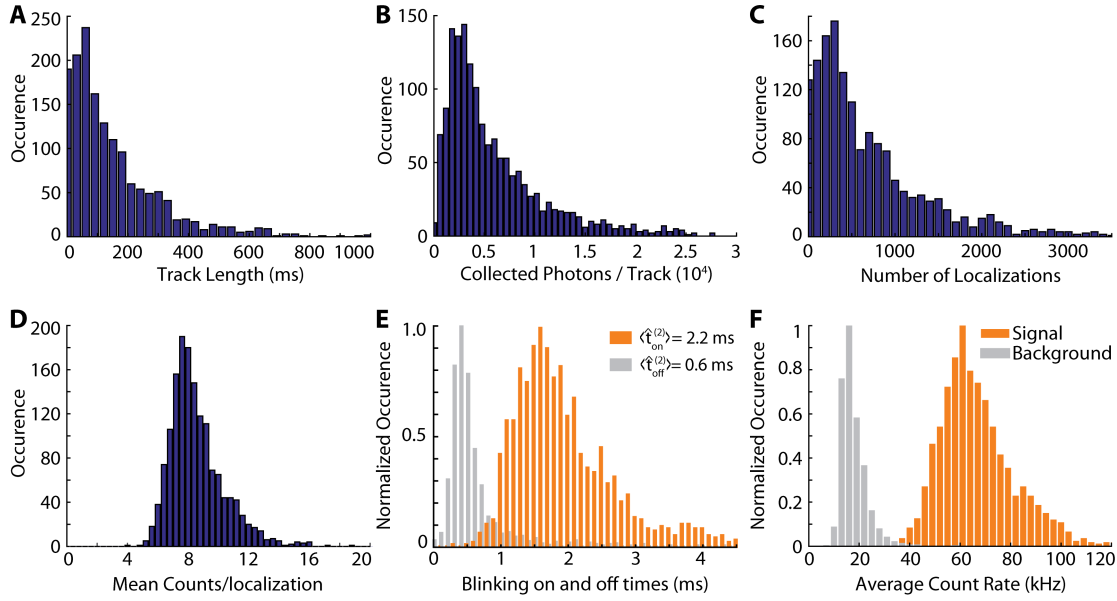


Figure 4.5: **(A)** Track length occurrences with a mean of 157 ms obtained from the 1535 measured tracks in living *E. coli*. All stated mean values of the distributions in (A-C) are the parameter value (i.e. average) of the respective non-truncated exponential distributions. Note that truncated distributions have higher averages than reported. **(B)** Total number of collected emitter photons (background corrected) per trace with a mean of 5803. **(C)** Total number of valid localizations per trace with a mean of  $\langle S \rangle \approx 742$  after iterative application of the Viterbi algorithm. A valid localization is defined as belonging to the emitter ON state and having more than 3 total photons. Note that the distributions in (A-C) extend further from the visualized plot limits. The longest measured track was 1444 ms with a total of 86009 collected emitter photons and 7503 valid localizations. **(D)** Mean total counts acquired per multiplex cycle for the respective measured tracks. The ensemble average is calculated to 9 photons per localization. **(E)** Normalized occurrences of the estimated blinking ON and OFF times  $\hat{t}_{on}^{(2)}$  and  $\hat{t}_{off}^{(2)}$ . **(F)** Normalized occurrences of the average signal count rates  $\Gamma_s^{(2)}$  in the ON state as well as the background count rates  $\Gamma_b^{(2)}$  in the OFF state. The average signal-to-background ratio is  $\langle \text{SBR}^{(2)} \rangle \approx 2.8$ , with  $\langle \Gamma_s \rangle \approx 68$  kHz and  $\langle \Gamma_b \rangle \approx 18$  kHz. Figure adapted from Balzarotti et al. (2016).

**Identification of mEos2 blinking events** To identify molecule blinking events, a simple two stage hidden Markov model (HMM) was employed on the total photon vector  $\bar{N}$ , with entries  $N_j = \sum_{i=1}^4 n_i$  representing the photons collected in the  $j^{\text{th}}$  multiplex cycle. Two emission states (state 1: emitter ON, state 2: emitter OFF) were assumed. They were presumed to follow Poissonian statistics with parameter  $\lambda_{on}$  and  $\lambda_{off}$ , respectively. The blinking ON and OFF times were assumed to follow exponential distributions with mean  $t_{on}$  and  $t_{off}$ . Estimation of the most probable state path employed the Viterbi algorithm implemented as “hmmviterbi” in the Matlab Statistics Toolbox. It requires the probability density function (here a Poissonian distribution) as input as well as initial parameter estimates for  $\lambda_{on}$  and  $\lambda_{off}$ . Furthermore, a transition matrix  $T$  estimate is needed

$$T = \begin{pmatrix} p_{11} & p_{12} \\ p_{21} & p_{22} \end{pmatrix} \quad (4.11)$$

where  $p_{ij}$  is the probability to undergo a state transition from state  $i$  to state  $j$ . For a multiplex cycle time  $\Delta t_c$  the transition probability from state 1 (ON) to state 2 (Off) is given by:

$$p_{12} = \frac{1}{t_{on}} \int_{t=0}^{\Delta t_c} e^{-\frac{t}{t_{on}}} dt = 1 - e^{-\frac{\Delta t_c}{t_{on}}} \approx \frac{\Delta t_c}{t_{on}} \quad (4.12)$$

In the first stage, noted by a (0) superscript,  $T$  was initialized as

$$T^{(0)} = \begin{pmatrix} 1 - \frac{\Delta t_c}{\hat{t}_{on}^{(0)}} & \frac{\Delta t_c}{\hat{t}_{on}^{(0)}} \\ \frac{\Delta t_c}{\hat{t}_{off}^{(0)}} & 1 - \frac{\Delta t_c}{\hat{t}_{off}^{(0)}} \end{pmatrix} \quad (4.13)$$

with initial estimates  $\hat{t}_{on}^{(0)} = 3$  ms and  $\hat{t}_{off}^{(0)} = 1$  ms.

The initial estimates for the parameter  $\lambda_{on}$  and  $\lambda_{off}$  can be estimated using the total photon vector  $\bar{N}$  as subsequently discussed. Let  $P(\lambda_{on}, t | x, t_0)$  be the probability of having state 1 with Poissonian mean  $\lambda_{on}$  at time point  $t$ , given that the system was in state  $x$  at time  $t_0$ . For the assumption of a memoryless continuous-time stochastic process that shows two distinct values (ON and OFF) the time dependence of  $P(\lambda_{on}, t | x, t_0)$  follows the master equation:

$$\frac{\partial}{\partial t} P(\lambda_{on}, t | x, t_0) = -\frac{1}{t_{on}} P(\lambda_{on}, t | x, t_0) + \frac{1}{t_{off}} P(\lambda_{off}, t | x, t_0) \quad (4.14)$$

It reaches the stationary state:

$$\lambda = \left( \frac{\lambda_{on}}{t_{off}} + \frac{\lambda_{off}}{t_{on}} \right) \left( \frac{1}{t_{on}} + \frac{1}{t_{off}} \right)^{-1} \quad (4.15)$$

This result can be used to obtain the initial estimates for  $\lambda_{on}$  and  $\lambda_{off}$

$$\hat{\lambda}_{on}^{(0)} = \langle \bar{N} \rangle \cdot \frac{\hat{t}_{on}^{(0)} + \hat{t}_{off}^{(0)}}{\hat{t}_{on}^{(0)} + \frac{\hat{t}_{off}^{(0)}}{\text{SBR}^{(0)} + 1}}, \quad \hat{\lambda}_{off}^{(0)} = \frac{\hat{\lambda}_{on}^{(0)}}{\text{SBR}^{(0)} + 1} \quad (4.16)$$

where  $\lambda = \langle \bar{N} \rangle$  was used. The mean total photons per multiplex cycle  $\langle \bar{N} \rangle$  can be estimated from the measured track.  $\langle \bar{N} \rangle$  is the ML estimate of the parameter  $\lambda$ . The average signal-to-background is given by:

$$\text{SBR} = \frac{\lambda_{on}}{\lambda_{off}} - 1 \quad (4.17)$$

Initially, it was set to  $\text{SBR}^{(0)} = 4$ .

The transition matrix  $T^{(0)}$  and the Poissonian probability density functions with mean  $\hat{\lambda}_{on}^{(0)}$  and  $\hat{\lambda}_{off}^{(0)}$  were employed for state path estimation. As a result, each multiplex cycle was attributed to state 1 or 2. To improve the obtained state emission estimates, a further iteration was calculated.

All ON and OFF times  $\bar{t}_{on}$  and  $\bar{t}_{off}$  were extracted as two vectors from the track. These times were assumed to follow truncated exponential distributions, as time intervals shorter than the sampling time were not collected. The updated parameter estimates  $\hat{t}_{on}^{(1)}$  and  $\hat{t}_{off}^{(1)}$  were obtained from the MLE:

$$\hat{t}_{on}^{(1)} = \langle \bar{t}_{on} \rangle - \Delta t_c, \quad \hat{t}_{off}^{(1)} = \langle \bar{t}_{off} \rangle - \Delta t_c \quad (4.18)$$

The new estimates were employed to update eq. (4.13). The state path allowed the classification of the total counts per multiplex cycle vector  $\bar{N}$ . This enabled the estimation of the emission probability distributions for the ON and the OFF state as well as the estimation of the average signal count rate in the ON state  $\Gamma_s^{(1)}$  and the average background count rate in the OFF state  $\Gamma_b^{(1)}$ . The estimation of the average signal-to-background ratio  $\text{SBR}^{(1)}$  is then given by:

$$\text{SBR}^{(1)} = \frac{\Gamma_s^{(1)}}{\Gamma_b^{(1)}} - 1 \quad (4.19)$$

The Viterbi algorithm was applied a second time using the parameters with superscript (1). From the resulting state path the final estimates  $\hat{t}_{on}^{(2)}$  and  $\hat{t}_{off}^{(2)}$  were obtained. Their distribution is visualized in fig. 4.5 (E). The mean values were calculated to  $\langle \hat{t}_{on}^{(2)} \rangle \approx 2.2$  ms and  $\langle \hat{t}_{off}^{(2)} \rangle \approx 0.6$  ms. This corresponds to an ON time of 18 and OFF time of 5 multiplex cycles in average.

Subtraction of the average background from the signal photons enabled calculation of the total number of emitter photons per track. The resulting distribution is shown in fig. 4.5 (B). Panel (F) visualizes the signal count rate  $\Gamma_s^{(2)}$  and the background count rate  $\Gamma_b^{(2)}$ . These rates enabled the calculation of the average signal-to-background ratio per track  $SBR^{(2)}$ . This average was used for the numLMS trajectory correction discussed below. Using the average value is an approximation, given that emitters at different positions of the EBP have different SBR values. Yet for a beam separation of  $L = 130$  nm and typical tracking error distribution ( $\approx (30 - 40)$  nm), the variation in the SBR values of the respective multiplex cycles is expected to be small. For the tracking application in E. coli for example, the SBR is approximated to  $SBR \approx 2.7$  with fluctuations of  $\sigma_{SBR} \approx 1$ . Note that the SBR distribution in a track is asymmetric with a larger tail toward high SBR values.

The state path also allowed the determination of the total number of localizations  $S$  in each trajectory by counting all multiplex cycles belonging to the emitter ON state. Note that all localizations belonging to the OFF state as well as localizations with less than 3 total counts were discarded in the estimation of  $S$  as well as in the further processing steps. The resulting number of localizations per track distribution is visualized in fig. 4.5 (C). The mean is estimated to  $\langle S \rangle \approx 742$  valid localizations per track.

Figure 4.6 (A) shows a representative transmission image of an E. coli cell overlain with 77 independent tracks. These consist of all valid localizations as retrieved after the state path classification. Panel (B) shows the details of one track. The count rate of the central doughnut exposure ( $\bar{r}_0$ , blue line) produces a lower count rate than the peripheral exposures, indicating that the emitter was indeed well centered while tracking. The measured tracks consist of segments in which the emitter is in the ON state, separated by short emitter OFF intermittencies. A gray line indicates a 2 ms excerpt. The corresponding count rate as well as the  $x$  and  $y$  trajectory values are visualized in panel (C). The identified ON and OFF states are indicated.

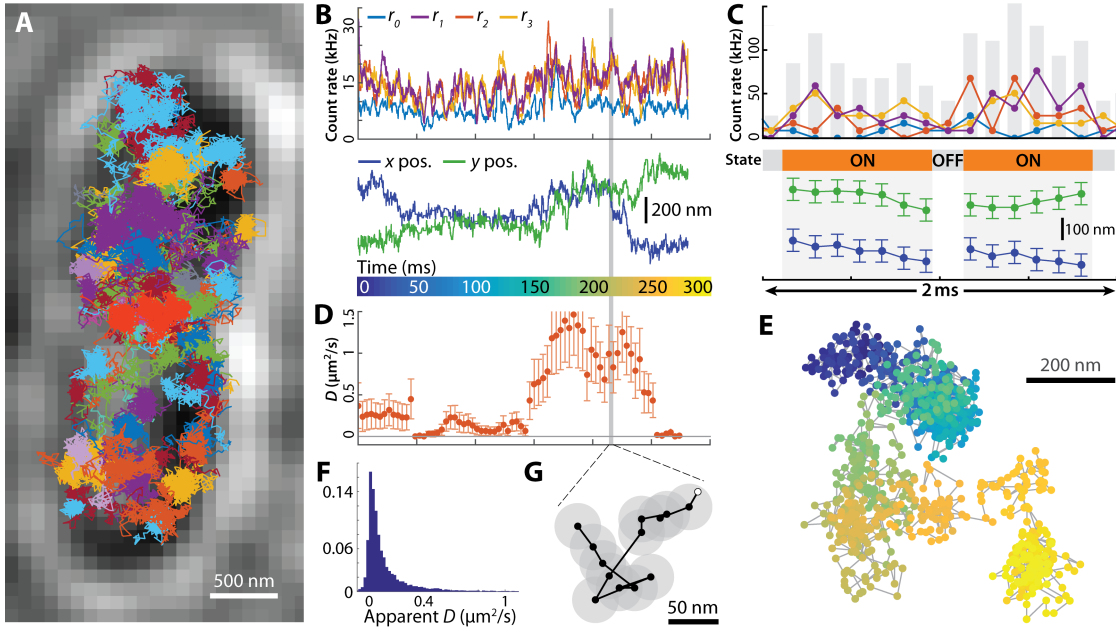


Figure 4.6: (A) Transmission image of an *E. coli* bacteria. 77 MINFLUX tracks of single 30S ribosomal protein subunits fused to the switchable fluorescent protein mEos2 are overlaid. (B) *Upper panel*: Low pass filtered count rate of the four doughnut exposures of the multiplex cycle. Filtering used a 5 ms moving average filter. The average total count rate was  $\Gamma_{tot} \approx 52$  kHz. *Lower panel*: extracted raw MINFLUX  $x$  and  $y$  coordinates of the trajectory with time resolution of 125  $\mu$ s. This represents a 100-fold improvement over current camera tracking results in living cells using fluorescent proteins (cf. table 4.1). (C) 2 ms excerpt of the trace in (B) (highlighted by a gray line at time point 210 ms). *Upper panel*: obtained counts per doughnut exposure are shown together with their sum (gray bars). The latter was used for ON/OFF state path classification as described in the text. *Middle panel*: retrieved ON/OFF classification. *Lower panel*: extracted raw  $x$  and  $y$  coordinates. Error bars indicate the average tracking error of 48 nm (cf. fig. 4.7 (A)). (D) Apparent diffusion constants  $D$  obtained from an OLSF fit to the MSD for a sliding window of 35 ms with approximated error bars of 1.4 times the CRB of eq. (4.5). (E, G) Trajectories shown in (B) and (C), respectively. The diameter of the shaded circles in (G) visualize the average tracking error. Open white circles represent localizations attributed to the emitter OFF state. (F) Normalized occurrences of apparent diffusion constants  $D$  for all measured tracks. Obtained from an OLSF fit to the MSD for a sliding window of 35 ms every 17.5 ms on the respective tracks. Figure adapted from Balzarotti et al. (2016).

**Trajectory reconstruction** The tracks in the experiment were recorded employing the live position mLMS estimator  $\hat{r}_{mLMS}^{(1)}$  of eq. (4.1) as explained in sec. 4.4.2. This estimator is biased (see sec. 2.2.2 and fig. 2.6) and causes MSD curves retrieved from the tracks to deviate from the linear relationship of eq. (4.7) (see sec. 4.2.2 and fig. 4.3). Thus, in order to obtain an improved trajectory estimation, the tracks were corrected by the numLMS estimator  $\hat{r}_{numLMS}^{(2)}(\hat{p})$  in post processing. As explained in sec. 2.2.2, the numLMS estimator construction requires the knowledge of the ground truth success probability  $\bar{p}(\bar{r})$  as well as the SBR. The latter was obtained as illustrated in the previous paragraph. The success probability  $\bar{p}(\bar{r})$  was measured according to the protocol of sec. 3.2. The success probability  $\hat{p}$  estimates of the respective multiplex cycles were obtained employing their MLE given by eq. (2.51).

**Diffusion coefficient and localization precision estimation** The diffusion coefficients  $D$  were estimated for 35 ms sliding windows of each trajectory. The diffusivity was obtained from the numLMS corrected tracks using the adapted OLSF estimator introduced in sec. 4.2.2. The MSD curves were calculated according to eq. (4.8), where the emitter ON and OFF intermittencies were obtained from the state path calculated using the Viterbi algorithm. Note that ON states with less than 3 localizations were attributed to the OFF state.

Figure 4.6 (F) visualizes the distribution of obtained diffusivity  $D$  estimates for 35 ms sliding windows with a spacing of 17.5 ms. The quartiles (25 %, 50 %, 75 %) are given by  $D = (0.02, 0.07, 0.15) \mu\text{m}^2/\text{s}$  with a mean of  $\langle D \rangle = 0.13 \mu\text{m}^2/\text{s}$ . The results show that the vast majority of ribosomal small subunit protein S2 have low diffusion coefficients, which is in agreement with results obtained in Sanamrad et al. (2014).

Figure 4.6 (D) shows the retrieved diffusivity values of the 35 ms sliding windows with a spacing of 3.75 ms. For every time window, the error bars ( $\pm\sigma$ ) were approximated as 1.4 times the diffusion estimation CRB of eq. 4.5. This approach is validated by the  $D$  estimation precision obtained from simulations (see sec. 4.2.2 and fig. 4.3). The plot reveals transient behavioral changes in the emitter diffusivity. Note that every window used for  $D$  estimation can have up to 280 localizations.  $D$  estimations utilizing less than 100 valid localizations were discarded.

In addition to the diffusion coefficient  $D$  estimation, the adapted OLSF estimator permits the estimation of the average tracking error  $\epsilon$ . An error estimation was obtained from the MSD of the complete numLMS corrected track. Figure 4.7 (A) visualizes the retrieved tracking error  $\epsilon$  against the mean number of photons per

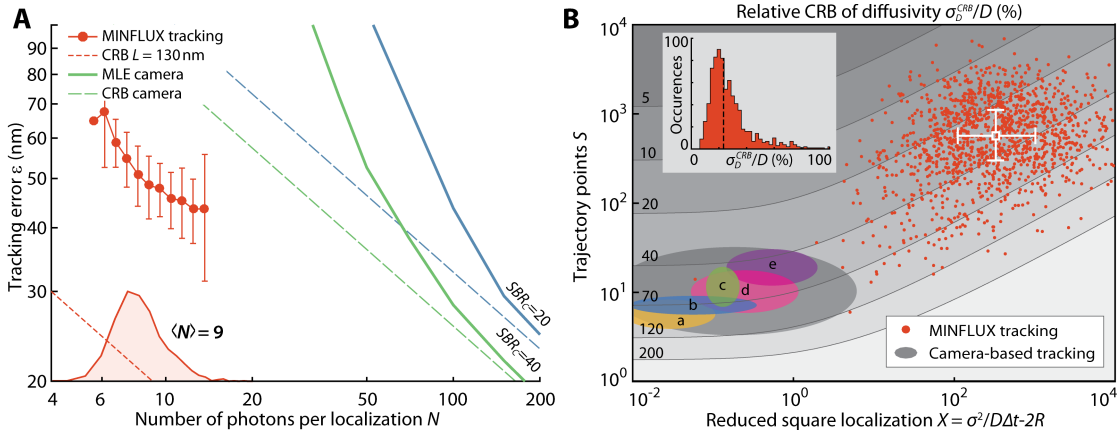


Figure 4.7: **(A)** Estimated tracking error  $\epsilon$  (red circles) as a function of the average counts per MINFLUX localization  $N$  for all measured and numLMS corrected tracks. The error estimation was obtained from an OLSF fit to the MSD curves of the respective tracks as described in the text. The marginal distribution of the average total counts per multiplex cycle  $N$  is inserted. In average  $\langle N \rangle \approx 9$  photons were used per localization. The CRB of a MINFLUX localization at the origin (EBP center) for a static emitter is plotted as a red dotted line for the used beam separation of  $L = 130$  nm. The idealized static camera MLE localization performance is shown as a solid line and its CRB as a dashed line for two relevant signal-to-background ratios  $SBR_c$  of 20 and 40. Compared to the idealized camera MLE performance, MINFLUX tracking in living *E. coli* shows a 5- to 10-fold improvement of the photon-efficiency. **(B)** Comparison of the relative CRB of diffusivity  $\sigma_D^{CRB}/D$  attainable by MINFLUX tracking compared to state-of-the-art camera tracking results. Contour lines of  $\sigma_D^{CRB}/D$  are shown as a function of the trajectory length  $S$  and the reduced localization precision  $X$ . The experimental  $S$  and  $X$  values obtained by MINFLUX tracking are overlain as red dots. The white cross shows the quartiles (25%, 50% and 75%) of the marginal distributions of  $S$  and  $X$ . Simulations showed that the diffusion estimator, though not optimal yet, provides acceptable results which deviate by a factor of about 1.4 from its theoretical limit (see fig. 4.3 (D)). The gray ellipse represents the  $[S, X]$  regime obtained with state-of-the-art camera tracking of fluorescent proteins (colored ellipses refer to table 4.1). The inset shows the distribution of  $\sigma_D^{CRB}/D$  for tracks with more than 500 localizations, which encompasses about 50% of the data (cf. fig. 4.5 (C)). The median of that distribution lies at 23%. Figure adapted from Balzarotti et al. (2016).



Ref.	Probe	$D$ ( $\mu\text{m}^2/2$ )	$\sigma$ (nm)	$\Delta t$ (ms)	Length (ms)	Aver. Loc.	Cut off
(a) Stracy, 2015	RNAP- PAmCherry	7-8	40	15	85	5.6	4
(b) Sanamrad, 2014	L1-mEos2 S2-mEos2	0.06 bound 0.4 free	20 60	20	180	9	5
(c) Li, 2016	RelA-YFP RelA-mEos2 RelA-Dendra2 S2-mEos2	1.52 0.64 0.32 0.05	45	10	90-150	> 9-15	6-10
(d) Bakshi, 2012	S2-YFP	0.04	10-30	30	150-180	5-6	8-13
(e) Manley, 2008	VSVG-EosFP Gag-EosFP	0.14 0.11	25	50	250	4-5	15

Table 4.1: Results and parameter values of typical camera tracking experiments in living cells using fluorescent protein labels. The cutoff states the minimum number of localizations used for  $D$  estimation. Table reproduced from Balzarotti et al. (2016).

localization  $\langle N \rangle$ .  $\langle N \rangle$  was estimated from the total counts vector  $\vec{N}$ , where only vector entries belonging to the ON state were used. Subsequently, the tracking error values of the respective tracks were binned according to their  $\langle N \rangle$  values, and the mean and standard deviation calculated. A mean tracking error of  $\langle \epsilon \rangle < 48$  nm was obtained by detecting an average of just 9 photons per localization with a time resolution  $\Delta t_c$  of 125  $\mu\text{s}$ .

#### 4.4.4 Summary and discussion

The ribosomal small subunit protein S2 fused to the switchable fluorescent protein mEos2 was tracked in living E. coli. In order to superimpose the MINFLUX excitation beam pattern with an activated mEos2 emitter, a tracking initiation routine was implemented. Tracking parameters were chosen according to the obtained simulation results which took into account previously published diffusion coefficients as well as measured emitter blinking time scales. The beam separation was set to  $L = 130$  nm with a multiplex cycle rate of 8 kHz. To prevent losing the target molecule due to emitter fluorescence ON and OFF intermittencies, a reaction threshold was implemented on the total counts per multiplex cycle. The combination of a piezo tip/tilt mirror with electro-optical scanners allowed covering a micrometer sized region while providing beam steering capabilities on microsecond timescales.

Measurements in 27 living *E. coli* cells yielded 1535 tracks. The identification and separation of successful tracking events from purely background driven segments was achieved by manual selection. Emitter ON and OFF intermittencies were identified by a simple two state hidden Markov model. Estimations of the diffusion coefficient  $D$  as well as of the average tracking error  $\langle\epsilon\rangle$  were obtained from an adapted OLSF algorithm. The resulting photon-efficiency of the numLMS corrected tracks was 5- to 10-fold higher than its idealized camera pendant at equal tracking error. An average error of  $\langle\epsilon\rangle < 48$  nm was obtained for an average number of  $\langle N \rangle = 9$  photons per localization. The time resolution, given by the multiplex cycle rate, was  $\Delta t_c = 125 \mu\text{s}$ . This is an 100-fold improvement over state-of-the-art camera tracking time resolutions obtained with similar probes as is visible from table 4.1.

Furthermore, MINFLUX tracking enabled  $D$  estimation with unparalleled temporal resolution of 35 ms using more than 100 valid localizations. This has to be contrasted with results obtained by typical camera tracking using fluorescent proteins, which obtain  $\lesssim 15$  localizations for an entire track (cf. table 4.1). The MINFLUX data acquisition conditions were adapted in favor of high number of localizations instead of high localization precision values, as it was shown to be the favorable approach for precise diffusion coefficient estimation. Figure 4.7 (B) visualizes the relative diffusion coefficient estimation precision  $\sigma_D/D$  as a function of the number of localizations  $S$  and the reduced squared localization precision  $X$ . The obtained MINFLUX results for  $S$  and  $X$  are superimposed as red markers. An average of 742 localizations per track were achieved, which accounts for an approximately 100-fold improvement over camera tracking results (cf. table 4.1). The theoretical bound of relative  $D$  estimation lies below 23% for half of the measured MINFLUX tracks (see inset in fig. 4.7 (B)) where camera results center around relative precisions of 70%. This suggests a 3-fold improvement in the relative  $D$  estimation.

Note that the obtained MINFLUX tracking results were mainly limited by the mEos2 fluorescence ON and OFF intermittencies. As shown in sec. 4.1.2, a non-blinking probe can be kept in closer proximity to the excitation beam pattern center. This enables the utilization of smaller beam separations  $L$  which would further increase the MINFLUX tracking photons efficiency.

# Chapter 5

## Conclusion and outlook

This work presented a new localization modality termed MINFLUX. By encoding spatial information into the excitation illumination, the information content of the collected photons can be increased significantly. This was illustrated by using an excitation scheme consisting of exposing a single emitter to four displaced doughnuts that feature an intensity zero, respectively. This excitation beam pattern (EBP) was characterized by a triangular geometry of size  $L$ . Theoretical evaluations showed that the Cramér-Rao lower bound (CRB) on the localization precision has a spatial dependence with the lowest values inside of the  $L$ -sized region. For a given number of emitter photons and no background contributions, decreasing  $L$  enabled a proportional decrease of the CRB. Localization estimators were developed and evaluated, and theory as well as experiments showed that the estimators reach the CRB and perform close to optimality starting from low photon numbers ( $\approx 10$ ).

The MINFLUX localization precision dependence on the geometrical parameter  $L$  has to be contrasted to camera localization schemes in which the precision is dependent on the diffraction limit. Each photon that is detected by the camera has a position uncertainty on the order of the diffraction pattern size. In MINFLUX this uncertainty is proportional to the beam separation  $L$ . Thus, camera localization performances can be surpassed simply by reducing  $L$  below the diffraction limit. Experimental measurements on a static fluorescent emitter with  $L = 50$  nm reached a localization precision of 5 nm with only 27 photons, increasing the photon-efficiency by 22-fold compared to the ideal camera performance with finite but very generous background contributions.

One of the main experimental limitations of MINFLUX is background contributions, as these introduce a limit on the minimal  $L$  that leads to an improvement of the localization precision. The use of fused silica coverslips with low auto-fluorescence as well as time gating promise to enable background signal reductions. An additional limiting aspect is certainly the quality of the intensity zero. In this work, doughnut minima on the order of  $< 0.2\%$  of the peak intensity were achieved. The use of beam shaping optics like spatial light modulators (SLM), for example, will help enhance the zero quality. Implementation of these improvements will allow measurement with yet smaller beam separations  $L$  and thus further improve the MINFLUX performance. The use of small  $L$ -values has additional benefits. For small  $L$ , the parabolic approximation of the doughnut excitation beams is valid. This renders the localization process independent of the excitation wavelength and opens up the possibility of employing red shifted excitation wavelengths that can reduce sample auto-fluorescence and potential photo-damage to living cells without compromising the localization precision.

It is noteworthy that the range  $L$  does not constitute a fundamental constraint to MINFLUX. Localizations outside of this range are possible, even though they show reduced localization precision. The combination of MINFLUX with conventional camera (or more generally detector arrays) localization schemes is feasible and would result in uniform localization precision outside of  $L$  with an increased performance inside of it. Furthermore, it is possible to iteratively decrease the beam separation in subsequent localization steps. In this scenario, the localization starts at the diffraction limit, until enough photons are collected to superimpose the EBP.  $L$  can then be decreased gradually. Even though the photons obtained from all used  $L$  values can be employed to localize the emitter, the most photon-efficient, and therefore the most important emitter probing, is the last one. Apart from promising high photon-efficiencies, this scheme has the advantage of reducing localization precision anisotropies present at large  $L$  and relaxes the requirements on the illumination beams. The excitation profile needs to be known in the small  $L$ -sized region around its zero only, where possible deteriorating aberration effects are minimal.

In camera localization the knowledge of the detection PSF is of vast importance for precise emitter localization. The orientation of static emitter dipoles alters the PSF shape and can induce localization errors on the order of tens of nanometers (Engelhardt et al., 2010; Lew et al., 2013). MINFLUX performance, on the other hand, is not deteriorated by the unknown dipole orientation. It certainly has an

influence on the excitation probability, but as the orientation is the same for all excitation beams, the localization precision is not affected. The combination with suitable detection schemes, however, enables measurement of the emitter orientation using polarization information (Mehta et al., 2016).

The reduction of photons needed to obtain high localization precision is of benefit to applications that require high spatio-temporal resolutions and that are limited by photon emission rates. In this work, MINFLUX localization precisions of 2.5 nm with time resolutions of 400  $\mu$ s were achieved, permitting to resolve the fast dynamics of a custom designed DNA origami sample. This comprises a 17-fold increase of the photon-efficiency compared to the ideal camera performance. In combination with the bound of a maximal photon emission rate, the reported spatio-temporal resolutions are unattainable using camera localization for a wide range of probes, including the used ATTO 647N. MINFLUX, on the other hand, will further be enhanced in future implementations, e.g. by reduction of system instabilities.

Furthermore, a 100-fold improvement of the time resolution in a single molecule tracking implementation in native cellular environments was achieved by tracking and keeping an emitter in the photon-efficient region of the EBP. This improved the photon-efficiency by a factor of 5 to 10 compared to ideal cameras. The obtained performance was mainly limited by emitter blinking. When the emitter is in the fluorescent OFF state it can diffuse away from the proximity of the EBP, such that large  $L$  values are required in order not to lose the emitter. It is foreseeable that EBP adaptations in combination with live position estimation improvements will solve this problem. More importantly, the employment of non-blinking probes will enable reduction of  $L$ . This can significantly increase the MINFLUX spatio-temporal resolution, and thus further enhance the measurement and characterization of emitter dynamics (e.g. the diffusion coefficient estimation).

The use of illumination schemes that adapt to possible transient emitter behavior promise further performance improvements. These include the use of optimal  $L$ -values dependent on the dynamics, such as enlarging  $L$  for trajectory parts with high diffusivity and reducing it for slow moving segments. Furthermore, conditional excitation schemes are implementable. An emitter that is temporarily stationary can be probed by the central doughnut exposure only. The superimposed illumination zero ideally requires no photons to confirm the immobility of

the emitter. Once the emitter moves, the photon emission rate increases, and the four-exposure excitation pattern can be launched again.

In general, MINFLUX offers the possibility to alter the excitation scheme in order to optimize for different performance metrics. These can encompass speed, large field of views, local precision maximization, light dose minimization or the extension to the third dimension. By displacing a z-doughnut in the axial direction (Klar et al., 2000), z-position information can be obtained that will render isotropic localization precision and tunable photon-efficiency in 3D reality. Furthermore, MINFLUX parallelization by implementation of multiple field of views with arrays of point, line or plane shaped zeros are foreseeable.

The combination of MINFLUX with the stochastic ON and OFF switching of close-by emitters creates the possibility to image structures with high precision and enhanced recording times due to the increased photon-efficiency. These benefits promise to have a huge impact on the field of superresolution. In its current experimental implementation MINFLUX localization precisions below 1 nm have already enabled resolving molecules only 6 nm apart (Balzarotti et al., 2016). These represent distance scales where molecules already interact with each other, which suggests that MINFLUX can potentially rival Förster resonance energy transfer (Schuler et al., 2002; Padilla-Parra and Tramier, 2012). Microscopes that adapt the excitation illumination on extended fields of view, e.g. by generating an EBP at positions where emitters spontaneously activate, promises the applicability of MINFLUX nanoscopy to the observation of large structures. Likewise, beam scanning implementations with targeted activation and MINFLUX position readout bear strong potential. The extension to multicolor/multispecies imaging and tracking will broaden the versatility of this new localization scheme to study fundamental processes in living organisms at their characteristic length and timescale in 2D and 3D, triggering new insights and adding up to the many findings already obtained with single molecule studies.

The genuine flexibility of tuning the localization precision for a given photon-budget through MINFLUX opens up the possibility of localizing fluorescent emitters with unrivaled spatio-temporal resolutions and will additionally allow the tracking and imaging of probes with reduced brightness, for example, using auto-fluorescent or other types of luminophores. Taking additionally its conceptual simplicity into account, it has the potential to become the method of choice in a multitude of experiments that localize single molecules and are limited by photon emission rates, bleaching or slow recording.







# Appendix A

## Tracking error for constant localization noise contributions

In this section the tracking error of a simplified system is derived analytically for tracking a diffusive movement with constant localization noise contribution in every controller update. The underlying control loop of the system is shown in fig. A.1 (A). Here  $x_n$  denotes the position of the excitation beam pattern (EBP),  $u_n$  is the position of the emitter, which is assumed to be the summation of white noise contributions  $w_n$ .

$$u_n = u_{n-1} + w_n \quad (\text{A.1})$$

Thereby, the increments  $w_n$  have a variance given by  $E(w_n^2) = 2D\Delta t_c$ , with  $D$  being the diffusion coefficient and  $\Delta t_c$  the update time of the controller. Thus, a diffusive movement is approximated by a random walk. The error  $e_n$  is defined as

$$e_n = u_n - x_n \quad (\text{A.2})$$

which is the distance between the emitter and the last controller position. The localization process is assumed to introduce the *constant* localization noise contribution  $v_n$  that is assumed to be white noise and therefore uncorrelated with variance  $E(v_n^2) = \sigma_v^2$ . The updated controller position is given by

$$x_{n+1} = x_n + k_i (e_n + v_n) \quad (\text{A.3})$$

where an integral controller constant  $k_i$  was introduced. Note that the controller position  $x_n$  is not the estimate of the emitter position  $u_n$  but of  $u_{n-1}$ .

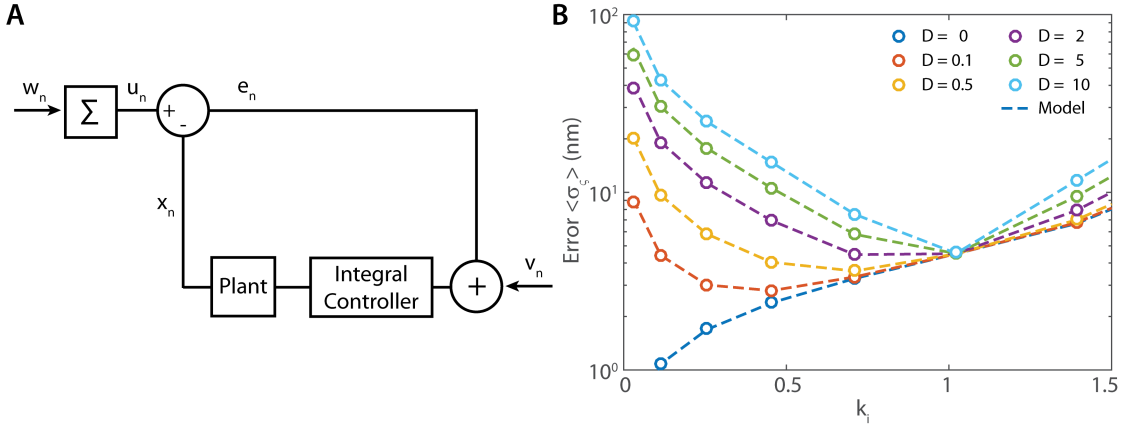


Figure A.1: (A) Simplified block diagram of the tracking routine with an integral controller. The plant, given by the electro-optical deflectors in the setup (see sec. 3.1), has a response time on the order of  $10 \mu\text{s}$ . Compared to typical controller update times of  $125 \mu\text{s}$  it can be ignored. The variables are defined in the text. (B) Comparison of the error model of eq. (A.6) for constant localization noise contributions  $\sigma_v = 30 \text{ nm}$ . Units of  $D$  in legend in  $\frac{\mu\text{m}^2}{\text{s}}$ .

Therefore, it makes sense to define the error  $\zeta_n = u_n - x_{n+1}$ . This definition characterizes the error between the emitter position  $u_n$  and its position estimate  $x_{n+1}$ . The error  $\zeta_n$  follows the recursion:

$$\zeta_n = u_n - x_{n+1} = (1 - k_i)\zeta_{n-1} + (1 - k_i)w_n - k_iv_n \quad (\text{A.4})$$

Using that white noise is uncorrelated, and therefore  $E(v_nv_m) = E(w_nw_m) = 0 \forall n \neq m$  as well as  $E(v_nw_m) = 0 \forall n, m$ , we get

$$E(\zeta_n^2) \equiv \sigma_\zeta^2 = E\left((u_n - x_{n+1})^2\right) \quad (\text{A.5})$$

$$\Rightarrow \sigma_\zeta^2 = \frac{k_i}{2 - k_i}\sigma_v^2 + \frac{(1 - k_i)^2}{k_i(2 - k_i)}2D\Delta t_c \quad (\text{A.6})$$

where  $E(v_n^2) = \sigma_v^2$  and  $E(w_n^2) = 2D\Delta t_c$  was used. Comparison of this analytic result to simulation is visualized in fig. A.1 (B). The good agreement is evident.

This yields an illustrative example of the influence of the integral parameter  $k_i$  on the tracking error  $\sigma_\zeta$ . Low  $k_i$  values reduce the localization noise contributions  $\sigma_v$  to the tracking error but cause a position set point to be reached after multiple steps only and thus increase the error contribution from the emitter movement. In consequence, there is an optimal value balancing out both contributions to minimize the tracking error.

Note that it does not represent the tracking error of MINFLUX, where the localization error is not constant in every update but depends on the position the molecule is at. This makes the analytical tracking error derivation challenging and was not pursued further in this work.



# Appendix B

## Supplementary figures and tables

$d$	$K$	$\mathbf{p}_i^{(0)}$	$F_{\bar{p}}/N$	$J^*$	$\tilde{\sigma}_{CRB}$
1	2	$\frac{I_i}{I_0+I_1}$	$p_0^{-1} + p_1^{-1}$	$\frac{\partial p_0}{\partial r_0}$	$\sqrt{\text{tr}(F_{\bar{r}_m}^{-1})}$
1	3	$\frac{I_i}{I_0+I_1+I_2}$	$\begin{bmatrix} p_0^{-1} & 0 \\ 0 & p_1^{-1} \end{bmatrix} + p_2^{-1}\mathbf{1}$	$\begin{bmatrix} \frac{\partial p_0}{\partial r_0} \\ \frac{\partial p_1}{\partial r_1} \end{bmatrix}$	$\sqrt{\text{tr}(F_{\bar{r}_m}^{-1})}$
2	3	$\frac{I_i}{I_0+I_1+I_2}$	$\begin{bmatrix} p_0^{-1} & 0 \\ 0 & p_1^{-1} \end{bmatrix} + p_2^{-1}\mathbf{1}$	$\begin{bmatrix} \frac{\partial p_0}{\partial r_0} & \frac{\partial p_0}{\partial r_1} \\ \frac{\partial p_1}{\partial r_0} & \frac{\partial p_1}{\partial r_1} \end{bmatrix}$	$\sqrt{\frac{1}{2} \text{tr}(F_{\bar{r}_m}^{-1})}$
2	4	$\frac{I_i}{I_0+I_1+I_2+I_3}$	$\begin{bmatrix} p_0^{-1} & 0 & 0 \\ 0 & p_1^{-1} & 0 \\ 0 & 0 & p_2^{-1} \end{bmatrix} + p_3^{-1}\mathbf{1}$	$\begin{bmatrix} \frac{\partial p_0}{\partial r_0} & \frac{\partial p_0}{\partial r_1} & \frac{\partial p_0}{\partial r_2} \\ \frac{\partial p_1}{\partial r_0} & \frac{\partial p_1}{\partial r_1} & \frac{\partial p_1}{\partial r_2} \\ \frac{\partial p_2}{\partial r_0} & \frac{\partial p_2}{\partial r_1} & \frac{\partial p_2}{\partial r_2} \end{bmatrix}$	$\sqrt{\frac{1}{2} \text{tr}(F_{\bar{r}_m}^{-1})}$
3	4	$\frac{I_i}{I_0+I_1+I_2+I_3}$	$\begin{bmatrix} p_0^{-1} & 0 & 0 \\ 0 & p_1^{-1} & 0 \\ 0 & 0 & p_2^{-1} \end{bmatrix} + p_3^{-1}\mathbf{1}$	$\begin{bmatrix} \frac{\partial p_0}{\partial r_0} & \frac{\partial p_0}{\partial r_1} & \frac{\partial p_0}{\partial r_2} \\ \frac{\partial p_1}{\partial r_0} & \frac{\partial p_1}{\partial r_1} & \frac{\partial p_1}{\partial r_2} \\ \frac{\partial p_2}{\partial r_0} & \frac{\partial p_2}{\partial r_1} & \frac{\partial p_2}{\partial r_2} \\ \frac{\partial p_3}{\partial r_0} & \frac{\partial p_3}{\partial r_1} & \frac{\partial p_3}{\partial r_2} \end{bmatrix}$	$\sqrt{\frac{1}{3} \text{tr}(F_{\bar{r}_m}^{-1})}$

Table B.1: Relevant quantities for characterizing the localization scheme performance.  $d$  is the dimensionality of the localization,  $K$  is the number of exposures of the emitter,  $p_i^{(0)}$  are the components of the multinomial vector parameter  $\bar{p}$ ,  $F_{\bar{p}}$  is the Fisher information matrix on  $\bar{p}$ ,  $J^*$  is the reduced Jacobian matrix for the change of variables from the reduced  $\bar{p}$  space to the molecule's position  $\bar{r}_m$  space and  $\tilde{\sigma}$  is the arithmetic mean of the eigenvalues of the CRB for the covariance matrix of the molecules position estimation.  $\mathbf{1}$  is an all-ones matrix. The cases  $d = 1, K = 2$  as well as  $d = 2, K = 4$  are the most relevant ones for this work. Table adapted from Balzarotti et al. (2016).

$$\langle \hat{p}_i \rangle = \frac{1}{N} \langle n_i \rangle = p_i$$

$$\langle \hat{p}_i \hat{p}_j \rangle = \frac{1}{N^2} \langle n_i n_j \rangle = \frac{N-1}{N} p_i p_j, \quad \text{for } i \neq j$$

$$\langle \hat{p}_0^2 \hat{p}_j \rangle = \frac{1}{N^3} \langle n_0^2 n_j \rangle = \frac{(N-1)(N-2)}{N^2} p_0^2 p_j + \frac{N-1}{N^2} p_0 p_j, \quad \text{for } 0 \neq j$$

Table B.2: Generalized factorial moments  $\langle n_j^k n_i \rangle$  of the multinomial distribution  $P(\bar{n} | N, \bar{p})$  of eq. (2.11) for relevant orders  $k$ . They were obtained from Mosimann (1962) and are used in sec. 2.2.2.

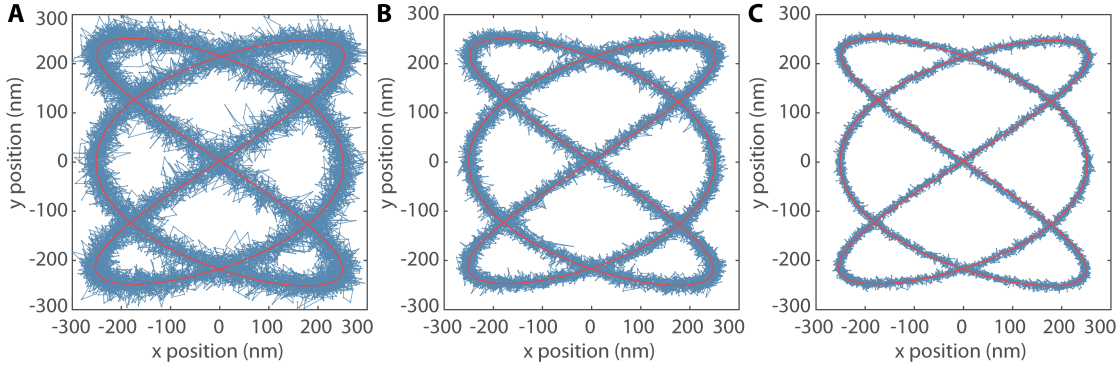


Figure B.1: (A) Tracking of predefined trajectory using a 20 nm fluorescent microsphere. The emitter was moved in the  $xy$ -plane along a predefined trajectory using the piezo stage (solid red line). The peak-to-peak amplitudes were 500 nm and the frequencies were 1.5 Hz and 1 Hz in  $x$  and  $y$ , respectively. MINFLUX tracking was performed with a beam separation of  $L = 100$  nm and a multiplex cycle rate of 8 kHz. Live position estimation is calculated using the mLMS estimator (see sec. 2.2.2) with parameters set to  $k_i = 1.2$  and  $\beta_1 = 3$  (see eq. (4.1)). The retrieved trajectory is shown by the blue line. The mean number of photons per localization was  $N = 11.5$ , corresponding to a count rate of 92 kHz. (B) Equal conditions as in (A) except for a count rate of 283 kHz (32 photons per localization). (C) Equal conditions as in (A) except for a beam separation of  $L = 50$  nm and a count rate of 327 kHz (40 photons per localization).

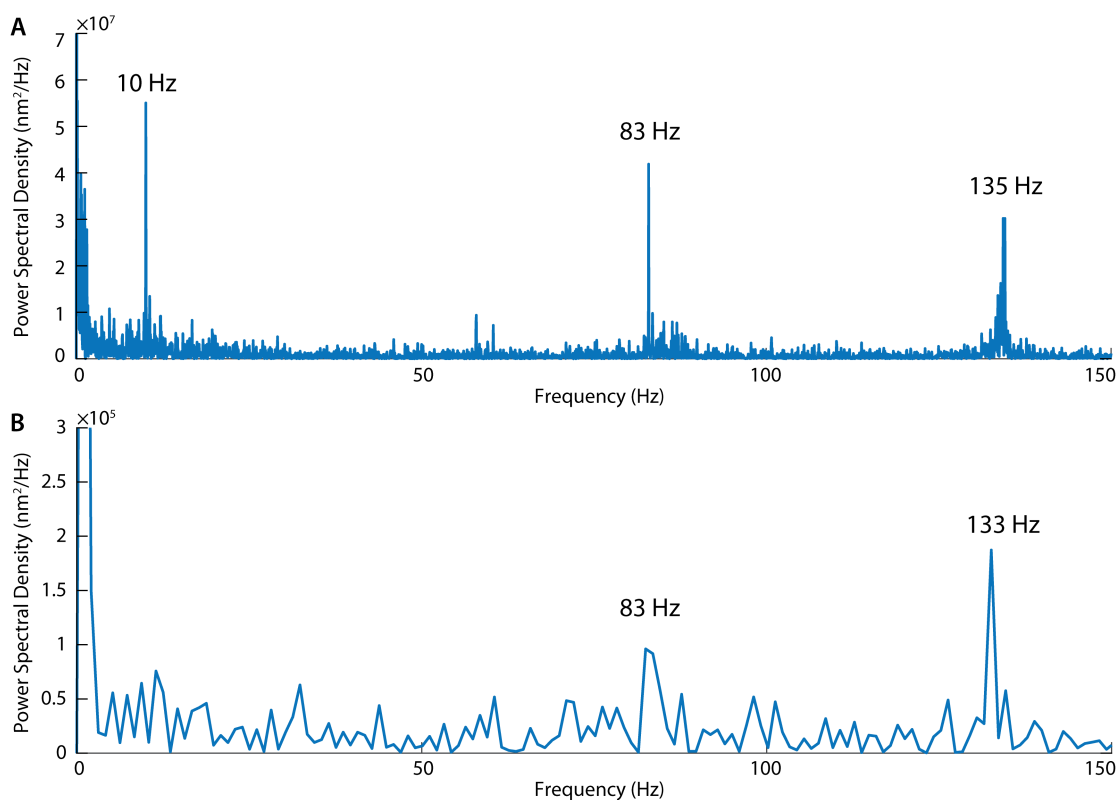


Figure B.2: (A) Power spectral density of the numLMS  $y$ -position estimation of a static emitter. The corresponding localization histogram comprising 25000 localizations is shown in fig. 3.6 (B). The frequency analysis reveals prominent contributions at 10 Hz, 83 Hz as well as 135 Hz. These could arise from emitter movement or, more probably, be induced by system instabilities. (B) Power spectral density of the numLMS  $y$ -position estimation of the static emitter visualized in fig. 3.6 (E) with a total of 2396 localizations. The prominent contributions at 83 Hz and around 130 Hz reappear.





# Appendix C

## DNA sequences

## Scaffold sequence

AATGCTACTACTATTAGTAGAATTGATGCCACCTTTTCAGCTCGCGCCCAAAATAGCTAAACAGGTTATTGACCATTGCGAAATGTATCTAATGGTCAAACCTAA  
ATCTACTCGTTCGCAGAAATGGGAATCAACTGTTATATGGAATGAACTCCAGACCCGTACTTATAGTTCATATTTAAACATGTTGAGCTACAGCATTATATCAGCAATT  
AAGCTCTAAGCCATCCGCAAAAATGACCTCTTATCAAAAGGAGCAATTAAGGTACTCTAATCTGACCTGTTGGAGTTGCTCCGGTCTGGTTCGCTTTGAAGCTCGAA  
TTAAACCGCATATTTGAAGTCTTTCCGGCTCTCTTAATCTTTTATGCAATCCGCTTTGCTTCTGACTATAATAGTCAGGGTAAAGACCTGATTTTTGATTTATGGTCATT  
CTCGTTTTCTGAAGCTTTAAAGCATTTGAGGGGATTCAATGAATTTATGACGATTCCGCAGTATTGACGCTATCCAGCTAAACATTTTACTATTACCCCTCTGGCAA  
AACTCTTTTGAAGGCTCTCGCTATTTTGGTTTTATCGTCTGTTAAACGAGGGTTATGATAGTGTGCTTACTATGCCTCGTAATCTTTTGGCGTTATGATCT  
GCATTAGTGAATGGTATTCTAAATCTCAACTGATGAATCTTCTACCTGTAATAATGTTGTTCCGTTAGTTCGTTTTTAAACGTAGATTTTTTCCCAACGCTCTGACT  
GGTATAATGAGCCAGTCTTAAATCGCATAAGGTAATTCACAATGATTAAGTTGAAATTAACCATCTCAAGCCAAATTTACTACTCGTTCTGGTGTTCCTGCTAGGGCA  
AGCCTTATCTACTGAATGAGCAGCTTTGTTACGTTGATTTGGGTAATGAATATCCGGTCTTGTCAAGATTACTCTTATGATGAAGGTACAGCAGCCTATGCGCCTGGTCTGTAC  
ACCGTTCATCTGCTCTTTCAAAGTTGGTCAGTTGCGTTCCCTTATGATTGACCGCTGCGCCTGTTCCGGTAAGTAACATGAGGACAGGTGCGGGATTTCGACACAATTTA  
TCAGGCGATGATACAAATCTCCGTTGACTTTGTTTCGCGCTTGGTATAATCGTGGGGTCAAAGATGAGTGTGTTAGTATTCTTTGCTCTTTGCTTTTGGTTGGTGC  
CTCGTAGTGGCATTACGATTTTTCCCGTTTTAATGAAACTCTCATGAAAAAGCTTTAGTCTCAAAGCTCTGACCCCTGTTGACCCCTGTTCCGATCGCTTTCCG  
TGCTGAGGGTGACGATCCCGCAAAAGCGGCTTAACTCCCTGCAAGCCTACGACCGAATATATCGTTATGCGTGGGCGATGGTGTGTCATTGTCGCGCAACTATC  
GGTATCAAGCTGTTAAGAAATCACCTCGAAAGCAAGCTGATAAACCGATACAATTAAGGCTCCTTTTGGAGCCTTTTTTGGAGATTTTCAACGTGAAAAAATTAAT  
TCGCAATTCCTTAGTGTCTTTTACTTCTACTCCGCTGAAACTGTTGAAAGTTGTTAGCAAAATCCCATACAGAAAAATCATTACTAACGCTGGAAAGACGACAAAA  
CTTTAGATCGTTACGTAACATGAGGGCTGTCTGGAATGCTACAGGCTGTAGTTGACTGGTGACGAAACTCAGTGTACGGTACATGGGTTCTATTGGGCTTGC  
TATCCCTGAAAATGAGGGTGGTGGCTCTGAGGGTGCCGGTCTGAGGGTGCCGGTCTGAGGGTGCCGGTACTAAACCTCTGAGTACGGGTATACACCTATTCCGGCT  
ATACTTATCAACCTCTCGACGGCACTTATCCGCTGGTACTGAGCAAAACCCGCTAATCTAATCTCTTCTGAGGAGTCTACGCTCTTAATACTTTCATGTTTCAGAA  
TAATAGGTTCCGAAATAGGCAGGGGGCATAACTGTTATACGGGCACTGTACTCAAGGCACTGACCCGGTAAAACTTATTACCAGTACACTCTGATCATCAAAGCCA  
TGATGACGCTTACTGGAACGGTAAATTCAGAGACTGCGCTTCCATTTCTGGCTTAAATGAGGATTTATTTGTTGTAATATCAAGGCAATCGTCTGACTGCCTAACCTC  
CTGCTAATGCTGGCGCGCTCTGGTGGTGGTCTGGTGGCGCTGAGGGTGGTGGCTGAGGGTGGCGGTTCTGAGGGTGGCGGCTGAGGGGAGCGGTTCCGG  
TGGTGGCTCTGGTCCGGTATTGTTGATGAAAAGATGGCAACGCTAATAAGGGGCTATGACCGAAAAATGCCGATGAAAAAGCTACAGCTCTGACGCTAAAGGCA  
AACTTATTCTGCTACTGATTACGGTGTCTATCGATGGTTTCTGGTACGTTTCCGGCTTGTAAATGGTAAATGGTACTGTTGATTTGCTGGCTAATTTCC  
AAATGGCTCAAGTCGGTACGGTGATAATCACCTTAAATGAATAATTCGCTCAATATTTACCTCCCTCCCTCAATCGGTTGAATGTCGCCCTTTGCTTTGGCGCTGGTA  
AACCATATGAATTTTCTATTGATTGACAAAAATAAATTTTCCGTTGGTCTTTCGCTTTTATATGTTGCCACCTTATGATGATTTTTCTACGTTTGTAACTACTG  
CGTAATAAGGAGTCTAATCATGCCAGTCTTTGGTATTCCGTTATATTGCGTTTCTCGGTTTCTCTGTAACCTTTGTTCCGCTACTGCTTACTTTAAAAAGGG  
CTTCGGTAAAGATAGCTATTGCTTCTTCTGCTTATTAATGGGCTTAACTCAATCTTGTGGGTTACTCTCTGATATTAGCCTCAATTTACCTCTGACTTTGTTT  
AGGGTGTTCAGTAAATCTCCGCTAATGCGCTTCCCTGTTTTATGTTATTCTCTGTAAAGGCTGCTATTTTCAATTTTACGTTAAACAAAAAATCGTTTCTATTGGAT  
TGGGATAAATAATATGGCTGTTATTTGTAAGTGGCAAAATAGGCTCTGGAAGACGCTGTTAGCGTTGTAAGATTAGGATAAAAATGATGCTGGTGGCAAAATAGCA  
ACTAATCTTGATTTAAGGCTTCAAACCTCCCGCAAGTCGGGAGGTTCCGTAACCGCTCGGCTTCTAGAATACCGGATAAGCCTTCTATATCTGATTTGCTGTCTATTGG  
CGCGGTAATGATTTACTACGATAAAATAAAGCGGCTGCTGTTCTCGATGAGTGCAGTACTGGTTTAAATACCCGTTCTTGGAAATGATAAGGAAAGACAGCCGATTAT  
GATGGTTTTCTACATGCTGATAAATAGGATGGGATATTTTTTCTGTTTCAGGACTTATCTATTGTTGATAAACAGGCGCGTTCTGATTAGCTGAACATGTTGTTATTGT  
CGTCTGCTGGACAGAAATTTACTTTTACCTTTTGTGGTACTTTATATTCTTATTACTGCTCGAAAAATGCCTCTGCCTAAATACATGTTGGCGTTGTAATATGGCGATTCTC  
AATTAAGCCCTACTGTTGAGCGTTGGCTTATACTGTTAAGAAATTTGATAACGCATATGATTAACAGCGCTTTTTCTAGTAATTTAGTTCGGGTGTTTATTCTATTAAAC  
GCCATTTATACACCGGTCGGTATTTCAAACCTAATTTAGGTCAGAAGATGAAATTAACATAAATAATTTGAAAAAGTTTTCTCGGCTTCTTGTCTTGGCATTGGATT  
TGCATAGCATTACATATAGTTTATAACCAACCTAAGCCGGAGGTTAAAAAGTGTCTCTCAGACCTATGATTTTGAATAATTTACTACTGCTTACTTACGCTCTTAA  
TCTAAGCTATCGTATGTTTTCAAGGATTCTAAGGGAAAAATAAATAGCGACGATTACAGAAGCAAGGTTATTCACTCACATATATTGATTTATGACTGTTTCCATTA  
AAAAGGTAATCAAATGAAATGTTAAATGTAATTAATTTGTTTTCTGATGTTGTTTCATCATCTCTTTGCTCAGGTAATGAAATGAATAATTCGCTCTGCGGATT  
TGTAATCTGGTATTCAAAGCAATCAGGCGAATCCGTTATTGTTTTCCCGATGTAAGGTAAGTACTGTTACTGATATTACTCTGACGTTAAACCTGAAACCTACGCAATTTCT  
TATTTCTGTTTACGTGCAAAATTTGATATGGTAGGTTCTAACCTTCCATTATTCAGAAGTATAATCAAACAATCAGGATTATTTGATGAATGGCCATCATCTGATAAT  
CAGGAATGATGATAATCCGCTCTTCTGGTGGTCTTGTTCGCAAAATGATAATGTTACTCAAACCTTTAAAAATAAAGCTTGGCAATTTTAAAGCTTCTGATTGTTT  
GTCGAATGTTTGAAGTCTAATCTTAAATCTCAAATCTCAAATGATTATCTATTGACGGCTCTAATCTATTAGTTGTTAGTCTCTAAAGATAATTTAGATAACCTTCTCAATT  
CCTTCAACTGTTGATTGGCAACTGACCAGATATTGATTGAGGGTTGATATTGAGGTTGAGCAAGGTATGCTTACTGTTGGCCAGAAATGCCTTTTATTACTGGTCTGTGACTGGTGA  
ATCTGCCAATGATAAATCAATTTACAGAGATTGAGCGTCAAAATGATAGGATTTCCATGAGCGTTTTCTGTTGCAATGGCTGGCGGTAATATTGTTCTGGATATTACCA  
GCAAGGCCGATAGTTGAGTTCTTACTACGCAAGTATGTTATTACTAATCAAGAAGTATTGCTACAACGGTTAATTTGCGTGATGGACAGACTCTTTACTCGTGGC  
CTCACTGATTAAAAACCTTCTCAGGATTCTGGCGTACCGTTCTGTCTAAAACTCCTTAAATCGGCTCCTGTTAGCTCCCGCTGATTCTAACGAGGAAAGACAGCTTA  
TACGTGCTGCTCAAAGCAACCATAGTACGCGCCTGTAGCGCGCATTAAAGCGCGGGGTTGGTGGTTACGCGCAGCGTACCCGCTACACTTCCAGCGCCTTAGCGCC  
CGCTCTTTGCTTTCTTCCCTTCTTCTCGCACGTTCCGCGGCTTCCCGCTCAAGCTCTAAATCGGGGCTCCTTTAGGTTCCGATTAGTCTTTACGGCACCTCGAC  
CCCCAAAAATGATTTGGGTGATGTTTACAGTAGTGGGCCATCGCCCTGATAGACGGTTTTTCGCCCTTTGACGTTGGAGTCCACGTTCTTAAATAGTGGAATCTGTTCCA  
AACTGGAACAACACTCAACCTATCTCGGCTATTCTTTGATTATAAGGGATTTGCCGATTTCGGAACCACCATCAACAGGATTTTGCCTGCTGGGGCAACACAGCGT  
GGACCCTTGTGCAACTCTCTCAGGGCCAGCGGTGAAGGGCAATCAGCTGTGCCCCTCTACTGGTGAAGAAAGAAAAACCCCTGGCGCCAAATACGCAAAACCGCTC  
TCCCAGCGGTTGGCCGATTCAATAGCAGCTGGCACGACAGGTTCCCGACTGGAAGCGGGCAGTGAGCGCAACGCAATTAATGTAGTTAGTCTACTCATTAGGCAC  
CCCAGGCTTACACTTATGCTCCGGCTCGTATGTTGTGGAAATTTGAGCGGATAACAATTTACACAGGAAACAGCTATGACCATGATTACGAATTCGAGCTCGGTACC  
CGGGATCTCTAGAGTGCAGCTGACGGATGCAAGCTTGGCACTGGCGCTGTTTTACAACGCTGACTGGGAAAACCTGGCGTTACCCAATTAATCGCTTTCAGCA  
CATCCCCTTCCGACGCTGGCGTAATAGCGAAGAGCCCGACCGATCGCCCTCCCAACAGTTGCGCAGCCTGAATGGCGAATGGCGTTGCTGCTTCCGGCACCAG  
AAGCGGTCCGCGAAAGCTGGTGGAGTGGCATTTCTGAGCGCGATTGTCGCTGCTCCCTCAAATGGCAGATGACGGTTACGATGCGCCATCTACACAAACGTTGA  
CTATTTCCATTACGGTCAATCCGCGTTTGTCCACGGAGAATCCGAGGGTTGTTACTCGCTCACATTAATGTTGATGAAAGCTGGCTACAGGAAGGCCAGACGGAAAT  
TATTTTTGATGGGCTTCTGATTATCAACCGGGTACATATGATTGACATGCTAGTTTTACGATTACCGTTTCTGATTCTGTTTGTCCAGACTCTCAGGCAATGACCTGAT  
AGCCTTTGATAGTCTCTAAAAATAGCTACCCTCCTGGCAATTAATATCAGCTAGAACGGTTGAATATCATATTGATGGTATTGACTGCTCCGGCTTCTCACCTTTT  
GAATCTTACCTACACATACTCAGGCATTGCATTTAAAAATATAGAGGGTCTAAAAATTTTTATCTTGGTGAATAAAGGCTTCCCGCAAAAGATTACAGGGTCA  
AATGTTTTGGTACAACCGATTAGCTTATGCTCTGAGGCTTATTGCTAATTTGCTAATTTGCTTGGCTGTATGATTTATTGGATGTT

Origami staples #	Sequence
78	CATAACCCGAGCATAGTAAGAGCTTTTAAAG
79	GCAATAGCGCAGATAGCCAAACAACTTCAACCG
80	GCCCAATACCGAGAAAGCAAGCAATAGGTTAAC
81	ATCAGAGAAAGAACTGGCATGATTTTATTTTG
82	TGACAAACAGATATGTTAGCAAACTAAAGAA
83	AAACAGTGTAGGCTTAGAGCTTTTAAATA
84	CAAAATCATGTCCTTTTGAAGTTTTCAT
85	TCAGAGCCTCAACAGCTAGGATCTGCGAA
86	AMGAGAAAGAGGTTCAAAAGCAAGATACATT
87	CCTAATTTAGGCTAAAGAGGCTCTATATCGGG
88	ATATTTAACCCAGCTAGAAATTTTCAAGAGG
89	TTTTTTTAGGCTTAAATCAAGATTCGAA
90	CTTACAGTTAGCGAACTCCCGAGTAGGAA
91	TTTTTGGCAGAAAAGAGAGATGATTTGTTAG
94	TACCTTTAAGGCTTTACCTGACAAAGAGT
95	GAAGCAAAAAGAGGATGTCATCAGATAAAA
96	TTTTAATTTGGCCGAAGAGCTCAATTCAGAG
97	TCTTACAGCCAGTTCACAAATAATGANAATA
98	TATTTTTGCTCCCAATCCAAATTAAGTAGTTAA
99	AGGTTTTAGAGCTCAAAATGAAAAGGCTAAT
100	GAGGCTTAGAGAAATAACATAAAAGAACCC
101	TGCAACTAAGCAATAAAGCTCAGTTATGACC
102	TCCATATACAGAGGCAAGGCAACTTATTT
103	GGAGTAGACTAATAGTAGTAGCAGAACCTCA
104	TGCAAAATGGGGGGAGCTGAAATATATGTT
105	ATCGCTTGGAGCATGATAGAACCCAGCTATAT
106	GGTATTAGAAACAGAAAATAATTAAGGCCA
107	CAAGCAAGACGCGCTTTTATCAAGAACTCC
108	TCAATACCCGACATAAACAACATATTIAGGC
109	TATAGAGCAACAAGAGTAAAGTAGAANAATA
110	GCTAATCTGAGCTCAACATGATGCTGTA
111	CAAAATTAAGTAGCGGTGCTGGAAAGGTTCA
112	CAATAATACAGTTGATTCCTCCATTTAGAGAG
113	TCAAATCTTTAGTTGAGCACTACCAAGACCG
114	TTTTCTTGGTCAATACTCTTAACTCAATA
115	CTAATTTCTTCTTATCATCTCACTCTGAA
116	TAGTCTACAGTAGCAGCAGCTAGTTCG
117	AAATGACAGGTTTTTATTTTCTACTCTGGGG
118	CGAGAGCGCCCAATAGCAGCAAGAAAGCC
119	CTGTAAATTTGCTGAGAGTCTGGAAAACCTAG
120	CAACCAATTTTGGAGAGTACTGTAATC
121	TATATTTAGCTATAAATTAATTTGTTATAA
122	AGGTAAGAAATCACCAATCAATAATAATTTT
124	ACGCTCAAAATAGAAATAACACCGTGAATTT
125	CATATTTAGAAATACGAGCGTGTACTCTTT
126	AGAGGCAATTTCTCTCTGACTATAACTA
129	TCAGGCTACTTTTGGGGAGAGCAAGAAATAG
130	GGTAGCTAGGATAAAAATTTTGTAACTC
131	ACGCTTAAATGCAATGCTGAGAGGTGCA
132	AGACAGTCAATCAAAAGGGTAGATATCAT
133	AATTACTCAAAATTTTACAGTAACTCCATC
134	AGGCGTTACAGTAGGGCTTATTTGACATAAGA
135	AAATGGTTACACGCCCAACTAGTGTAGCT
141	TTTTAGGTTTTCGAGCAAGTAAATAATCTGT
142	TAACTCCATATGTTAGTAAATAAATAAATC
143	TATGAACTTTTAAATTTTGGAAAATTAACCT
144	TATGAACTTTTAAATTTTGGAAAATTAACCT
147	ACCGTGTCAATGATACCCGCTAAAGGCTA
148	CTTTCATCCCAAAAACAGAAAGCCGGAGAG
149	AAATATTTTAAATTTGTAAGCTGTATTTCA
150	GCTAATTTGGGATTAATTTTGTAGCTTAGA
151	TAGAATCTGAGAAAGTCAATAGAAATCAT

Origami staples #	Sequence
2	ACGTTAGTAAATGAATTTTGTAAAGCGAGT
3	GTAAAGATTCAGAAAGTTTGTGTAAATTTGGC
4	TGTAGATTCACAGACAGCCCTCATCTCCGA
5	TGATGTTGTCACAGTAGCAACTTAATTTGTA
6	CAAGCCCAATAGAACCCCATGACCGTAAAC
7	CTAGAGCAACCCCTCATTTCTCTTATTT
8	CCCTCAAGACCGCACCTTCAAGACTAGACT
9	TATCAGTACTCAGAGAGTTTAAAGGGGGT
12	AAATAAAGTGGCTGAGGCTTGCAMAGACTT
13	AAAAAGGACAAACATGCCCACGCGGGTAAA
14	TGGTTTTAGTTGATACCGATATGCAACCTTA
15	AAATGCCCCTAAAGAGTCCGATGTAATTTT
16	CTGAAACAGTAAAGTTTAAACCTCTCAGA
17	GCTCAAGATACATGGCTTTTGTAGAACCC
18	TGCTCAGTCTGCTGAAATTTACAGAGAGT
21	AAAGGCGAAGGAAACAACTAAAGCTTTCAG
22	ATATATTTTTCACGTGTAATATAGTTAG
23	CAATGACACTCAAAAAGGAGCTTACAGCC
24	TCTAAACATCAGTTGCTTTGCGAAGAACAGT
25	TGCTTGTACTGCTATTTTGGAAAGGAGTAG
26	ATGCTACTGAAAGTATTAAAGAGGCGCCACC
27	TAAAGGTCGAGAGTATAGATAGTAGCGCA
29	AGGCTACTTACTTAGCCGAGAGCTGACCA
30	TTTTGATGAAATTTGTGCAAACTTCTACAGA
31	ATAGTAAAGTACAAAGGAGATTTCTCAAG
32	AAAGCAAGTACAGCCCAAGCGAATTTACTTAC
33	GAGCCGCGCAACCGCAAGCCGCTAAMACA
34	GGCAAGCTTTTCAATTAACAACCTGTCACC
35	CACAGAGTTGCTCAAGGCCCCGGCAGAAA
36	TGAGGAGGCTGAGACTGTAGCTAGTAGGAG
39	GCTCATGAGAGGCTTGTAGGACTAGGAGATT
40	GCGCTGATGGAATTTTCAATTAACAATAAGCC
41	GGAAACATGCACTAGAGAGGCTTGGCCGA
42	CTCATCTTGGGCAAAAGAAATACCTCTCA
43	AAACAGAGCTTAGAACGCGAGGAGTACAG
44	GTTTGCCTCTGAGAGCCCAAGCTAGCAGG
45	TGCGAATTTGGGGGAGAGCTTGAAGTTCAG
46	TGCTTTAGTCAAGAGATTTGCTGCGAAT
47	CTTTGAAAGAACTGGCTTATTTAATAAA
48	CCAGGCGTTAATCTGTTGAAATACAGTAG
49	AGTAACTTAAATTTGGGCTTGAAGATAACA
50	CCAAATCTGCCCCTGACAGAGCGCAAAA
51	TTATCATAGGAAAGTAAATTAATCTAGT
52	GACTTGAGAGCAAAAGGCGCAAGTAACTCA
53	AAATCAAAATAGAAAATTCATATAAACCGA
54	CCGGAACACACCGGAATAAGTAAAGTCTC
57	GGATTTTAGAGACAGATGAAAGGAGGACT
58	TTTCAACTAGGCTGGCTGACTGTATCAT
59	AGAGTAGTCAAGAGACGGATATACCAAGC
60	GAAATAGGAGCTTAAAGTGTCTGAGGAAA
61	ATTAGGTTAAAGTGAATTTATCAATCCGCG
62	AGCCCAACCAATTTGGGAATAGATTAATAGC
63	TCAAATGTTAGCAGCAATACCATCTTTTCA
64	AGCAAAAGTCCAAATGAAACCAATCAAGTT
65	AGCAACTAGGTTCAATTAATGCGGATGCTTT
66	AAAGATTAGGGGTTAATAGTAAACATTAAT
67	CATTCAGCGGAGAGGCTTTTGCATATATAG
68	GAAATCTGTTTACAGAGCAAAAGAT
69	AAAAGTATCTTACCGAAGCCCACTAT
70	GAAGAAATTAAGCAAGCAAAACAAGCCAT
71	ATACCAAGATAACCAAGATAAAGGAT
72	TTATAGGTTCAAGGGTAAATGATAGGAGC
75	ACTGAGATACGGAAACAACTATACCTTATG
76	TTTTGCGAGATAGTGGAGATTTAGTGGTTAA
77	CCAAAATAATAGTCAGATACATAAACCAGAA

<b>76 single molecule helper</b>	TTA TTC CTG TAG TAT ATG GCA ATG AAA TTA T -- TTT GCC AGT CAG TTG GAT TTT AGT GGT TTA A
<b>Single molecule strand</b>	
5' strand	TAA TTT CAT TGC CAT ATA CTA CAG GAA TAA
<b>Nes22 &amp; Nes76 helper</b>	
1DD 22	AATGGGGAAGAGGGGCTACCTGCAGTCTAATTGCC -- AATACC ATATAATCTTTTTCAGGTGGAAAATAGTTAG
1DD 76	TTT GCC AGT CAG TTG GAT TTT AGT GGT TTA A TGGATA -- GAGGCTATGAGATTGCTCCAGCAAGCAAGCCATATT
<b>Bridge</b>	
1DD bridge	GTATTGGCAATTAGACTTGCAGGTAAAGCCCTCTCCCAT -- TTAATATGGCTTGGTCTGGAGACAATCTCATAGCCCTCATCC

152	CTGTAATCATAGGCTGAGAGACGATAAATA	
153	AAATCAATGGCTTAGGTTGGGTTACTAAATTT	
154	TTGAAATATGGTGATGCAAAATCCACAATATA	
155	TAGATGGGGGTAAGCCAGGTTGEGCAAG	
156	GTTTAGGGAAAGGGGGATGCTAGAGAGATC	
157	GAGATTCGGTGGGGGCTCTCCCAATCTGG	
158	GCCTGGTCAGGCTGGCACTGTGTATCC	
159	CTTTTACACAGTAATATACAGTAAGGCGCA	
160	CTGATTGAAAAGAAATGGGTAGACCCGAAC	
161	GGCCAGAGATCAAAATATTTTGAATATC	
162	GAGCAAACTCTGMAATAGBAGAGGAG	
165	ATATAGTTGCACTGTAACCTGCGAGTAMCA	
166	CAGCTGGGGAGAGACAGATGCTGGTAGCGAG	
167	GGCGATGCGACTCAGCCAGCTTGCCATCAA	
168	TTCCGATTCGGGAACCCAGCAACAGATC	
169	TTTAACGTTGGGGAGAAACAATATTTCCCT	
170	ACGAAATCTTTGMAATACCAAGTTCTTGCTT	
171	AACCTACCGGAAATATTCATTTCCAGTAGAT	
172	TGGATATAGAGATGATGAACAATAATTCAT	
173	CTTGATGCAATTAAGTAAATCGCCCGCAGGG	
174	CCGGGTACTTCCAGTGGGAAACGGGCAAC	
175	TCATAGCTACTACAAATTTGCGCCCTGAGA	
176	GGTCAAAAGTAAAGCTGGGGTGGGTTGGCC	
177	GGCAACTAAGTATAGACTTANCGCGGAA	
178	TTATATGGCGTCAATAGATATAGAGGTG	
179	ATTTTGGCTTTAGGGAGCACTAAGCCAGT	
180	CGGAATATTGAAGAAATTAAGGTGAAAAT	
183	GCCAGCTGCTCAGTGGGAAACGGGCAAC	
184	ACTGCCCGCAGCTCGAATTTGTTATTAGGC	
185	GTGAGTATGTTCTGCTGTTGMAAATGGGGAAG	
186	GCATAAGTTCCACACACATAGCAACAAT	
187	GGATTAGGTATTAATCTTTGTTTCAGG	
188	AGATTAGATTAAMAAGTTTGGATGACGATAA	
189	CTAAAATAGACAAGAAACCCAGGGTTAG	
190	ATCAAGTACTATCTCTGATTGATGTT	
192	AGCTGATCAAGAGTCCACTTGAAGTGGC	
194	GAGTGCAGAGTAGGGTTGAGTAGGGAGC	
194	CCAGACGGGCAMAATCCCTATAAAGCCGCG	
195	AGAAACMAAGATGCGCATTAATGTTGTT	
196	AGGGGTGATTAGTCTTTAATGGCAATATA	
197	GCCAGCTTACGTGGCAGACAACCGCTCAT	
198	CTAAGCAAGATAGAAACCTCTGAAATGCT	
201	TGGACTCCCTTCCACAGTAGAGACTGTGT	
202	AGTTTGGAGCTTCCAGCCCTGTTGGGCTC	
203	GAAATGCGGAGGGTCCAGCTCTCTATAGA	
204	CCGMAATCGAAMATCTGTTGMAATACCGA	
205	TAGCCTTACCAGAGAAGATAAAACATTTGA	
206	GAAATGCTAGTATTAAAGCCCTCAACTAAT	
207	GGTAAAGAGAGAGCCAGCAAAAAGTTAT	
210	ACCCAATCAAGTTTTTGGGTTCAAGAGC	
211	GTAAGCACTAATCGAACCCCTAGTTGTCC	
212	CCCGATTTAGAGCTGGAGGGGAATONAMA	
213	GAACTGGGGAGAAAGGAAAGCAAAACTAT	
214	CGCCCTGCTGGTATATCCAGAACGAACTGA	
215	CCGCCAGCCATGCAACAGAAATAATTTT	
216	GGAAATACCTACATTTTGAAGCTCACTGAAA	
217	GAAATGGATTATTACATTGGCAGACATCTG	
<b>Biotinylated Strands</b>		
<b>5' biotin modification</b>		
#	<b>Sequence</b>	<b>Length (bp)</b>
11	GAGAAATGCTTTGGGGATGCTGGGGTAGCA	32
191	TGGTTTTAAGGTCAAAGGGGGAAGAACCTC	32
123	GGTTATAGAAAAGCCCTGTTAGAGCGCGG	32
28	GGAAAGCAGCAGCGGGATAGTGAATAGGTG	32
208	GCCAAAGTCACTGCTGCAAACTGTTGGCAA	32

# Bibliography

- Abbe, E. (1873). Beiträge zur Theorie des Mikroskops und der mikroskopischen Wahrnehmung. *Archiv für mikroskopische Anatomie*, 9(1):413–418.
- Altman, R. B., Terry, D. S., Zhou, Z., Zheng, Q., Geggier, P., Kolster, R. A., Zhao, Y., Javitch, J. A., Warren, J. D., and Blanchard, S. C. (2012). Cyanine fluorophore derivatives with enhanced photostability. *Nat. Methods*, 9(1):68–71.
- Annibale, P., Dvornikov, A., and Gratton, E. (2015). Electrically tunable lens speeds up 3D orbital tracking. *Biomed. Opt. Express*, 6(6):2181–2190.
- Bakshi, S., Siryaporn, A., Goulian, M., and Weisshaar, J. C. (2012). Superresolution imaging of ribosomes and RNA polymerase in live *Escherichia coli* cells. *Mol. Microbiol.*, 85(1):21–38.
- Balzarotti, F., Eilers, Y., Gwosch, K. C., Gynnå, A. H., Westphal, V., Stefani, F. D., Elf, J., and Hell, S. W. (2016). Nanometer resolution imaging and tracking of fluorescent molecules with minimal photon fluxes. *arXiv preprint arXiv:1611.03401*.
- Bergemann, F., Alber, L., Sahl, S. J., Engelhardt, J., and Hell, S. W. (2015). 2000-fold parallelized dual-color STED fluorescence nanoscopy. *Opt. Express*, 23(1):211–223.
- Berglund, A. J. (2010). Statistics of camera-based single-particle tracking. *Phys Rev E Stat Nonlin Soft*, 82(1):011917.
- Betzig, E., Patterson, G. H., Sougrat, R., Lindwasser, O. W., Olenych, S., Bonifacio, J. S., Davidson, M. W., Lippincott-Schwartz, J., and Hess, H. F. (2006). Imaging intracellular fluorescent proteins at nanometer resolution. *Science*, 313(5793):1642–1645.
- Bobroff, N. (1986). Position measurement with a resolution and noise-limited instrument. *Rev. Sci. Instrum.*, 57(6):1152–1157.

- Chao, J., Ward, E. S., and Ober, R. J. (2016). Fisher information theory for parameter estimation in single molecule microscopy: tutorial. *J. Opt. Soc. Am. A*, 33(7):B36–B57.
- Cranfill, P. J., Sell, B. R., Baird, M. A., Allen, J. R., Lavagnino, Z., de Gruiter, H. M., Kremers, G.-J., Davidson, M. W., Ustione, A., and Piston, D. W. (2016). Quantitative assessment of fluorescent proteins. *Nat. Methods*.
- Dai, M., Jungmann, R., and Yin, P. (2016). Optical imaging of individual biomolecules in densely packed clusters. *Nat. Nanotechnol.*
- Deschout, H., Zanicchi, F. C., Mlodzianoski, M., Diaspro, A., Bewersdorf, J., Hess, S. T., and Braeckmans, K. (2014). Precisely and accurately localizing single emitters in fluorescence microscopy. *Nat. Methods*, 11(3):253–266.
- D’Este, E., Kamin, D., Velte, C., Göttfert, F., Simons, M., and Hell, S. W. (2016). Subcortical cytoskeleton periodicity throughout the nervous system. *Sci. Rep.*, 6.
- Elf, J., Li, G.-W., and Xie, X. S. (2007). Probing transcription factor dynamics at the single-molecule level in a living cell. *Science*, 316(5828):1191–1194.
- Engelhardt, J., Keller, J., Hoyer, P., Reuss, M., Staudt, T., and Hell, S. W. (2010). Molecular orientation affects localization accuracy in superresolution far-field fluorescence microscopy. *Nano Lett.*, 11(1):209–213.
- Fisher, R. A. (1922). On the mathematical foundations of theoretical statistics. *Phil. Trans. R. Soc. A*, 222:309–368.
- Gallatin, G. M. and Berglund, A. J. (2012). Optimal laser scan path for localizing a fluorescent particle in two or three dimensions. *Opt. Express*, 20(15):16381–16393.
- Giepmans, B. N., Adams, S. R., Ellisman, M. H., and Tsien, R. Y. (2006). The fluorescent toolbox for assessing protein location and function. *Science*, 312(5771):217–224.
- Ha, T. and Tinnefeld, P. (2012). Photophysics of fluorescence probes for single molecule biophysics and super-resolution imaging. *Annu. Rev. Phys. Chem.*, 63:595.
- Hayashi, F. (2000). *Econometrics*. Princeton University Press.

- Hell, S. W. (2007). Far-field optical nanoscopy. *Science*, 316(5828):1153–1158.
- Hell, S. W. and Wichmann, J. (1994). Breaking the diffraction resolution limit by stimulated emission: stimulated-emission-depletion fluorescence microscopy. *Opt. Lett.*, 19(11):780–782.
- Hess, S. T., Girirajan, T. P., and Mason, M. D. (2006). Ultra-high resolution imaging by fluorescence photoactivation localization microscopy. *Biophys. J.*, 91(11):4258–4272.
- Huang, B., Babcock, H., and Zhuang, X. (2010). Breaking the diffraction barrier: super-resolution imaging of cells. *Cell*, 143(7):1047–1058.
- Huang, B., Wang, W., Bates, M., and Zhuang, X. (2008). Three-dimensional super-resolution imaging by stochastic optical reconstruction microscopy. *Science*, 319(5864):810–813.
- Huang, F., Hartwich, T. M., Rivera-Molina, F. E., Lin, Y., Duim, W. C., Long, J. J., Uchil, P. D., Myers, J. R., Baird, M. A., Mothes, W., et al. (2013). Video-rate nanoscopy using sCMOS camera-specific single-molecule localization algorithms. *Nat. Methods*, 10(7):653–658.
- Kay, S. M. (1993). *Fundamentals of statistical signal processing, volume I: estimation theory*. Prentice Hall.
- Kis-Petikova, K. and Gratton, E. (2004). Distance measurement by circular scanning of the excitation beam in the two-photon microscope. *Microscopy research and technique*, 63(1):34–49.
- Kiuchi, T., Higuchi, M., Takamura, A., Maruoka, M., and Watanabe, N. (2015). Multitarget super-resolution microscopy with high-density labeling by exchangeable probes. *Nat. Methods*, 12(8):743–746.
- Klar, T. A., Jakobs, S., Dyba, M., Egner, A., and Hell, S. W. (2000). Fluorescence microscopy with diffraction resolution barrier broken by stimulated emission. *Proc. Natl. Acad. Sci.*, 97(15):8206–8210.
- Kusumi, A., Tsunoyama, T. A., Hirose, K. M., Kasai, R. S., and Fujiwara, T. K. (2014). Tracking single molecules at work in living cells. *Nat. Chem. Biol.*, 10(7):524–532.

- Levi, V., Ruan, Q., Kis-Petikova, K., and Gratton, E. (2003). Scanning FCS, a novel method for three-dimensional particle tracking. *Biochemical Society Transactions*, 31(5):997–1000.
- Lew, M. D., Backlund, M. P., and Moerner, W. (2013). Rotational mobility of single molecules affects localization accuracy in super-resolution fluorescence microscopy. *Nano Lett.*, 13(9):3967–3972.
- Li, W., Bouveret, E., Zhang, Y., Liu, K., Wang, J. D., and Weisshaar, J. C. (2016). Effects of amino acid starvation on RelA diffusive behavior in live *Escherichia coli*. *Mol. Microbiol.*, 99(3):571–585.
- Mandelkern, M., Elias, J. G., Eden, D., and Crothers, D. M. (1981). The dimensions of DNA in solution. *J. Mol. Biol.*, 152(1):153–161.
- Manley, S., Gillette, J. M., Patterson, G. H., Shroff, H., Hess, H. F., Betzig, E., and Lippincott-Schwartz, J. (2008). High-density mapping of single-molecule trajectories with photoactivated localization microscopy. *Nat. Methods*, 5(2):155–157.
- Marx, V. (2015). Probes: paths to photostability. *Nat. Methods*, 12(3):187–190.
- McKinney, S. A., Murphy, C. S., Hazelwood, K. L., Davidson, M. W., and Looger, L. L. (2009). A bright and photostable photoconvertible fluorescent protein for fusion tags. *Nat. Methods*, 6(2):131.
- Mehta, S. B., McQuilken, M., La Riviere, P. J., Occhipinti, P., Verma, A., Oldenbourg, R., Gladfelter, A. S., and Tani, T. (2016). Dissection of molecular assembly dynamics by tracking orientation and position of single molecules in live cells. *Proc. Natl. Acad. Sci.*, 113(42):E6352–E6361.
- Michalet, X. (2010). Mean square displacement analysis of single-particle trajectories with localization error: Brownian motion in an isotropic medium. *Phys Rev E Stat Nonlin Soft*, 82(4):041914.
- Michalet, X. and Berglund, A. J. (2012). Optimal diffusion coefficient estimation in single-particle tracking. *Phys Rev E Stat Nonlin Soft*, 85(6):061916.
- Moerner, W. E. and Kador, L. (1989). Optical detection and spectroscopy of single molecules in a solid. *Phys. Rev. Lett.*, 62(21):2535.
- Mortensen, K. I., Churchman, L. S., Spudich, J. A., and Flyvbjerg, H. (2010). Optimized localization analysis for single-molecule tracking and super-resolution microscopy. *Nat. Methods*, 7(5):377–381.



- Mosimann, J. E. (1962). On the compound multinomial distribution, the multivariate  $\beta$ -distribution, and correlations among proportions. *Biometrika*, 49(1/2):65–82.
- Mukhopadhyay, N. (2000). *Probability and statistical inference*. CRC Press.
- Ober, R. J., Ram, S., and Ward, E. S. (2004). Localization accuracy in single-molecule microscopy. *Biophys. J.*, 86(2):1185–1200.
- Padilla-Parra, S. and Tramier, M. (2012). FRET microscopy in the living cell: different approaches, strengths and weaknesses. *BioEssays*, 34(5):369–376.
- Pellegrotti, J. V., Acuna, G. P., Puchkova, A., Holzmeister, P., Gietl, A., Lalkens, B., Stefani, F. D., and Tinnefeld, P. (2014). Controlled reduction of photobleaching in DNA origami–gold nanoparticle hybrids. *Nano Lett.*, 14(5):2831–2836.
- Perillo, E. P., Liu, Y.-L., Huynh, K., Liu, C., Chou, C.-K., Hung, M.-C., Yeh, H.-C., and Dunn, A. K. (2015). Deep and high-resolution three-dimensional tracking of single particles using nonlinear and multiplexed illumination. *Nat. Commun.*, 6.
- Pukelsheim, F. (1993). *Optimal design of experiments*, volume 50. Siam.
- Rao, C. R. (1973). *Linear statistical inference and its applications*. John Wiley & Sons Inc.
- Rasnik, I., McKinney, S. A., and Ha, T. (2006). Nonblinking and long-lasting single-molecule fluorescence imaging. *Nat. Methods*, 3(11).
- Rothemund, P. W. (2006). Folding DNA to create nanoscale shapes and patterns. *Nature*, 440(7082):297–302.
- Rust, M. J., Bates, M., and Zhuang, X. (2006). Sub-diffraction-limit imaging by stochastic optical reconstruction microscopy (STORM). *Nat. Methods*, 3(10):793–796.
- Sahl, S. J., Leutenegger, M., Hilbert, M., Hell, S. W., and Eggeling, C. (2010). Fast molecular tracking maps nanoscale dynamics of plasma membrane lipids. *Proc. Natl. Acad. Sci.*, 107(15):6829–6834.

- Sanamrad, A., Persson, F., Lundius, E. G., Fange, D., Gynnå, A. H., and Elf, J. (2014). Single-particle tracking reveals that free ribosomal subunits are not excluded from the *Escherichia coli* nucleoid. *Proc. Natl. Acad. Sci.*, 111(31):11413–11418.
- Schmidt, T., Schütz, G., Baumgartner, W., Gruber, H., and Schindler, H. (1996). Imaging of single molecule diffusion. *Proc. Natl. Acad. Sci.*, 93(7):2926–2929.
- Schuler, B., Lipman, E. A., and Eaton, W. A. (2002). Probing the free-energy surface for protein folding with single-molecule fluorescence spectroscopy. *Nature*, 419(6908):743–747.
- Sharonov, A. and Hochstrasser, R. M. (2006). Wide-field subdiffraction imaging by accumulated binding of diffusing probes. *Proc. Natl. Acad. Sci.*, 103(50):18911–18916.
- Shechtman, Y., Sahl, S. J., Backer, A. S., and Moerner, W. (2014). Optimal point spread function design for 3D imaging. *Phys. Rev. Lett.*, 113(13):133902.
- Shechtman, Y., Weiss, L. E., Backer, A. S., Lee, M. Y., and Moerner, W. (2016). Multicolour localization microscopy by point-spread-function engineering. *Nat. Photon.*
- Shuang, B., Byers, C. P., Kisley, L., Wang, L.-Y., Zhao, J., Morimura, H., Link, S., and Landes, C. F. (2012). Improved analysis for determining diffusion coefficients from short, single-molecule trajectories with photoblinking. *Langmuir*, 29(1):228–234.
- Small, A. and Stahlheber, S. (2014). Fluorophore localization algorithms for super-resolution microscopy. *Nat. Methods*, 11(3):267–279.
- Stracy, M., Lesterlin, C., de Leon, F. G., Uphoff, S., Zawadzki, P., and Kapanidis, A. N. (2015). Live-cell superresolution microscopy reveals the organization of RNA polymerase in the bacterial nucleoid. *Proc. Natl. Acad. Sci.*, 112(32):E4390–E4399.
- Sun, T. and Andersson, S. B. (2007). Precise 3-D localization of fluorescent probes without numerical fitting. In *29th Annual International Conference of the IEEE Engineering in Medicine and Biology Society*, pages 4181–4184. IEEE.

- Thompson, R. E., Larson, D. R., and Webb, W. W. (2002). Precise nanometer localization analysis for individual fluorescent probes. *Biophys. J.*, 82(5):2775–2783.
- Vestergaard, C. (2016). Optimizing experimental parameters for tracking of diffusing particles. *Phys Rev E Stat Nonlin Soft*, 94(2).
- Vestergaard, C. L., Blainey, P. C., and Flyvbjerg, H. (2014). Optimal estimation of diffusion coefficients from single-particle trajectories. *Phys Rev E Stat Nonlin Soft*, 89(2):022726.
- Vogelsang, J., Kasper, R., Steinhauer, C., Person, B., Heilemann, M., Sauer, M., and Tinnefeld, P. (2008). A reducing and oxidizing system minimizes photobleaching and blinking of fluorescent dyes. *Angew. Chem. Int. Ed.*, 47(29):5465–5469.
- Wang, Q. and Moerner, W. (2010). Optimal strategy for trapping single fluorescent molecules in solution using the ABEL trap. *Appl. Phys. B*, 99(1-2):23–30.
- Weisenburger, S., Jing, B., Hänni, D., Reymond, L., Schuler, B., Renn, A., and Sandoghdar, V. (2014). Cryogenic Colocalization Microscopy for Nanometer-Distance Measurements. *ChemPhysChem*, 15(4):763–770.
- Widengren, J., Mets, U., and Rigler, R. (1995). Fluorescence correlation spectroscopy of triplet states in solution: a theoretical and experimental study. *J. Phys. Chem. A*, 99(36):13368–13379.
- Yildiz, A., Forkey, J. N., McKinney, S. A., Ha, T., Goldman, Y. E., and Selvin, P. R. (2003). Myosin V walks hand-over-hand: single fluorophore imaging with 1.5-nm localization. *Science*, 300(5628):2061–2065.
- Zhang, X., Zhang, M., Li, D., He, W., Peng, J., Betzig, E., and Xu, P. (2016). Highly photostable, reversibly photoswitchable fluorescent protein with high contrast ratio for live-cell superresolution microscopy. *Proc. Natl. Acad. Sci.*, page 201611038.
- Zheng, Q., Juette, M. F., Jockusch, S., Wasserman, M. R., Zhou, Z., Altman, R. B., and Blanchard, S. C. (2014). Ultra-stable organic fluorophores for single-molecule research. *Chem. Soc. Rev.*, 43(4):1044–1056.

# List of Abbreviations

<b>1D, 2D, 3D</b> .....	one-, two-, three-dimensional
<b>APD</b> .....	avalanche photodiode
<b>CMOS</b> .....	complementary metal–oxide–semiconductor
<b>CRB</b> .....	Cramér–Rao bound
<b>DAQ</b> .....	data acquisition
<b>DM</b> .....	dichroic mirror
<b>DNA</b> .....	deoxyribonucleic acid
<b>EBP</b> .....	excitation beam pattern
<b>(EM)CCD</b> .....	(electron multiplying) charge-coupled device
<b>EOD</b> .....	electro-optical deflector
<b>FPGA</b> .....	field-programmable gate array
<b>FWHM</b> .....	full width at half maximum
<b>IR</b> .....	infra red
<b>LMS(E)</b> .....	least-mean-square (estimator)
<b>MINFLUX</b> .....	maximally informative luminescence excitation
<b>ML(E)</b> .....	maximum likelihood (estimator)
<b>mLMS(E)</b> .....	modified least-mean-square (estimator)
<b>MSD</b> .....	mean square displacement
<b>MSE</b> .....	mean square error
<b>NA</b> .....	numerical aperture
<b>numLMS(E)</b> .....	numerically unbiased modified least-mean-square (estimator)
<b>OLFS(E)</b> .....	optimized least-square (estimator)
<b>PALM</b> .....	photoactivation localization microscopy
<b>PI</b> .....	proportional integral
<b>PSF</b> .....	point spread function
<b>ROXS</b> .....	reducing and oxidizing system
<b>SBR</b> .....	signal-to-background ratio
<b>SLM</b> .....	spatial light modulator
<b>SMT</b> .....	single molecule tracking
<b>STED</b> .....	stimulated emission depletion
<b>STORM</b> .....	stochastic optical reconstruction microscopy
<b>TCSPC</b> .....	time correlated single photon counting
<b>TIR</b> .....	total internal reflection

## Contributions

This work was carried out at the Max Planck Institute for biophysical Chemistry (MPI-BPC) in the Department of Nanobiophotonics in Göttingen. The head of department, Stefan W. Hell, initialized and supervised the entire project. Further day to day supervision was provided by Francisco Balzarotti (FB). The setup was designed and assembled with FB, where the stage lock was additionally designed and assembled with Klaus Gwosch (KG). Volker Westphal contributed as well. FB programmed the measurement control software. Measurements in sec. 3.3 were conducted and evaluated with KG. The samples in sec. 3.4.1 were designed by Haisen Ta. These contributors are all part of the Department of Nanobiophotonics, MPI-BPC. The *E. coli* BW25993 strains in sec. 4.4.1 were supplied by the Department of Molecular and Cell Biology lead by Johan Elf (Science for Life Laboratory, Uppsala University, Se-751 24 Uppsala, Sweden). Arvid Hedén Gynnå contributed to the sample preparation.

## Acknowledgement

First and foremost, I would like to express my sincere gratitude to Prof. Stefan W. Hell for the opportunity to work on this fascinating and challenging project in an outstanding research environment. His guidance as well as his continuous interest and motivation significantly contributed to the success of this project.

I would also like to thank Prof. Sarah Köster for her interest in my work, her willingness to be a referee for my thesis and for being part of my thesis advisory committee. Likewise, I want to thank Prof. Ropers for his valuable and insightful comments as an advisory committee member.

My sincerest thanks go to Dr. Francisco Balzarotti for the many fruitful discussions, his multiple contributions and the excellent mentoring that made this work possible. The teamwork throughout my time in this group was always fun and very enjoyable.

I also thank Klaus Gwosch for the productive teamwork and for always being ready and willing to help, even late at night. I greatly appreciated the many interesting and helpful conversations.

Thank you to my team members for your continuous cooperation and support; I will gladly remember it.

I also want to express my gratitude to the collaboration partners, Prof. Johan Elf, Arvid Hedén Gynnå and Dr. Fredrik Persson for their input and insights on the inner workings of cells and for their commitment to the tracking project.

Many thanks also to

- Jasmin Pape and Felix Kleißler for their invaluable advice while proof reading the thesis.
- Dr. Haisen Ta for his helpful discussions on the photo-physics of molecules and his support with sample preparations.
- Jaydev Jethwa and Rainer Pick for always being there when technical problems arose and for holding the entire optical infrastructure in order.
- Dr. Marco Roose for providing me with performant servers that never let me down.

- the optical and mechanical workshop for their reliable work.
- my office mates Federico Barabas, Heydar Shojaei, Philipp Alt, Maria Loidolt and Elke Hebisch for the many stimulating and fun conversations.
- the Max Planck Society for funding me throughout this work.

I would also like to thank my peers and co-workers in the department for providing a wonderful atmosphere and good times at work and beyond. You made the last 3.5 years a very enjoyable experience.

Finally, I want to thank my girlfriend Bryce Stewart for coping with long working hours, her encouragement and her never-ending support. It was of tremendous help throughout this work. I also want to thank my family for their generosity, helping me further my education and always being there when I needed them. Thank you.

## Publications resulting from this thesis

Balzarotti, F. †, Eilers, Y. †, Gwosch, K. C. †, Gynnå, A. H., Westphal, V., Stefani, F. D., Elf, J., Hell, S. W. (2016). Nanometer resolution imaging and tracking of fluorescent molecules with minimal photon fluxes. *arXiv preprint arXiv:1611.03401*.

†: Equal contributors.

Balzarotti, F. †, Eilers, Y. †, Gwosch, K. C. †, Gynnå, A. H., Westphal, V., Stefani, F. D., Elf, J., Hell, S. W. (2016). Nanometer resolution imaging and tracking of fluorescent molecules with minimal photon fluxes. (*Accepted as research article in Science*). †: Equal contributors.



Yvan Eilers

E-Mail: [yvan.eilers@mpibpc.mpg.de](mailto:yvan.eilers@mpibpc.mpg.de)

---

## Curriculum vitae

**Born on:** 1984-03-15

**Birthplace:** Vorwerk

**Nationality:** German



## Education

---

- 06/2013 – 02/2017     **Doctoral Student** – MPI for biophysical chemistry, Dep. NanoBiophotonics
- Title of the thesis: „Localizing and tracking of fluorescent molecules with minimal photon fluxes“
  - Adviser: Prof. Dr. Stefan W. Hell
- 03/2013 – 05/2013     **Scientific Staff** - Fraunhofer IPM, Freiburg
- 10/2005 – 10/2012     **Studies in physics (Diplom-Physiker)** – Albert-Ludwigs-Universität Freiburg
- 08/2008 – 05/2009: study abroad. University of Arizona (USA)  
Graduate studies in physics
  - Thesis – Fraunhofer IPM  
Title: „Untersuchungen zur direkten Zusammensetzungsbestimmung von Nierensteinen nach operativer Steinentfernung“  
Adviser: Prof. Dr. Jürgen Wöllenstein, Prof. Dr. von Issendorff
  - Grade: 1.1
- 08/2004 – 04/2005     **Alternative civilian service**
- 09/2001 – 06/2004     **High-School**, Gymnasium Osterholz-Scharmbeck
- 08/2000 – 07/2001     **Stay abroad** – Beloit Memorial High School, Beloit, Wisconsin, USA

## Publications

---

Miernik A, Eilers Y, Bolwien C, Hauschke D, Hesse A, Lambrecht A, Lossin P, Rassweiler J, Rebentisch G, Wetterauer U, Schoenthaler M **Automated analysis of urinary stone composition using Raman spectroscopy – Pilot study for the development of a compact portable system for immediate postoperative ex-vivo application**, *The Journal of urology* 190.5 (2013): 1895-1900

Balzarotti, F. †, Eilers, Y. †, Gwosch, K. C. †, Gynna, A. H., Westphal, V., Stefani, F. D., Elf, J., Hell, S. W. (2016). **Nanometer resolution imaging and tracking of fluorescent molecules with minimal photon fluxes.** (accepted for publication in Science).